ULTRASONIC STUDY OF CuO AND A LANDAU MODEL FOR MONOCLINIC MULTIFERROICS

RENÀN VILLARREAL

Ultrasonic study of CuO and a Landau model for monoclinic multiferroics

by

©Renán Villarreal

A thesis submitted to the School of Graduate Studies in partial fulfillment of the requirements for the degree of

M. Sc. in Physics

Department of Physics and Physical Oceanography

Memorial University of Newfoundland

September 2012

St. John's Newfoundland

Abstract

Encouraged by recent experiments on multiferroic systems using high-resolution ultrasonic measurements, we measured the temperature and field dependence of the velocity of acoustic modes in order to determine the magnetic phase diagram of the monoclinic multiferroic cupric oxide (CuO). A new transition at $T_{N3} = 230$ K, corresponding to an intermediate state between the antiferromagnetic incommensurate non-collinear spiral phase (AF2) observed below $T_{N2} = 229.3$ K and a paramagnetic phase (PM), is revealed. Anomalies associated with a first order transition to a commensurate collinear phase (AF1) are also observed at $T_{N1} = 213$ K. Our dielectric constant measurements confirm that only the spiral phase supports a spontaneous electric polarization. As well, we report on a spin-flop transition between 11 T - 13 T in the low temperature AF1 collinear phase with $\mathbf{B} \parallel \mathbf{b}$. Most of the experiments were carried out in Memorial University of Newfoundland with the exception of the high magnetic field (B > 7 T) measurements which are part of Professor Guy Quirion's short visit to l'Université de Sherbrooke. In addition, a non-local Landau-type free energy is developed for CuO and similar monoclinic multiferroics. In contrast with previous results of other groups, but in support of a recent proposal, our analysis clearly reveals the necessity for an incommensurate collinear phase (AF3) between the PM and the spiral AF2 states. Such a phase has been shown, both theoretically and experimentally, to occur in other geometrically frustrated antiferromagnets

where symmetry allows for uniaxial anisotropy at second order and in multiferroic compounds similar to CuO. We compare the model predictions to the B-T phase diagram of CuO obtained using ultrasonic velocity data. The same sequence of magnetic phase transitions is observed as in other multiferroic systems with spiral spin-driven ferroelectric order such as $MnWO_4$, $AMSi_2O_6$, some of the orthorhombic systems $RMnO_3$, the Kagomé-related compound $Ni_3V_2O_8$ and $LiCuVO_4$.

Acknowledgements

I wish to express my great appreciation to my supervisor, Professor Guy Quirion, who accepted me as his student and supported me along the course of this project, for constantly challenging me since the beginning and understanding my imperfect French. I owe most of the experimental work to him.

I am very grateful to my co-supervisor, Professor Martin L. Plumer, who decided to be part of this project at halfway and devotedly supported me along the last part of it. For the helpful discussion meetings and his guidance through the mathematical formalism, I owe most of the theoretical work to him.

I am thankful to both of them for being so patient to my naive scientific mind, for their suggestions and advice during the publication and thesis writing process, and their endless motivation.

I extend my thanks to Professor Mario Poirier for allowing my supervisor do some experiments with their facilities at l'Université de Sherbrooke. An important part of this project came out of those results and otherwise it would have been incomplete and less significant.

I acknowledge the collaboration with Professor Tsuyoshi Kimura from Osaka University, who generously provided the CuO sample immediately after we solicited.

I recognize the financial support from the School of Graduate Studies, the Department of Physics and Physical Oceanography, my supervisor, the CAP and my

parents. I appreciate the staff members of the Department of Physics and Physical Oceanography and the School of Graduate Studies for being there when needed.

Naturally, I admit this would have never been possible without my family's encouragement, specially from my parents, who never said no to any of my demands and persistently send me emails to catch up with my life. I am grateful to them and my friends for asking me the creative folly science questions, for making me laugh, for calling me every once in a while, for visiting me here in St. John's, for inviting me to adventures, for hosting me at their places, for teaching me all I would never learn in academia, and for having a good time with me.

Table of Contents

List of Tables

List of Figures

Chapter 1

Introduction

The transition metal monoxide cupric oxide (CuO) has been studied for more than 80 years due to its important and interesting physical properties. Despite the fact of being an apparent simple binary compound, the numerous studies carried out so far have not been enough to completely satisfy scientific curiosity. Initial research in 1929 on this compound began as a mere magnetic properties' characterization experiment [1]. Later, scientific interest was awakened in 1986 by the high-T_C superconductivity (HTSC) discovery of Bednorz and Muller at the IBM laboratories in Zurich [2]. With this breakthrough the cuprate family of superconductors was born and speculation arose regarding the role played by CuO_2 planes. One of the shared characteristics between CuO and the cuprates is the fact that they are insulators and order antiferromagnetically at high temperatures with magnetic moments ($\sim 0.67\ \mu_B$) significantly smaller than what is expected ($\sim 1\ \mu_B$) for $S = \frac{1}{2}$ localized spins.

In the first section of this chapter the outline of the thesis is given. In the second section a brief account of spin-driven magnetoelectric multiferroics is provided, followed by a section on frustrated magnetism. These two topics are closely related, and as shown later, associated with CuO. Therefore, a significant part of the Introduction

is devoted to their explanation. In the last section, I comment on some of the initial and final motivations in the course of this project.

1.1 Outline of thesis

Chapter 2 describes the particular properties of CuO such as the crystal structure, the magnetic properties, and its high-temperature magnetoelectric nature. The reader will find details on previous observations such as anomalous experimental results, anisotropy, 1-dimensionality, helimagnetism, magnetic frustration, and theoretical calculations.

In Chapter 3, the experimental setup is described together with an explanation of the technique. This includes the high-resolution ultrasound pulsed echo velocity measurements, the capacitance bridge dielectric constant measurements, the sample, and the low-temperature high magnetic field measurements.

In Chapter 4, the theoretical background associated with the experimental technique and the data analysis is explained. Elasticity theory is summarized and the concepts of exchange interactions and magnetoelastic coupling are introduced. This is important in order to understand how sound velocity measurements reveal magnetic phase transitions.

In Chapter 5, the relevant experimental data are presented and meticulously analyzed by comparing the temperature and magnetic field dependence of the sound velocity measured along the principal crystallographic directions. The two known phase transitions are observed at 213 and 230 K. Two additional phase transitions have been found: one close to 230 K with zero-field ($B = 0$) and the other as a spin-flop transition for $11 < B < 13.5$ T. Also, measurements of the dielectric constant along the **b** axis reveal the magnetoelectric coupling. All these measurements have been

used in order to determine the magnetic field-temperature phase diagram of CuO.

Chapter 6 is devoted to the description of the Landau model developed for the analysis of the magnetic properties of CuO. First, the general concepts of the theory are explained. Then, symmetry arguments are used to identify the possible anisotropic contributions. Finally, the model predictions are presented and discussed. In summary, the theoretical magnetic phase diagram reveals the stabilization of three zero-field and three high-field magnetically ordered states.

Finally, in the last chapter, the conclusions regarding the full project are enumerated and compared to previous theoretical and experimental results. Important remarks concerning the multiferroic mechanism in CuO, relative to other spin-driven multiferroics, are emphasized. As the proposed model is expected to be relevant for monoclinic mutliferroics in general, two other compounds are briefly discussed. At last, some future work is proposed.

1.2 Spin-driven magnetoelectric multiferroics

The induction of magnetization by an external electric field or the induction of an electric polarization by the application of a magnetic field, referred as the magnetoelectric effect, was predicted in the late 1800's by Pierre Curie [3] based on symmetry considerations [4]. By definition, the magnetoelectric effect involves electric and magnetic fields which restrict the observation of these phenomena to systems with no center of inversion [4]. However, a few decades of failed experimental attempts had to pass until Landau and Lifshitz realized that the magnetoelectric response is only allowed in systems where time-reversal symmetry is broken as well [5]. Then, Dzyaloshinskii demonstrated for the first time that the magnetoelectric effect is theoretically possible in Cr_2O_3 [6], which was experimentally confirmed in 1960 [7, 8, 9, 10]. This discov-

ery was particularly significant as it offers new technological applications based on the magnetoelectric effect: modulating devices, data storage and switching, optical diodes, spin waves generation, amplification and frequency converter [4]. However, the coupling strength and the physical properties of the existing magnetoelectric materials were not large enough until the 1990's when two new classes of magnetoelectric materials were introduced: composite materials and multiferroics [4].

In the composite materials, the magnetoelectric effect was primarily associated with structural transformations due to piezoelectric and magnetostrictive effects. In multiferroics, at least two of the four ferroic parameters exhibit long-range order. The first ferroic parameters were established by Smolenskiĭ *et al.* [11]: ferromagnetism and ferroelectricity; one was introduced by Hans Schmid [12]: ferroelasticity; and the last one defined by Manfred Fiebig [4]: ferrotoroidicity. In multiferroic crystals these orders can all coexist in a single phase crystal. The prefix ferro implies uniform order (zero wave vector), which is often accompanied by the formation of domains [13]. It comes from the family of first discovered magnetic materials (magnetites) which are mainly made of iron (ferrum in Latin) oxide. Later this prefix would be preserved as a convention to refer to uniform order of any type in matter. The more complex ordering is also included in this definition for all of the ferroic orders mentioned, such as: antiferromagnetic, antiferroelectric, etc. [4]. By single phase it is intended to mean solid, homogeneous and crystallized composition [14]. Thus, a ferroic order is described as a spontaneous macroscopic property, also called an order parameter, which is induced by the collective alignment of a microscopic property.

Until recently there were no known multiferroic materials with a magnetoelectric effect that was large enough for applications. In 2003, Kimura *et al.* [15] discovered a new type of multiferroic where ferroelectricity is induced by a spin-order (type-II), leading to a giant magnetoelectric and magnetocapacitive effects in the perovskite

manganite $TbMnO_3$. Unfortunately, most of the type-II multiferroics exhibit low Néel temperature (< 40 K), for reasons that will be more evident in Section 1.3.

So far, multiferroics can be classified in several groups: independent multiferroics, lone-pair multiferroics, geometrical multiferroics, spin-driven multiferroics, charge-ordered multiferroics, collinear multiferroics, etc [16]. The main differences between all these classes rely on the mechanism that induces ferroelectricity, the magnitudes of polarization, and more important, the magnitude of the magnetoelectric coupling. No description will be given for all of these multiferroic classes, however curious readers are invited to look at Ref. [16]. In general, multiferroics can be classified in two groups: type-I where ferroelectricity and magnetism have different sources and type-II where magnetism causes ferroelectricity and thus there is a prominent magnetoelectric coupling [17]. In particular, in the type-II, spin-driven ferroelectricity is induced by non-collinear magnetic structures. These are usually referred as spiral magnets because of the spiral-looking arrangement of the magnetic configuration.

There are different types of non-uniform magnetic structures with a long wavelength: sinusoidal, screw, cycloidal, and conical (see Figure 1.1). In a sinusoidally modulated spin structure, all magnetic moments are pointing in the same direction but with a modulated magnitude characterized by a wave vector $\mathbf{Q}$. When the spin rotation axis ($\mathbf{S}_i \times \mathbf{S}_j$) is parallel to $\mathbf{Q}$, as in Figure 1.1b, the arrangement yields a screw spiral, also called proper screw. If the spin rotation axis is perpendicular to $\mathbf{Q}$, the spin configuration is referred as a cycloidal spiral (see Figure 1.1c). In the conical structures a ferromagnetic component coexists with the screw or cycloidal spiral. More literature regarding the standard cycloid scenario can be found in Refs. [19, 20]. So far, the relevant interactions that can be responsible for the magnetoelectric effect are: single-ion anisotropy, symmetric superexchange, antisymmetric interactions, dipolar interactions, and Zeeman energy [4]. Several theoretical models have been de-

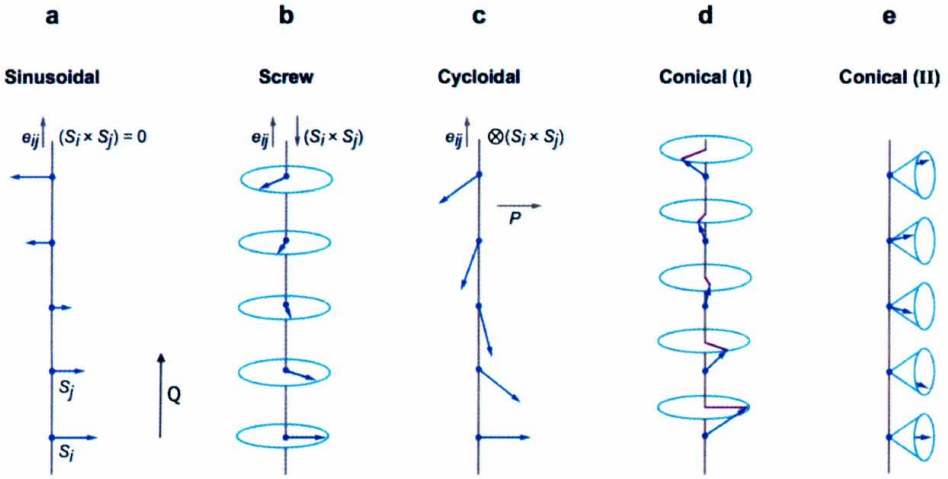

Figure 1.1: Magnetic structures in a 1D array of magnetic moments with a long wavelength: *a)* the collinear sinusoidal, *b)* the non-collinear screw (also known as proper-screw), *c)* cycloidal, *d)* conical longitudinal, and *e)* conical transverse. $\mathbf{e_{ij}}$ stands for a unit vector connecting the neighboring magnetic moments, $(\mathbf{S}_i \times \mathbf{S}_j)$ is the spin rotation axis, $\mathbf{Q}$ is the magnetic wave vector and $\mathbf{P}$ the electric polarization. Adapted by permission from Annual Reviews, Inc [18], copyright 2007.

veloped in order to explain the magnetoelectric effect associated with this long-range ordered magnetic structures. One of them is the Katsura-Nagaosa-Balatsky (KNB) microscopic model [21]. In this model, the magnetoelectric effect in non-collinear magnets is directly related to a spin current of the form $\mathbf{S}_i \times \mathbf{S}_j$. The phenomenological theory of the magnetoelectric effect, together with the origin of non-collinear magnetic ordering and its relation to ferroelectric orders, was discussed in the early 1960's by several groups [22, 23, 24, 6]. In a few words, magnetic frustration makes a single lowest-energy configuration of collinear spins impossible inducing a more exotic configuration such as a spiral spin structure instead. As a result, the spiral magnetic structure breaks inversion symmetry activating the antisymmetric DM-interaction. The DM-interaction term in the free energy leads to relativistic corrections that favor non-collinear ordering and are proportional to the spin-orbit coupling [20]. Then, the

DM-interaction forces the positive and negative ions to shift apart inducing the ferroelectric order [22, 23, 24, 25, 26]. In the KNB-model, the spin-orbit interaction and the non-collinear ordering is realized by competing exchange interactions, and there is no DM-interaction involved [21]. In general, both of these models give a relation for the electric polarization ($\mathbf{P}$) as follows

$$\mathbf{P} \propto \mathbf{e}_{ij} \times (\mathbf{S}_i \times \mathbf{S}_j), \tag{1.1}$$

where $\mathbf{e}_{ij}$ is a unit vector connecting neighboring magnetic moments and $\mathbf{S}$ is the magnetic moment associated with the ion. As emphasized, in both cases magnetic frustration plays a crucial role and this is the topic of the next section.

1.3 Frustrated magnetism

Frustrated magnetism is a rich field of new states and properties of matter that emerged from the new kind of insulator proposed by P.W. Anderson in the early 1970's [27]. Classically, the term frustration is understood as competing interactions hampering the minimization of the energy [28]. Initially, it was ascribed to quantum systems such as spin glasses, however, it was extended to other classes of materials after further studies. Generally, frustrated systems can have three different origins: quenched disorder, competing interactions, and geometry [28]. In the following, a brief account of frustrated magnetism due to geometry and competing interactions will be given as these two mechanisms are relevant to the area of multiferroics (a literature review can be found in Refs. [28, 29]).

In the case of frustrated multiferroic systems the frustration is often not too big. Nevertheless, it is responsible for exotic magnetic structures that can induce ferroelectric orders. The important consequences of this frustration are: low ordering temper-

ature, increased degeneracy of the ground state, and tendency to form non-collinear spin structures [30] (such as the ones just described in Section 1.2). Therefore, spin-driven magnetoelectric multiferroics manifesting magnetic frustration normally have a low Néel temperature.

In geometrical frustrated magnetism, a geometrical restriction, such as a triangular lattice, frustrates the magnetic moments. As shown in Figure 1.2, when two magnetic moments in a triangular antiferromagnet are collinearly aligned, the third moment is said frustrated since it cannot satisfy the antiferromagnetic exchange interaction with both of its nearest-neighbors simultaneously. Consequently, it costs less energy to rearrange all three moments in a 120° configuration, inducing a non-collinear magnetic state.

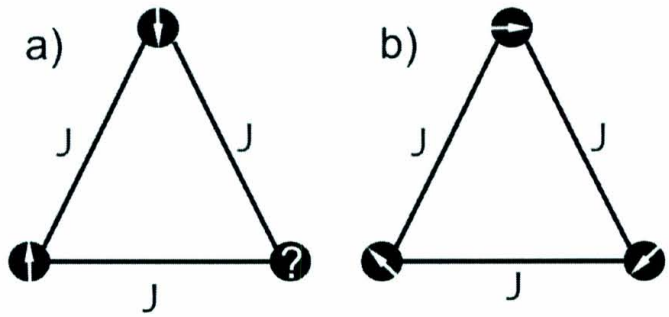

Figure 1.2: Magnetic frustration by geometry in a triangular lattice. J represents the exchange interaction. *a)* One magnetic moment is frustrated and unable to pick a direction. *b)* The magnetic moments get rearranged in a 120° configuration.

In the case of magnetic frustration by competition, for example in an antiferromagnetic square lattice, the competition arises between nearest-neighbors exchange (NN) - J_1 and next-nearest-neighbors (NNN) - J_2. If the NNN coupling is also antiferromagnetic and strong enough compared to the NN interaction, frustration can arise as in the J_1-J_2 checkerboard model [31]. This is also called the crossed chain model, that is often found in spin-liquids (see Figure 1.3).

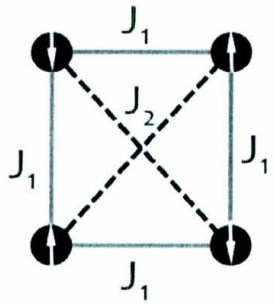

Figure 1.3: Square lattice magnetic frustration. The arrows represent spin-up and spin-down, J_1 and J_2 are the exchange interactions, different colors (solid lines/dashed lines) are used to represent different strengths of the exchange interactions.

1.4 Motivation

CuO is an unusual high-temperature magnetoelectric multiferroic ($T_N \sim 230$ K). As a result, people have been speculating about its magnetic properties and its high ordering temperature with the objective of finding out how to tailor high-temperature multiferroic compounds for new commercial applications. In Table 1.1 a list of several multiferroic compounds, together with some of their characteristics, is provided. The first one, $BiFeO_3$, is a model compound of the type-I multiferroics and one of the most studied due to its room temperature ferroelectric order. However, as it was mentioned before, in type-II multiferroics there is a stronger magnetoelectric coupling and higher values of spontaneous polarization have been discovered. Therefore, there are great expectations on these compounds, wherein CuO has one of the highest ferroelectric temperatures with a high spontaneous polarization according to a recent publication in 2008 [32].

Forsyth *et al.* [40] published a work on neutron diffraction in CuO and mentioned that the paramagnetic state unexpectedly condenses to a spiral antiferromagnetic state at $T_{N2} = 230$ K. As Giovannetti *et al.* [41] pointed out recently, from a theoretical

Table 1.1: List of some multiferroics. All of them with the exception of $BiFeO_3$ are type-II multiferroics. In the case of $CuFeO_2$ a magnetic field (B) has to be applied to reach the magnetoelectric state.

Compound	Structure	Ferroelectric temperature (K)	Spontaneous polarization (μC m^{-2})	Magnetic order	References
$BiFeO_3$	$R3c$	< 1103	75	type-I	[16]
CuO	$C2/c$	213-230	150	cycloidal	[32]
$MnWO_4$	$Pc/2$	7-12.5	55	"	[33]
$RMnO_3$	$Pbnm$	< 28	500	"	[15]
$LiCuVO_4$	$Pnma$	< 3	20	"	[34]
$LiCu_2O_2$	"	< 23	4	"	[35]
$Ni_3V_2O_8$	mmm	3.9-6.3	100	"	[36]
$AMSi_2O_6$	$C2/c$	< 6	14	?	[37]
$CuFeO_2$	$R\bar{3}m$	< 11	300($\mathbf{B}\perp\mathbf{c}$)	screw	[38]
$ACrO_2$	"	< 24	30	"	[39]

point of view, it is not clear what is the microscopic origin of the type-II multiferroicity in CuO. In other words, how is CuO a type-II multiferroic at high-T_N and what is the key ingredient for high-T_N type-II multiferroics? Tolédano *et al.* [42] made a comment on the unexpected sequence of magnetic phase transitions of CuO and developed a Landau model to try to understand the reasons for this behaviour. Their results revealed a strong coupling which is associated with strong magnetic frustration. On the contrary, Jin *et al.* [43] obtained a relatively weak frustration from their DFT calculations. All these theoretical studies [41, 42, 43] support the direct transition

from the paramagnetic to the spiral state. However, different from these studies, Sakhnenko *et al.* [44, 45] revealed the existence of what they call the "praphase" of magnetoelectrics. The "praphase" is a magnetic phase between the paramagnetic and the spiral phases. It has been suggested that CuO should exhibit this phenomenon, as it is the case for $MnWO_4$ and $CuCl_2$. They emphasized that this phase has not been yet observed in CuO and suggested some experimental work to support their theory.

A few experimental methods are adequate for this investigation and ultrasound is one of them. Experimental techniques that are traditionally used for the study of magnetic phase transitions in antiferromagnets are based on measuring physical properties such as the heat capacity, the magnetic susceptibility, sound velocity, etc. Measurements of the heat capacity and the magnetic susceptibility of CuO have been already published with no evidence of an intermediate phase. This can possibly be due to the lack of resolution. Measurements of the sound velocity are nonexistent and the high-resolution ultrasound technique is well suited to look for phase transitions as a result of the magnetoelastic coupling. Moreover, magnetic fields can be applied to observe the field dependence of the phase transitions in order to construct a magnetic field-temperature phase diagram of a single crystal CuO for the first time. Surprisingly, only one publication was found regarding a spin-flop transition in a powder sample [46]. Furthermore, the capacitance can be measured simultaneously with the sound velocity in order to detect magnetoelectric phase transitions. This approach is certainly appropriate for the fundamental physics of multiferroics and frustrated magnets such as CuO.

In the course of this project, two additional magnetic phases were found, a spin-flop transition to a high-field phase which coincides with previous susceptibility measurements on a powder sample [46] and an intermediate phase observed between the spiral

order and the paramagnetic state. A theoretical approach was chosen since no other experimental tool, for an extended study of this new magnetic states, was accessible. Landau theory has been used earlier for this class of materials and has provided good results that can account for the ultrasound experimental data of related magnetoelectric compounds [47, 48, 49]. It can provide a solid theoretical support for experimental findings. It is a good tool for analyzing phase transitions and sometimes it can give extra information about the nature of the phenomena such as specific details regarding the magnetic structures.

In summary, our ultrasound data revealed two magnetic phases, and Landau theory helped us learn more about the magnetic structures associated with them and confirm the proposed magnetic field-temperature phase diagram.

Chapter 2

Properties of CuO

As mentioned in the Introduction, CuO is associated with the HTSC cuprate family and it is a high-temperature magnetoelectric multiferroic. Moreover, other phenomena have been observed such as magnetic frustration, orbital ordering, quasi-1D antiferromagnetism, and it has been described as a strongly correlated system. Thus, for this project purpose, this chapter describes its crystal structure, the magnetic properties, and the magnetoelectric effect in CuO.

2.1 Crystal structure

As a transition metal monoxide, CuO is expected to have a fcc crystal structure as in its parent compounds, the type-II antiferromagnets (MnO, FeO, CoO, NiO), however it does not. This disparity can be attributed to the fact that Cu^{2+} is a d^9 Jahn-Teller ion and thus the rock salt structure is not energetically favorable due to the degeneracy of the orbitals d_{z^2} and $d_{x^2-y^2}$ [30, 50]. As a result the crystal structure is monoclinic with a C2/c (C_{2h}^6) No. 15 space group symmetry and lattice constants $a = 4.68$ Å, $b = 3.42$ Å, $c = 5.129$ Å and $\beta = 99.54°$ at room temperature [32]. The symmetrical crystallographic axis of the 2-fold rotation is the **b** axis, so $\mathbf{b} \parallel \mathbf{b}^*$. The

3D crystal structure can be seen as two zigzag chains with different Cu-O-Cu bond angles (see Figure 2.1). Therefore, different exchange interactions would be expected due to a different type of magnetic interactions and orbital overlapping.

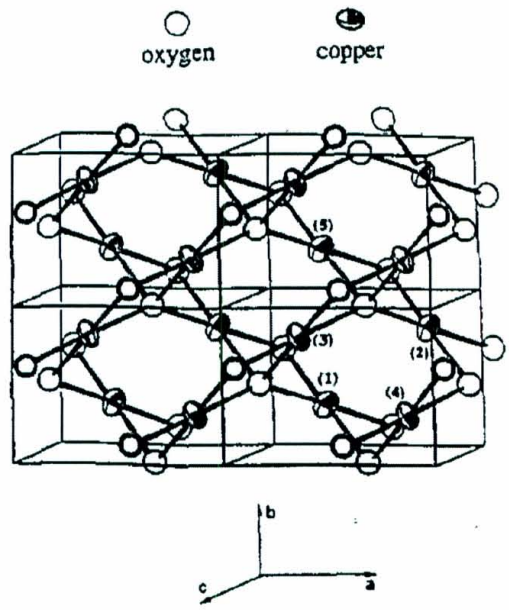

Figure 2.1: Four primitive cells of CuO, with four Cu-O groups in each unit cell, the numbers in parentheses distinguish different Cu ions. M. Aïn, A. Menelle, B. M. Wanklyn and E. F. Bertaut, Magnetic structure of CuO by neutron diffraction with polarization analysis. J. Phys.: Condens. Matter 4 (1992) 5327-5338. IOP Publishing Ltd. [51].

Figure 2.2 is a sketch of one CuO sheet normal to the **b** axis, with the red atoms representing the Cu^{2+} ions and the green ones O^{2-} ions. Note that in the crystal there are two of these CuO sheets per unit cell with an AB stack configuration. The angles for the two zigzag chains along the [101] and [10$\bar{1}$] directions are specified in this figure.

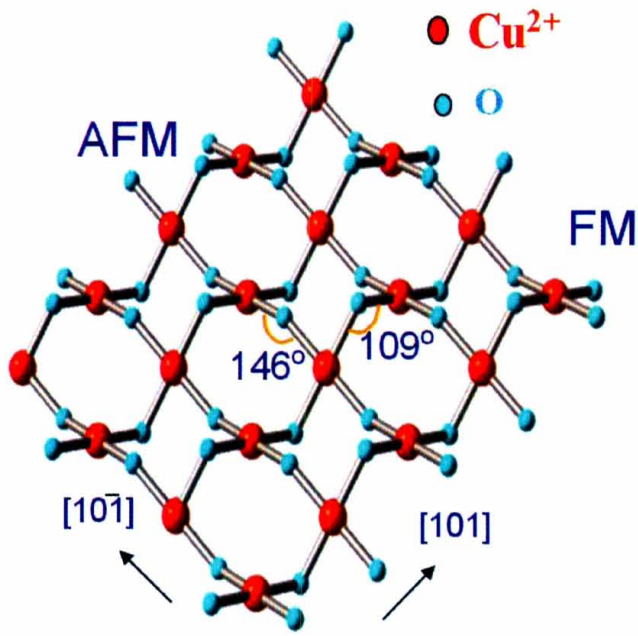

Figure 2.2: Crystal structure of CuO. Adapted by permission from Macmillan Publishers Ltd: Nature Materials [32], copyright 2008.

2.2 Magnetic properties

CuO is a magnetic material containing Cu^{2+} magnetic ions that have a $3d$ hole with an orbital moment that is expected to be quenched. As a result, it has been considered as an isotropic spin-only $S = \frac{1}{2}$ system. However, neutron scattering publications [40, 52] reported a considerably lower moment of $\sim$ 0.65 μ B in the low-temperature phase, where 1 μ B is expected for a spin-only Cu^{2+} ion. Naturally, this indicates that CuO is by far a more complicated system than the isotropic spin-only $S = \frac{1}{2}$ system. In particular, the crystal structure has four main different angles which are associated with four superexchange interactions. The two dominant J_1 and J_2 are described in Figure 2.1 and Table 2.1 [53]. It has been noted that a value of 69 meV is estimated for a 1D antiferromagnetic (AFM) Heisenberg chain [54] in agreement

with the fact that J_1 has the largest angle $\sim 145.82°$ along the $[10\bar{1}]$ direction. With this in mind, the magnitude of the strongest superexchange interaction, J_1, has been derived from experimental data and two different values have been obtained: 67 meV [55] and 91 meV [56]. The second strongest superexchange interaction, J_2, is ferromagnetic with an angle of 108.85° along the [101] direction and no experimentally derived value was found in literature. However, a manifold of magnitudes for these exchange interactions, and other possible ones, have been proposed by different density functional theory (DFT) calculations [41, 43, 57, 58] in agreement with a quasi-1D AFM.

Table 2.1: Angles of superexchange interactions at room temperature. The magnitude of J_1 is the average value derived from different experimental studies [55, 56]. The magnitude of J_2 is an estimation resulting from the averaging of the $\frac{J_2}{J_1}$ ratios given in Refs. [41, 43, 57].

Bond	Cu(2)-O-Cu(3)	Cu(1)-O-Cu(4)
Exchange	J_1	J_2
Angle	145.82°	108.85°
(meV)	79	$\sim$ -9.5

In superexchange the coupling between two cations (Cu^{2+}) is mediated through a non-magnetic anion (O^{2-}). When the angles along the bonds are close to 180° the helimagnetic structure has strong antiferromagnetic interactions and when it approaches 90° weak antiferromagnetic interactions are expected by the Goodenough-Kanamori rule [59]. A rough sketch illustrating the frustration in CuO is shown in Figure 2.3. The NN are coupled by the exchange interactions J_3 and J_4 with a different **b** coordination. The NNN can be defined as a first-NNN coupled by the FM superexchange J_2 and a second-NNN coupled by the AFM superexchange J_1. Thus, since the second-NNN exchange is much stronger than the NN coupling, frustrated magnetism is caused by competing interactions and the lattice stabilizes crossed AFM-chains and

FM-chains inducing a spiral magnetic order relative to the layered **b** planes [51]. Notice that J_1 and J_2 are the dominant interactions and they do not lead to frustration within the CuO sheet as all couplings are fully satisfied (see Figure 1.3). However, due to the C-type monoclinic structure, the next plane along the **b** direction (in orange) forms an AB stack structure with neighboring planes (in red). As a result, these magnetic moments are frustrated since they cannot satisfy an antiferromagnetic interaction (or ferromagnetic) simultaneously with its neighbours.

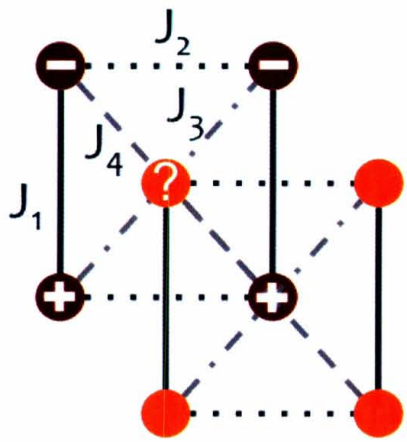

Figure 2.3: Frustration in CuO arises from the overlapping **b** plane magnetic Cu^{2+} ions. Plus/minus represent in/out magnetic moments, red/orange are planes with different **b** coordination, J_1 is AFM (continuous line), J_2 is FM (dotted line), and J_3 (dash-dotted line) / J_4 (dashed line) are frustrated.

Furthermore, high-resolution powder x-ray diffraction suggested relatively small variations of the lattice constants with temperature [60]. This lattice distortion, attributed to the displacement of O atoms along the **b** axis and the chains, could significantly vary the value of the superexchange couplings and therefore induce more competition while the temperature is changed [50, 61, 62]. The temperature dependence of these exchange interactions has been speculated based on mid-IR experiments, theoretical investigations, and resonant soft x-ray magnetic scattering [63, 64, 65].

Consequently, besides being a distorted version of the frustrated fcc AFM (the transition metal monoxide family), the Jahn-Teller distortion accounts for orbital order and the competing interactions give rise to helimagnetism, providing to CuO several sources of magnetic frustration. Whether this frustration is weak or strong remains an open question.

On another matter, early magnetic susceptibility measurements revealed an anomalous behaviour (see Figure 2.4). Instead of the usual Curie-Weiss dependence ($\chi \sim T^{-1}$), a broad maximum at 550 K and a dominant exchange interaction along the AFM-chain was observed in the paramagnetic state [46, 56], see Figure 2.4 [46]. This is in agreement with the initial consideration of CuO as a 1D AFM. Further investigations showed magnetic excitations above $\sim$ 230 K (again, in the paramagnetic state) in neutron scattering studies [55, 66, 67], magnetic susceptibility measurements [68, 69, 70], and an infrared study [64]. These results are strong evidence that CuO is a quasi-1D Heisenberg AFM mainly due to the AFM-chains presenting important anisotropic effects.

From measurements of the heat capacity [1] and magnetic susceptibility [71] two phase transitions have been identified ($\sim$ 215 K and $\sim$ 230 K). An example of the magnetic susceptibility data of a CuO single-crystal is presented in Figure 2.5. Two pieces of information can be extracted from this figure. First, the transition at $\sim$ 230 K, labeled T_{N1}, is clearly of second order appearing as a cusp whereas at $\sim$ 212 K, T_{N2}, a first order transition with a step-like behaviour is observed. Second, CuO is magnetically anisotropic since the measurements undoubtedly depend on the direction. Additionally, anisotropic behaviour was observed along the **b** axis, the AFM-chains and the FM-chains, in neutron scattering studies [67, 72, 73], magnetic susceptibility measurements [69, 70], an infrared study [50], high-resolution x-ray diffraction [60], electric polarization measurements [32, 65], and resonant soft x-ray magnetic scatter-

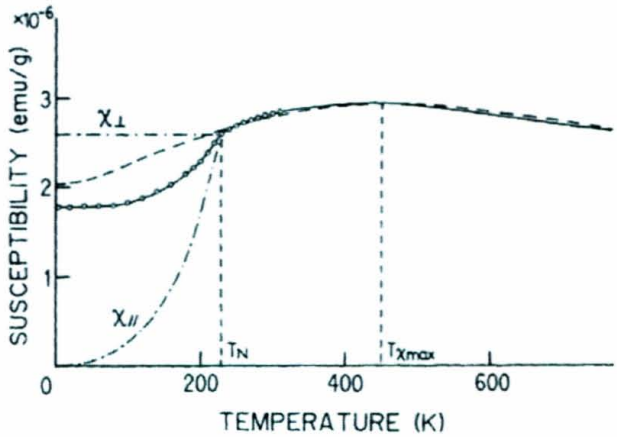

Figure 2.4: Magnetic susceptibility measurements of CuO powder. The dotted line shows the estimated 1D curve from Ref. [54]. Reprinted by permission from the Journal of Physical Society of Japan, Vol. 57, No. 10, pp. 3293, copyright 1988, O. Kondo, M. Ono, E. Sugiura, K. Sugiyama and M. Date, Figure 2. [46]

ing [65]. It is important to emphasize that, despite the obvious anisotropic character of CuO, only two theoretical studies have explicitly considered the anisotropy as an important contribution to their Hamiltonian Heisenberg model [43, 58].

These phase transitions are of a magnetic nature and thus attributed to different magnetic orders. Neutron diffraction experiments on single-crystals with polarization analysis have been used to resolve the spin configurations. First, Yang *et al.* [55] corroborated the magnetic susceptibility measurements of a single-crystal by finding a second order magnetic phase transition at T_{N1} from a paramagnetic state to an AFM spiral state and a first order phase transition from the AFM spiral state to an AFM collinear state. Then, below $T_{N1} \sim 213$ K the magnetic structure was resolved as a commensurate collinear state with the magnetic moments along the monoclinic **b** axis (easy axis). In this magnetic state, there are two characteristic chains: an AFM-chain along the $[10\bar{1}]$ direction (see Figure 2.6 [32]) and a FM-chain along $[101]$, with a commensurate modulation vector $\mathbf{Q}_{CM} = [\frac{1}{2}\ 0\ -\frac{1}{2}]$. Note that the **b** axis

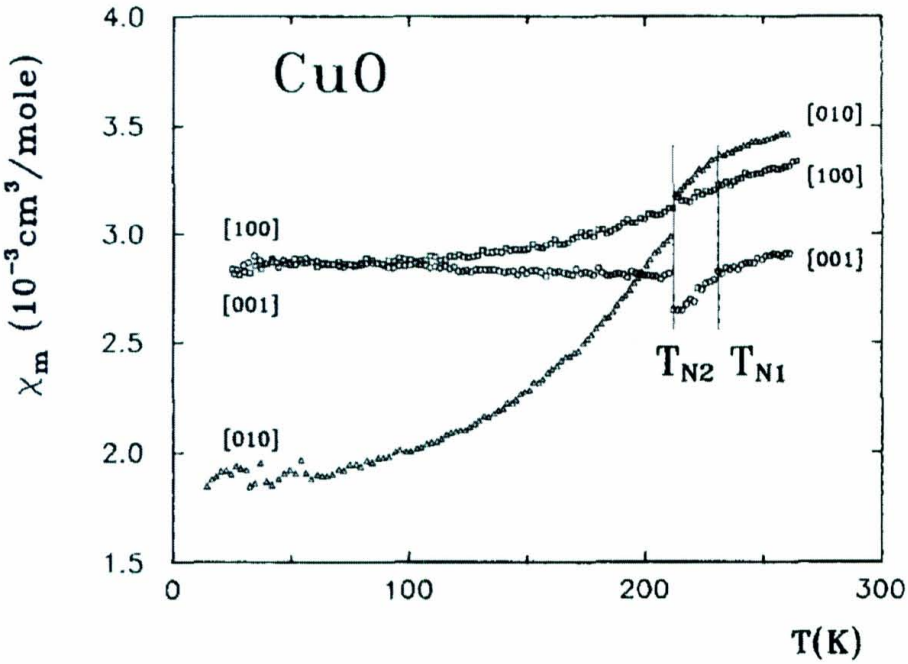

Figure 2.5: Magnetic susceptibility measurements of a CuO single-crystal along the three crystallographic axes. In the left side of the figure [100] is on the top. Springer and Zeitschrift für Physik B - Condensed Matter, 82, 1991, 383, On the magnetic anisotropy of CuO, U. Köbler and T. Chattopadhyay, Figure 1, with kind permission from Springer Science and Business Media. [68]

is the symmetrical crystallographic axis and the magnetic easy axis. As the temperature increases, a phase transition occurs, at $T_{N2} \sim 230$ K, to an incommensurate cycloidal spiral (non-collinear) state with half of the magnetic moments in the *ac* plane with $\mathbf{Q}_{ICM} = [0.506\ 0\ -0.483]$ and a spiral plane parallel to the **b** axis and $\mathbf{v} = 0.506\mathbf{a}^* + 1.517\mathbf{c}^*$ [51]. Notice that in Figure 2.6 two different **b** planes are shown with no distinction, the consecutive AFM-chains $[10\bar{1}]$ belong to a different plane. For example, in the AF2 phase the magnetic moments that are pointing along the **b** axis correspond to a different plane from those pointing in the *ac* plane. Another remark is that the difference between these two pointing directions of the magnetic moments

appears to be 90°.

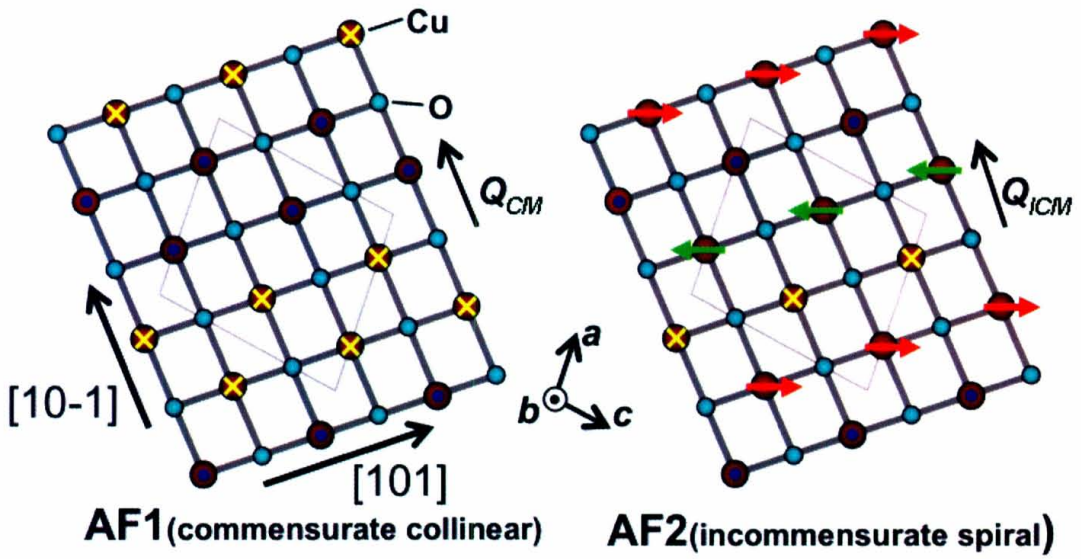

Figure 2.6: Magnetic structures of CuO, the cross means a magnetic moment pointing into the page and the dot a magnetic moment pointing outside the page. Adapted by permission from Macmillan Publishers Ltd: Nature Materials [32], copyright 2008.

2.3 Magnetoelectric effect

CuO has been used for several applications such as a pigment in ceramic, dietary supplement in animals etc. Recently, in 2008, scientific interest in CuO was awakened when Kimura *et al.* [32, 26] discovered the multiferroic nature of CuO. It was then classified as a magnetoelectric (type-II) multiferroic [74]. The mechanism responsible for the induced ferroelectricity was explained as a cycloidal scenario, since the spiral plane is nearly parallel to **Q** and the spontaneous electric polarization **P** is parallel to the **b** axis. The magnetic susceptibility was again measured in a single-crystal and anomalies in the dielectric constant revealed a transition that could correspond to a ferroelectric order in the spiral state (see Figure 2.7 [32]). No anomalies were

observed along directions different from the **b** axis. The ferroelectric order was then confirmed by electric polarization measurements along the **b** axis as a function of temperature, shown in Figure 2.8 [32]. For these measurements the crystal was subject to an electric field of 117 kV/m in the paramagnetic phase and then cooled down to the spiral state (poling process). Then the electric field is removed and finally the pyroelectric current, which is a discharge current resulting from a warming process, is registered as a function of temperature [75]. Finally, the pyroelectric current is integrated to calculate the spontaneous electric polarization. This study indicates that a ferroelectric order coexists with the AFM spiral state between 213 K $< T <$ 230 K. Moreover, the transition from the paraelectric to the ferroelectric states is of second order whereas an abrupt drop (first order phase transition) is observed at 213 K.

The induced ferroelectricity in the cycloidal scenario is in accord with proposed models such as the Dzyaloshinskii-Moriya (DM) interaction and KNB-model [21, 76, 77]. However, other theoretical models have been suggested over the past two years to justify the high-temperature of the multiferroic state (AF2) compared to most spin-driven multiferroics. Tolédano *et al.* [42] developed a theoretical description for the unusual sequence of transitions based on an irreducible representation analysis and a Landau type free-energy, with some antisymmetric DM-interaction type terms. They obtain dramatic results such as two consecutive first order phase transitions despite what has been demonstrated experimentally. Babkevich *et al.* [78] have introduced what they call a ferroaxial crystal class where **P** is induced through the coupling between the chirality of a magnetic structure and a structural rotation. They proved that the chiral magnetic order is coupled to the ferroelectric order, but there is no evidence of such a structural rotation yet (see Table 2.2).

As can be seen, the ferroaxial model is based on a DM-interaction, with a similar Hamiltonian, the main difference is the term with the chirality $\sigma_{n,n+1}\mathbf{e}_{n,n+1}$. This

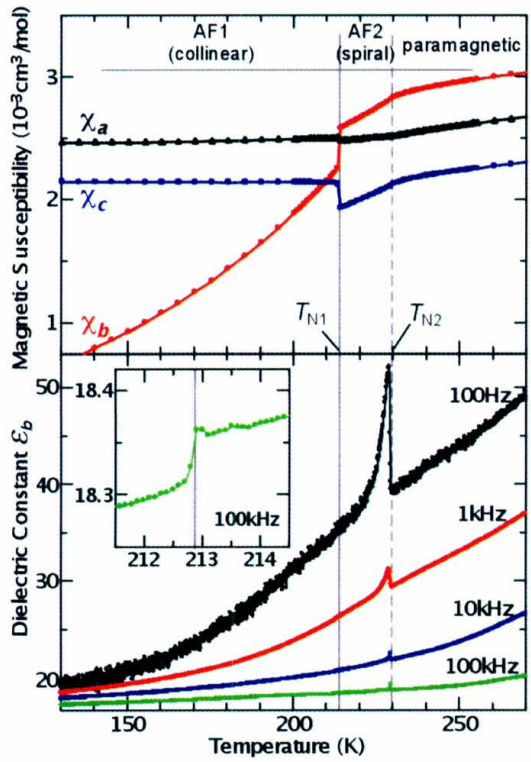

Figure 2.7: Magnetic susceptibility and dielectric constant measurements of CuO from Ref. [32]. The inset shows a magnified view at 100 kHz for the dielectric constant around T_{N1}. Adapted by permission from Macmillan Publishers Ltd: Nature Materials [32], copyright 2008.

term is the coupling between the chiral magnetic order and the predicted structural rotation. Since this term does not exist in the traditional DM-interaction, the energy associated with this coupling involves a different mechanism.

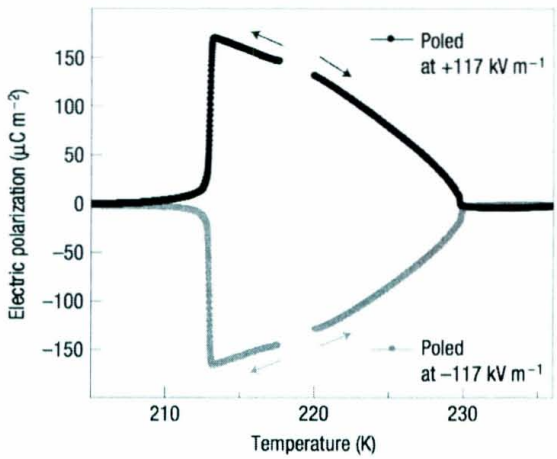

Figure 2.8: Electric polarization along the **b** axis of CuO. The arrows indicate the direction of the temperature sweep. Reprinted by permission from Macmillan Publishers Ltd: Nature Materials [32], copyright 2008.

Table 2.2: Models for the induced spontaneous electric polarization in CuO. $\mathbf{P}$ is the electrical polarization, λ is a coupling term, $\mathbf{u}$ are the oxygen displacements, $\mathbf{e}$ is a unit vector connecting two sites, $(\mathbf{S}_n \times \mathbf{S}_{n+1})$ is a spin current, and $\sigma = \pm 1$ is the chirality of the magnetic structure.

Model	Hamiltonian term
DM-interaction [76, 77]	$H_{DM} = \sum_n \lambda(\mathbf{u}_{n+\frac{1}{2}} \times \mathbf{e}_{n,n+1}) \cdot (\mathbf{S}_n \times \mathbf{S}_{n+1})$
Ferroaxial DM [78]	$H_{DM} = \sum_n (\mathbf{P}_{n,n+1} \times \mathbf{e}_{n,n+1} + \sigma_{n,n+1}\mathbf{e}_{n,n+1}) \cdot (\mathbf{S}_n \times \mathbf{S}_{n+1})$

Chapter 3

Experimental Setup

For the experimental part of this project, two main instruments were necessary: a high-resolution interferometer and a capacitance bridge. The high-resolution interferometer is used for ultrasonic velocity measurements with a pulse echo method; the first section explains the technique and the setup involved. In Section 3.2, the capacitance bridge, used to measure the dielectric constant temperature dependence, is described. Then, the experimental configuration in order to carry out simultaneous dielectric and ultrasonic velocity measurements is illustrated. Finally, a few details are given regarding the "low" temperature and high magnetic fields experimental considerations.

3.1 Ultrasonic measurements and interferometer

For this investigation, sound velocity measurements have been used in order to probe the macroscopic physical properties of CuO. Since the sound velocity depends on the restoring forces between atoms, any variation of these forces has an effect on the value of the velocity. As a result, any type of phase transition (structural, magnetic, electric, etc.) is in principle measurable by this technique. In the case of CuO, as the magnetic moments are localized on ions, the sound velocity is sensitive to the coupling

between the lattice and the spin, also called the magnetoelastic coupling. Therefore, the technique deserves explanation since it is used to interpret our results. Figure 3.1 is a diagram of the high-resolution (1 ppm) acoustic interferometer.

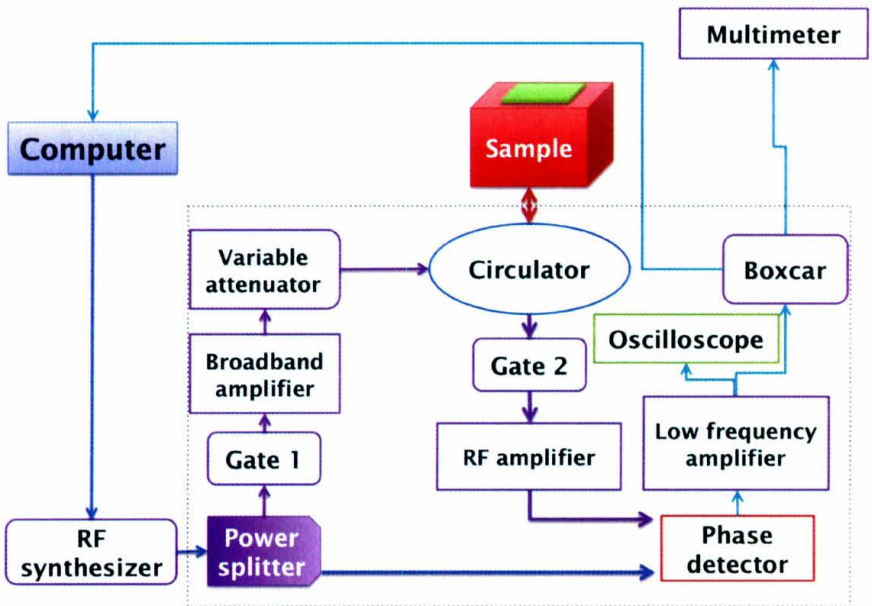

Figure 3.1: Setup with the high-resolution acoustic interferometer inside the dotted box.

The interferometer has one input (the RF synthesizer) and one output (the computer). First of all, the frequency synthesizer provides a continuous signal which is split into two equal power signals by the power splitter (referred to as the sample and the reference signal). Gate 1 is used to shape the sample signal into a ~ 0.4 μs low power pulse at a repetition rate of $\sim$ 1kHz, which is then amplified by a 1 W broadband amplifier. The pulse power is then adjusted using a variable attenuator. The sample signal is then directed to the sample via the circulator, the role of this element is to prevent a high power signal to be reflected back to the synthesizer. The sample signal is converted to an acoustic wave by a piezoelectric transducer via the inverse piezoelectric effect. After a round trip a fraction of the acoustic echo energy

is converted into a RF signal by the piezoelectric effect using the same transducer (reflection configuration). These processes are not simultaneous and cannot interfere with each other. In gate 2, the initial pulse is filtered to prevent the saturation of the RF amplifier. Then, the sample and the reference signals are compared in the phase detector (mixer) which gives a signal proportional to the phase shift between both signals. A boxcar is used instead of a voltmeter since the signal is not continuous and the boxcar can do the measurement in given periods of time. Also, this boxcar is part of a retroactive loop where the computer keeps the phase difference equal to zero by changing the frequency of the RF signal, so that during the experiment the in-phase condition is fulfilled, $\frac{\Delta\phi}{\phi} = 0$.

As the phase difference (ϕ_n) depends on the time of flight Δt_n, the time for a round trip (transducer to transducer) of the acoustic wave in the sample, the phase shift simply reduces to

$$\phi_n = 2\pi\frac{\Delta t_n}{T} = 2\pi f \Delta t_n = \frac{4\pi n l f}{v}, \tag{3.1}$$

where $f = \frac{1}{T}$ is the frequency of the signal ($\sim$ 30 MHz). In the ideal case, multiple echoes are observed on the oscilloscope at different times. Thus, the n^{th} echo has a time of flight $\Delta t_n = \frac{L}{v}$, where L is the distance traveled ($L = 2nl$ for reflection mode, where l is the length of the sample) and v is the sound velocity at a frequency f (see Figure 3.4). For any echo, the relative phase difference variation can be derived from the last expression leading to

$$\frac{\Delta\phi}{\phi} = \frac{\Delta l}{l} + \frac{\Delta f}{f} + \frac{\Delta v}{v}. \tag{3.2}$$

In general, as the sample expansion ($\frac{\Delta l}{l}$) as a function of temperature or field is smaller than the relative sound velocity variation ($\frac{\Delta v}{v}$) by a factor 10. Therefore,

the measured relative frequency variation ($\frac{\Delta f}{f}$) can be related to the relative velocity variation using

$$\frac{\Delta f}{f} \simeq \frac{\Delta v}{v}, \tag{3.3}$$

whenever $\frac{\Delta \phi}{\phi} = 0$. The high-resolution relies on the fact that the RF synthesizer is stable at 10 Hz and the frequency of operation is 30 MHz $\rightarrow$ resolution $= \frac{10 \text{ Hz}}{30 \text{ MHz}} < 1$ ppm. Thus, small anomalies can be observed by measuring relative sound velocity variations.

3.2 Capacitance Bridge and dielectric constants

Sound velocity measurements can be used to gain information about physical properties coupled to the lattice. In our case, we are trying to detect phase transitions and their nature. As described in Section 2.3, the observation of a spontaneous electric polarization, via pyroelectric current measurements [32], revealed that the order between 213 and 230 K in CuO is also ferroelectric. Moreover, it has been shown that this magnetoelectric active phase can also be identified using dielectric constant measurements [32, 15] which show a distinct anomaly at the critical temperature.

The dielectric data have been obtained using an extremely accurate and stable AH 2550A Ultra Precision 1 kHz capacitance bridge. The measurable properties are the capacitance and the loss (component of the impedance that is 90° out of phase). The accuracy is around 5 ppm with a resolution of 0.5 attofarad (an atto is 10^{-18}). The operating frequency is 1 kHz with a 30 ms minimum limit for repeated measurements. Figure 3.2 is a rough diagram of the full setup with the inclusion of the Capacitance Bridge. As can be seen, everything is controlled by the computer in a way that repeated simultaneous measurements are achieved. The Capacitance Bridge operation

is based on the balance between a controllable capacitor ($C_\circ$), a pseudo-resistor ($R_\circ$), and the impedance to be determined. A microprocessor minimizes the voltage across a detector connected to the controllable and unknown capacitances. The electronic circuit allows one to independently balance the resistive (R_x) and capacitive (C_x) components of the unknown impedance using

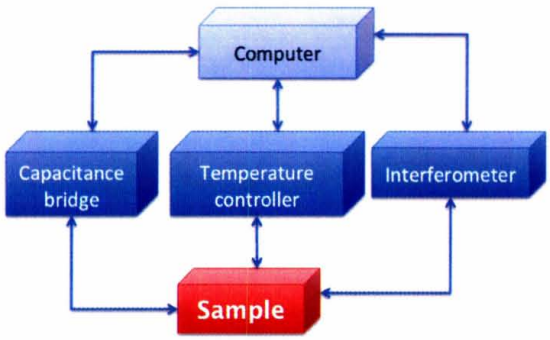

Figure 3.2: Full setup.

$$\frac{C_x}{C_\circ} = \frac{V_1}{V_2}, \tag{3.4}$$

$$\frac{R_x}{R_\circ} = \frac{V_2}{V_1}, \tag{3.5}$$

where V_1 is the voltage for the controllable branch, and V_2 is the voltage for the unknown branch. The high precision relies on the three-terminal connection where the unknown impedance is measured between the central conductors of the BNC coaxial connectors that is used between the capacitance bridge and the sample. A shielding surrounding the connections avoids undesired capacitance added to the actual value.

3.3 Sample preparation, transducers, and electrodes

For velocity measurements, plane acoustic waves were generated using 30 MHz $LiNbO_3$ piezoelectric transducers bonded to the crystal faces. These transducers operate by the inverse piezoelectric and the piezoelectric effect for the transmission and reception of sound waves. In the inverse piezoelectric effect an acoustic wave is generated by a mechanical stress caused by an applied electric field. This is due to the alignment, induced by the electric field, of the electric dipole moments giving rise to strain. The transducers can be of two kinds: longitudinal or transverse. Longitudinal transducers generate acoustic waves with a polarization parallel to the direction of propagation. Transverse transducers generate acoustic waves with a polarization perpendicular to the direction of propagation. Therefore, for every direction of propagation we have access to three independent polarizations.

For the purpose of this study a CuO sample was grown using a floating zone technique as described in Ref. [32] by Kimura *et al.* in Osaka University. A single crystal was cut with faces perpendicular to the monoclinic axes $\mathbf{a}^*$, $\mathbf{b}^* = \mathbf{b}$, and $\mathbf{c}^*$ ($4 \times 4 \times 3$ mm^3) (see Figure 3.3). The sample was then polished to obtain parallel faces in order to avoid nonparallelism effects and ensure a good bonding with the transducers. For the transmission configuration two transducers, mounted on opposite faces, are necessary while only one transducer is used for the reflection configuration. As the capacitance measurements require the use of electrodes, custom-made brass plates were bonded on opposite faces (see Figure 3.4). These electrodes were bonded to the faces perpendicular to the $\mathbf{b}$ axis since this direction (ϵ_b) is the one showing the largest variation at the magnetoelectric phase transition. Therefore, simultaneous sound velocity variations and dielectric constant measurements are possible for most of the acoustic modes with the exception of those where acoustic waves are propagating along the $\mathbf{b}$ axis. Previous alginment of the sample was performed by our collaborators

in Osaka University.

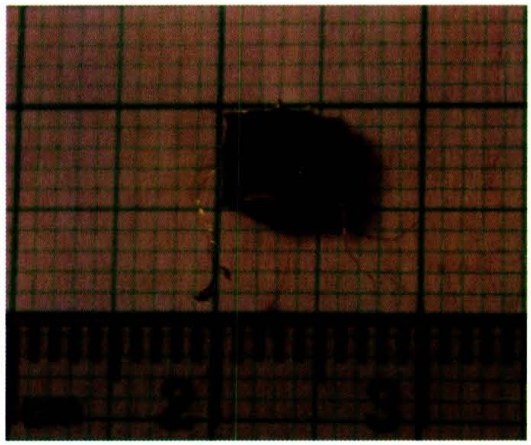

Figure 3.3: CuO single crystal sample.

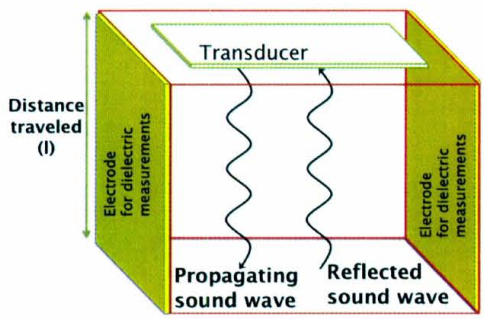

Figure 3.4: Reflection configuration.

3.4 Low-temperature and high magnetic fields

The range of temperature of interest is 200 to 240 K; however, some measurements were carried out at lower temperatures for exploration purposes. Cryogenic liquids are involved in all of our experiments for decreasing the temperature and especially for high magnetic fields using a superconducting magnet. Naturally, cryostats were

used in this investigation with liquid nitrogen and liquid helium as cryogenics. At Memorial University of Newfoundland, magnetic fields up to 7 T were applied whereas at l'Université de Sherbrooke magnetic fields up to 16 T were attained. High magnetic fields were indispensable for the investigation of the magnetic phase diagram of CuO. The temperature control is crucial as well, this system uses an algorithm called PID control (for Proportional-Integral-Differential). The tuning of three variables allows to adjust the power input of the heater in order to stabilize the temperature at a specific value or at a desired rate of change.

Chapter 4

Crystalline Elasticity

Crystalline elasticity plays an important role in measuring the sound velocity by associating the elastic constants with the measured sound velocities. This chapter summarizes the part of elasticity theory that is necessary to understand the sound velocity measurements carried out for this thesis. We begin by describing the basic principles of static elasticity, then continue with a brief explanation of dynamic elasticity where the Christoffel equation is derived and close with the concepts of exchange interactions and magnetoelastic coupling. It is assumed that the reader is familiar with the subjects of Hooke's, Newton's and Curie's laws, symmetry operations, and Hund's rules. For more details regarding the sections about static and dynamic elasticity the reader is invited to have a look at the Refs. [79, 80, 81] and for the section on the exchange interactions and magnetoelastic coupling at Refs. [82, 83].

4.1 Static elasticity

The collective deformations in a solid are called strain and are labeled e. First we will limit our description to one-dimensional systems for simplicity and later fully extend the description to three-dimensional systems.

When a force F is exerted on a solid, a change in length from L to L' is observed as in Figure 4.1. Since this deformation is not necessarily macroscopically homogeneous, it is instead defined over a small portion, where it is assumed to be homogeneous when taking the infinitesimal limit.

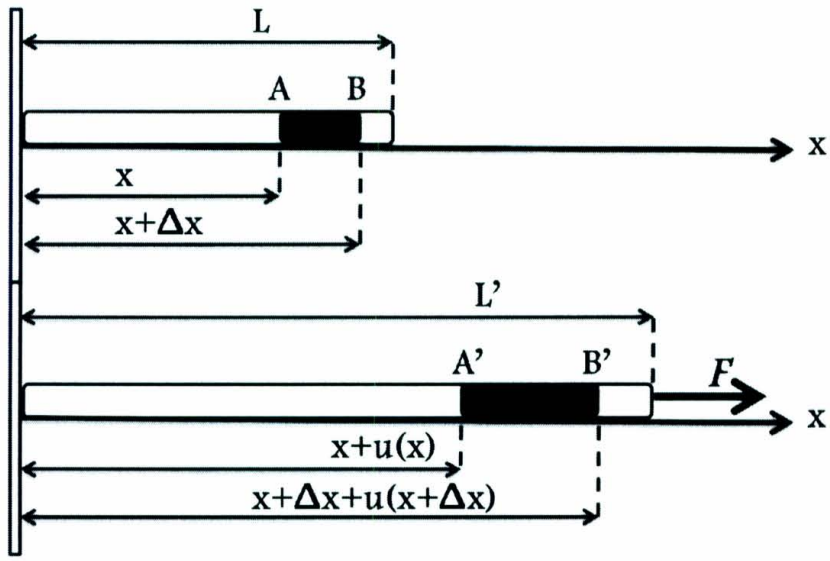

Figure 4.1: 1D deformation of a string.

From Figure 4.1, for a segment $\overline{AB} = \Delta x$, the deformation induced by the force changes the segment to $\overline{A'B'}$. The local deformation at x is labeled as $u(x)$ and at $x + \Delta x$ is $u(x + \Delta x)$, and therefore the relative deformation on Δx is

$$\frac{\overline{A'B'} - \overline{AB}}{\overline{AB}} = \frac{u(x + \Delta x) - u(x)}{\Delta x}. \tag{4.1}$$

By definition, the strain of the string at x (which is dimensionless) is the limit when $\Delta x \to 0$

$$e = \lim_{\Delta x \to 0} \frac{u(x + \Delta x) - u(x)}{\Delta x} = \frac{du}{dx}. \tag{4.2}$$

In three dimensions the local deformations can occur in all possible directions. Hence, we use a x_i where $i = 1, 2$, and 3 represent the indices of the coordinate system. Therefore, we now have a vector deformation $\mathbf{u}(x_i)$ and thus

$$du_j = \frac{\partial u_j}{\partial x_i} dx_i, \tag{4.3}$$

where the summation from 1 to 3 over repeated indices is used. The square of the distance between two points ($d\mathbf{x}' = d\mathbf{x} + d\mathbf{u}$) is now

$$(d\mathbf{x}')^2 = (d\mathbf{x})^2 + 2(d\mathbf{x}) \cdot (d\mathbf{u}) + (d\mathbf{u})^2. \tag{4.4}$$

If the scalar product is expanded

$$(d\mathbf{x}')^2 - (d\mathbf{x})^2 = 2\ dx_i\ du_i + du_k\ du_k, \tag{4.5}$$

and substituting for du using Eq. 4.3,

$$(d\mathbf{x}')^2 - (d\mathbf{x})^2 = 2\frac{\partial u_i}{\partial x_j} dx_i\ dx_j + \frac{\partial u_k}{\partial x_i}\frac{\partial u_k}{\partial x_j} dx_i\ dx_j. \tag{4.6}$$

Permuting the indices i, j leaves the sum unchanged, so Eq. 4.6 can be rewritten in a symmetrical form

$$(d\mathbf{x}')^2 - (d\mathbf{x})^2 = \left[\frac{\partial u_i}{\partial x_j} + \frac{\partial u_j}{\partial x_i} + \frac{\partial u_k}{\partial x_i}\frac{\partial u_k}{\partial x_j}\right] dx_i\ dx_j = 2\ e_{ij}\ dx_i\ dx_j, \tag{4.7}$$

with

$$e_{ij} = \frac{1}{2}\left[\frac{\partial u_i}{\partial x_j} + \frac{\partial u_j}{\partial x_i} + \frac{\partial u_k}{\partial x_i}\frac{\partial u_k}{\partial x_j}\right]. \tag{4.8}$$

The nine elements of e_{ij} constitute the strain second rank tensor. Assuming that the

deformations are small, or that the relative variations of distances are

$$\frac{\partial u_i}{\partial x_j} << 1, \tag{4.9}$$

the second order term $\frac{\partial u_k}{\partial x_i}\frac{\partial u_k}{\partial x_j}$ is negligible. This reduces the strain tensor to

$$e_{ij} = \frac{1}{2}\left[\frac{\partial u_i}{\partial x_j} + \frac{\partial u_j}{\partial x_i}\right], \tag{4.10}$$

where it is obvious that $\frac{\partial u_i}{\partial x_j}$ and $\frac{\partial u_j}{\partial x_i}$ are interchangeable, so the strain tensor is further reduced to six components

$$e_{ij} = e_{ji}. \tag{4.11}$$

Therefore, the general matrix form is

$$e = \begin{pmatrix} e_{11} & e_{12} & e_{13} \\ e_{12} & e_{22} & e_{23} \\ e_{13} & e_{23} & e_{33} \end{pmatrix}. \tag{4.12}$$

These constants can be classified in two groups due to the nature of their physical meaning. For $i = j$, we have longitudinal deformations along the i direction while for $i \neq j$ the strain elements e_{ij} correspond to shear deformations (see Figure 4.2).

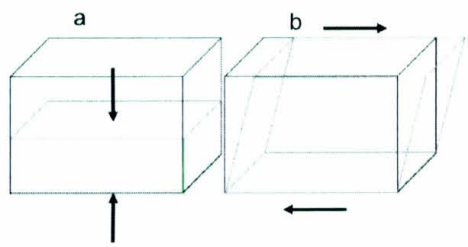

Figure 4.2: a. Longitudinal deformation. b. Shear deformation.

Now that we understand how to describe a deformation, we have to find a way to define the forces acting on and within a solid (also called stress). Using the same logic as for the strain, we can think of an infinitesimal force $\Delta\mathbf{F}$ acting on an arbitrary infinitesimal area $\Delta\mathbf{A}$. One can think of this as a generalization of the definition of pressure: $p = \frac{F}{A}$. This analogy is valid since the direction of $\mathbf{F}$ could make any angle with the vector defining A. Let ΔF_i be the i^{th} component of $\mathbf{F}$ exerted on the area element ΔA_k, which is perpendicular to the $\mathbf{k}$ axis, in the positive direction. The stress (T_{ik}) is defined as the limit, when ΔA_k goes to zero of the ratio $\frac{\Delta F_i}{\Delta A_k}$

$$T_{ik} = \lim_{\Delta A_k \to 0} \frac{\Delta F_i}{\Delta A_k}, \tag{4.13}$$

where T_{ik} are the stress components that constitute a second rank tensor as the strain. Thus, T_{ik} is the i^{th} component of the stress on a unit area perpendicular to j. Here we assume that the solid is initially in static equilibrium, as a result the net force acting on the crystal is necessarily equal to zero. Thus the sum of the torques about any point is zero as well. By "initially" we refer to first Newton's law of motion which says that every object continues in its state of rest unless compelled to change that state by an external force. In other words, if it is initially in static equilibrium it will remain in static equilibrium since we are not applying any net external force. As a result, the stress tensor is also symmetric

$$T_{ij} = T_{ji}, \tag{4.14}$$

leading to the same conclusions as for the strain. There are only six independent constants for a crystal with no symmetry, besides the identity symmetry (E).

From Hooke's law we know that the length of a spring is directly proportional to the applied force ($F = -kx$ where k is the spring constant). This can be translated

to our elasticity terminology as the strain being proportional to the stress. Therefore, this can be rewritten as stress-strain relation

$$T_{ij} = C_{ijkl} e_{kl}, \tag{4.15}$$

where $i,\ j,\ k,\ l\ =\ 1,\ 2,\ 3$ for the three coordinates system and C_{ijkl} stands for the elastic constants. Thus, the elastic tensor has 81 components C_{ijkl} that constitute the elastic stiffness fourth rank tensor. However, since e_{kl} and T_{ij} are symmetrical (Eqs. 4.11 and 4.14), and from Hooke's law, the elastic potential ($U = \frac{1}{2}kx^2$ is rewritten as in Eq. 4.18) imposes a strain energy independent of the path. Thus C_{ijkl} will necessarily have several symmetries as well

$$e_{kl} = e_{lk}, \tag{4.16}$$

$$T_{ij} = T_{ji}, \tag{4.17}$$

$$U = \frac{1}{2} C_{ijkl} e_{ij} e_{kl} = \frac{1}{2} C_{klij} e_{kl} e_{ij}, \tag{4.18}$$

$$C_{ijkl} = C_{klij} = C_{jikl} = C_{ijlk}, \tag{4.19}$$

leaving only 21 independent components. We take advantage of this symmetry by using the Voigt notation $(i,\ j,\ k,\ l) \rightarrow (\alpha\ \beta)$, where pair of indices are replaced accordingly to $(11) \rightarrow 1$, $(22) \rightarrow 2$, $(33) \rightarrow 3$, $(23) = (32) \rightarrow 4$, $(13) = (31) \rightarrow 5$, $(12) = (21) \rightarrow 6$. Then, the elastic constants C_{ijkl} can be represented by a 6×6 matrix

$$C = \begin{pmatrix} C_{11} & C_{12} & C_{13} & C_{14} & C_{15} & C_{16} \\ C_{12} & C_{22} & C_{23} & C_{24} & C_{25} & C_{26} \\ C_{13} & C_{23} & C_{33} & C_{34} & C_{35} & C_{36} \\ C_{14} & C_{24} & C_{34} & C_{44} & C_{45} & C_{46} \\ C_{15} & C_{25} & C_{35} & C_{45} & C_{55} & C_{56} \\ C_{16} & C_{26} & C_{36} & C_{46} & C_{56} & C_{66} \end{pmatrix}. \tag{4.20}$$

Since the symmetry operations of a crystal represent transformations (rotations, symmetry with respect to a point or a plane, etc...) that keep the crystal unchanged from the reference frame regardless of the orientation, the physical properties of the crystal should remain unchanged as well. Therefore, the three tensors e_{kl}, T_{ij}, and $C_{\alpha\beta}$ need to be invariant under any symmetry operation associated with the crystal in question. Consequently, the number of independent components is usually reduced, with the exception of triclinic point groups. For example, the generating elements of the monoclinic space group C2/c are C_{2y} (2-fold rotation with respect to the **y** axis) and I (Inversion) [84]. For the case of the elastic stiffness tensor, the invariant condition is [80]

$$C_{ijkl} = \alpha_i^m \alpha_j^n \alpha_k^o \alpha_l^p C_{mnop}, \tag{4.21}$$

where α_i^m, α_j^n α_k^o, and α_l^p represent the elements of one symmetry operation and are given by the following matrices

$$\alpha_{(I)} = \begin{pmatrix} -1 & 0 & 0 \\ 0 & -1 & 0 \\ 0 & 0 & -1 \end{pmatrix} \tag{4.22}$$

and

$$\alpha_{(C_{2y})} = \begin{pmatrix} -1 & 0 & 0 \\ 0 & 1 & 0 \\ 0 & 0 & -1 \end{pmatrix}. \tag{4.23}$$

The inversion symmetry does not reduce the tensor since $x_i \rightarrow -x_i$ and this is an even product (for example, $xxxx \rightarrow xxxx$). However, C_{2y} changes $x \rightarrow -x$ and $z \rightarrow -z$ while y does not change ($y \rightarrow y$). Therefore, elements with an odd product of x and z must be zero in order to keep the tensor invariant (for example, C_{14} (C_{xxyz}) = C_{36} (C_{zzxy}) = 0). The elastic stiffness tensor is then reduced to

$$C = \begin{pmatrix} C_{11} & C_{12} & C_{13} & 0 & C_{15} & 0 \\ C_{12} & C_{22} & C_{23} & 0 & C_{25} & 0 \\ C_{13} & C_{23} & C_{33} & 0 & C_{35} & 0 \\ 0 & 0 & 0 & C_{44} & 0 & C_{46} \\ C_{15} & C_{25} & C_{35} & 0 & C_{55} & 0 \\ 0 & 0 & 0 & C_{46} & 0 & C_{66} \end{pmatrix}. \tag{4.24}$$

4.2 Dynamic elasticity

Whenever there is a restoring force giving rise to equilibrium in a physical system, this system can be used as a medium of propagation. In our case, we will limit our study to acoustic waves propagating in solids and we start by defining a force density

$$f_i = \frac{\partial T_{ij}}{\partial x_j}, \tag{4.25}$$

responsible for producing a local acceleration (atomic displacements away from equilibrium). According to Newton's second law of motion ($\mathbf{F} = m\mathbf{a}$)

$$f_i = \rho \frac{\partial^2 u_i}{\partial t^2} = \frac{\partial T_{ij}}{\partial x_j}, \tag{4.26}$$

where ρ is the mass density. We can now use the stress-strain relation Eq. 4.15 with the definition of strain from Eq. 4.8 ($e_{kl} = \frac{du_k}{dx_l}$) and substitute

$$\rho \frac{\partial^2 u_i}{\partial t^2} = \frac{\partial (C_{ijkl} e_{kl})}{\partial x_j} = C_{ijkl} \frac{\partial^2 u_k}{\partial x_j \partial x_l}. \tag{4.27}$$

For plane waves, the solution to this equation is

$$u_i = u_{0i} e^{i(\mathbf{k}\cdot\mathbf{r} - \omega \mathbf{t})} \quad i = 1, 2, 3, \tag{4.28}$$

where $u_{0i} = u_{0l}\delta_{il}$ is the wave polarization (or the particle displacement direction), while $\mathbf{k}$ is the wave vector and ω the frequency. When we substitute Eq. 4.28 in Eq. 4.27 we get

$$(\rho\omega^2 \delta_{il} - C_{ijkl} k_j k_k) u_{0l} = 0, \tag{4.29}$$

which is possible to simplify by using the expression of the phase velocity ($v = \frac{\omega}{k}$)

$$(\rho v^2 \delta_{il} - C_{ijkl} n_j n_k) u_{0l} = 0. \tag{4.30}$$

This is the Christoffel equation, where n_j and n_k represent the cosine direction of the wave vector relative to the proper axis of the crystal system. We can imagine a dummy second rank tensor, $\Gamma_{il} = C_{ijkl} n_j n_k$, and solve for the velocity of sound waves in the secular equation where ρ is assumed to remain constant

$$|\Gamma_{il} - \rho v^2 \delta_{il}| = 0. \tag{4.31}$$

This relation (Eq. 4.31) between the elastic constant tensor and the acoustic wave velocities is what we use in the next chapter to associate the ultrasonic velocity measurements with CuO elastic constants.

4.3 Exchange interactions and magnetoelastic coupling

In order to understand antiferromagnets, it is necessary to consider the magnetic interaction between magnetic moments. As pointed out by Ashcroft and Mermin [82], the term magnetic exchange interaction is used to describe the dependence of the energy due to the relative orientation of two or more magnetic moments. The origin of this interaction is usually electrostatic electron-electron interaction. Other sources of magnetic interactions, such as magnetic dipole-dipole interaction and spin-orbit coupling, are often weak compared to the electrostatic interaction. As a reference, numerical values of magnetic dipolar interaction energy and electrostatic energy in a magnetic solid given in Ashcroft and Mermin [82] are 10^{-4} eV, and a fraction of an eV, respectively. Regarding the spin-orbit coupling in transition metal ions from the iron group, Curie's law is obeyed when some modifications are done to Hund's rules due to a crystal field splitting phenomenon known as quenching of the orbital angular momentum ($L \equiv 0$). The quenched orbital moment in these transition metal ions occurs because their partially filled d-shells are strongly influenced by the crystalline environment. This crystal field is much larger than the spin-orbit coupling so that to a first approximation the spin-orbit coupling could be ruled out. However, one must include terms that break rotational symmetry in spin space, such as dipolar interactions or spin-orbit, in order to take into account anisotropic coupling.

In a simple two electron system the linear combination of the four spin states leads

to one state with $S = 0$ known as singlet and three states with $S = 1$ known as the triplet. The associated lowest eigenvalues are E_s for the singlet and E_t for the triplet, then the ground state depends on whether E_s is less than or greater than E_t. A spin Hamiltonian operator can then be expressed, representing the molecular system as a simple linear combination of four lowest states, to analyze the energetics of spin configurations. The eigenvalues are the same as the four-state system Hamiltonian and the eigenfunctions give the spin of the corresponding states. In the case of the two electron system, each electron spin operator satisfies

$$\mathbf{S}_i^2 = \frac{1}{2}\left(\frac{1}{2} + 1\right) = \frac{3}{4}, \tag{4.32}$$

giving a total spin

$$\mathbf{S}^2 = (\mathbf{S}_1 + \mathbf{S}_2)^2 = \frac{3}{2} + 2\mathbf{S}_1 \cdot \mathbf{S}_2. \tag{4.33}$$

Since the eigenvalue of $\mathbf{S}^2$ is $S(S+1)$ in state S, it follows that the operator $\mathbf{S}_1 \cdot \mathbf{S}_2$ has the eigenvalue $-\frac{3}{4}$ in the singlet state and $\frac{1}{4}$ in the triplet states. As a result, the spin Hamiltonian operator is constructed

$$H = \frac{1}{4}(E_s - 3E_t) - (E_s - E_t)\mathbf{S}_1 \cdot \mathbf{S}_2, \tag{4.34}$$

where the first term can be omitted by redefining the zero energy, giving

$$H = -J\mathbf{S}_1 \cdot \mathbf{S}_2, \tag{4.35}$$

with $J = E_s - E_t$. In this convention, $J < 0$ when the singlet state has the lower eigenvalue which is related to antiparallel spins and $J > 0$ when the triplet state has the lower eigenvalue which is related to parallel spins. Thus, the Heisenberg spin

Hamiltonian summed over all pairs of ions is

$$H = -\sum J_{ij}\mathbf{S}_i \cdot \mathbf{S}_j, \tag{4.36}$$

where J_{ij} are known as the exchange interactions.

Magnetoelastic coupling can be accounted for by allowing variation of the exchange interactions with interionic distance [83]. Assuming there is a distortion from the equilibrium positions ($\mathbf{r}_0$) in the paramagnetic state (similar to Section 4.1)

$$\mathbf{r} = \mathbf{r}_0 + \mathbf{u}(\mathbf{r}_0), \tag{4.37}$$

the exchange interaction can be expressed to a low order as

$$J(\mathbf{r}' - \mathbf{r}) = J(\mathbf{r}'_0 - \mathbf{r}_0) + [\mathbf{u}(\mathbf{r}'_0) - \mathbf{u}(\mathbf{r}_0)] \cdot \nabla J(\mathbf{r}_0) + ... \tag{4.38}$$

With the expansion

$$\mathbf{u}(\mathbf{r}') = \mathbf{u}(\mathbf{r}) + \tau_i \frac{\partial \mathbf{u}}{\partial r_i} + ..., \tag{4.39}$$

where $\tau = \mathbf{r}' - \mathbf{r}$, $i = x, y, z$ and the summation convention is used. The relation in Eq. 4.38 is then expressed as

$$J(\tau) \cong J(\tau_0) + e_{ij}K_{ij}(\tau_\mathbf{0}), \tag{4.40}$$

where e_{ij} are the strain components. The symmetric magnetoelastic coupling coefficients are then given by

$$K_{ij}(\tau_0) = \frac{1}{2}\left[\frac{\partial J}{\partial r_i}\tau_j + \frac{\partial J}{\partial r_j}\tau_i\right]_0. \tag{4.41}$$

Such a coupling term provides a mechanism for ultrasound measurements to probe the magnetic states of solids.

Chapter 5

Experimental Data

The acoustic modes were studied, using the sound velocity measurements, in order to identify anomalies associated with phase transitions that are presented herein. Exhaustive velocity measurements as a function of temperature and magnetic field were carried out and dielectric measurements were used as support to avoid ambiguity for a magnetoelectric analysis. A thorough study of the transverse mode propagating along the $\mathbf{a}^*$ axis polarized along the $\mathbf{c}^*$ axis, hereafter called $V_{a^*}[c^*]$, helped determine the magnetic phase diagram for $\mathbf{B} \parallel \mathbf{b}$. This mode in particular shows the foremost evidence of a new magnetic phase transition. First, some characteristics of the temperature dependence of the acoustic modes are pointed out. Then, the behaviour with applied magnetic fields and dielectric constant measurements are presented. Finally, the experimental magnetic phase diagram is described.

5.1 Temperature dependence

Fig. 5.1 shows the relative sound velocity for the longitudinal mode propagating along the $\mathbf{a}^*$ direction (V_a^*). The heating and cooling processes are presented since the anomalies are dependent on whether we are increasing or decreasing the tempera-

ture. Two anomalies, associated with phase transitions, are clearly visible in both of the curves. The transition at the lower temperature (213 K) is identified as T_{N1} while the one at $\sim$ 230 K is labeled as T_{N3} for reasons that will be established in next section. The way we identify the transition temperatures is the following: the transition temperature is where a clear peak or dip is observed, or the mid point in step-like anomalies. As it can be seen, the anomaly at T_{N1} has a different behaviour for the heating and cooling cycles. We attribute this phenomenon to a first order transition based on previous measurements on other compounds which exhibit a similar hysteretic behaviour [85, 86]. Moreover, magnetic neutron scattering measurements [55] revealed hysteresis around this transition. In elasticity theory it can be associated with crystal domains developing with the lattice relaxation when changing the temperature. In this case, it might be related to the fact that T_{N1} is the crossover from a ferroelectric to a paraelectric state. Furthermore, the step-like anomaly is consistent with a first order phase transition, which is evident from susceptibility measurements [46]. An explanation of this argument will be given in Ch. 6 based on Landau theory for phase transitions. The other anomaly observed at $T_{N3} = 230$ K manifests a continuous variation (second order) and, contrary to what we observe at T_{N1}, it is independent of the temperature sweeping process.

Fig. 5.2 shows the transverse mode propagating along the **b** direction polarized along the $\mathbf{a}^*$ axis ($V_b[a^*]$). Again, the anomaly observed at T_{N1} has a step-like behaviour corroborating the argument of being a first order transition. Also, there is a small anomaly at T_{N3} showing a temperature dependence similar as the one obtained for the longitudinal mode V_{a*}. However, the slope of $V_b[a^*]$ is steeper compared to V_{a*} indicating more stiffness associated with the magnetoelastic coupling. In a paramagnetic phase, one mechanism for the temperature dependence of the sound velocities comes from the theory of lattice vibrations when anharmonic terms in the

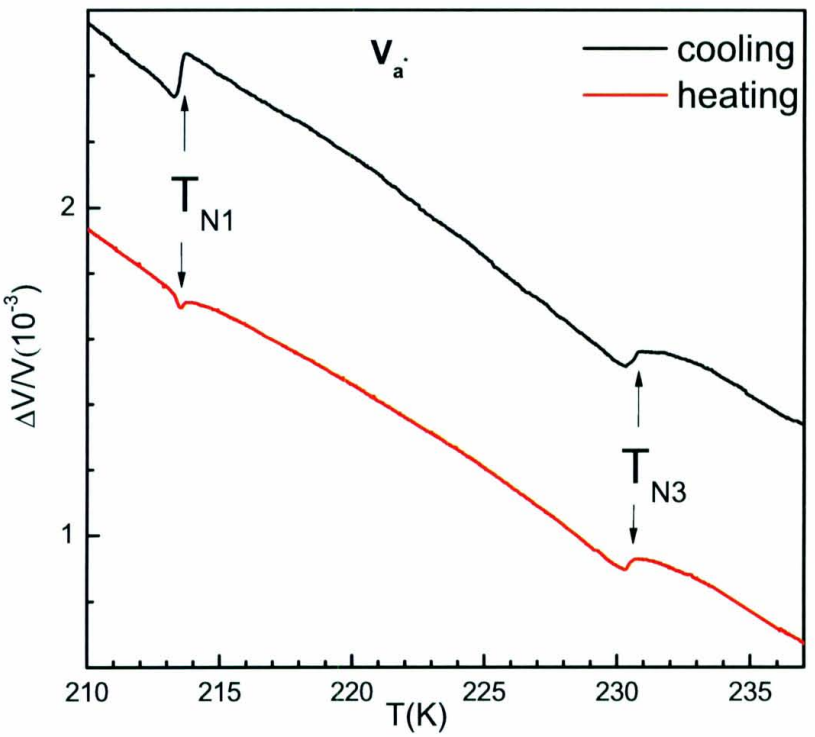

Figure 5.1: V_{a^*} acoustic mode for the cooling and heating process.

interatomic displacements are taken into account [87]. For example, in three-phonon processes the anharmonic effect involves higher order interactions of phonons where one phonon causes a periodic elastic strain modulating in space and time the elastic constant (sound velocity), a second phonon perceives the modulation and is scattered to produce another third phonon. Therefore, the stiffening is commonly associated with the population of phonons. In this case, the evident change of slope at the magnetic ordering temperature (T_{N3}) is an indication of the magnetoelastic coupling contribution. Otherwise, the slope would remain the same as designated by the dotted line.

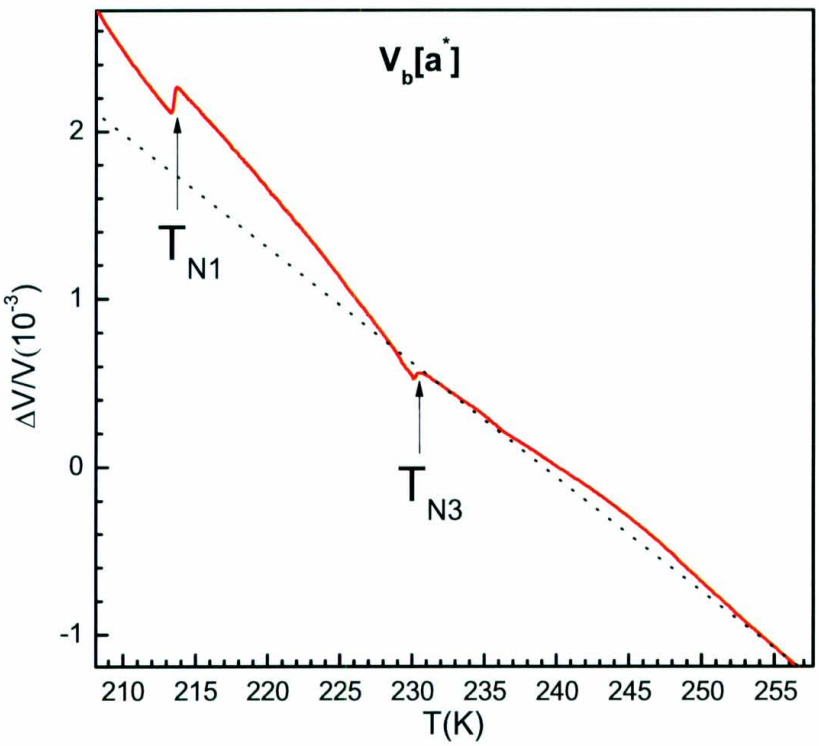

Figure 5.2: $V_b[a^*]$ acoustic mode for the heating process, the dotted line is to guide the eye and show the difference between the paramagnetic and first magnetically ordered states.

Fig. 5.3 shows the temperature dependence in the region of T_{N2} of six transverse acoustic modes. The curves were arranged purposely in this order to compare the data between equivalent acoustic modes. For example, the two acoustic modes on the top, $V_{c^*}[b]$ and $V_b[c^*]$, have similar slopes and anomalies. The two modes in the middle, $V_b[a^*]$ and $V_{a^*}[b]$, have exactly the same slopes and a slightly different behaviour for the phase transition anomaly. As well, the two modes on the bottom, $V_{c^*}[a^*]$ and $V_{a^*}[c^*]$, are congruently equivalent. Besides the fact that the anomaly is larger for these two modes, they reveal evidence of a smaller anomaly that is later, in

the next section, proven to be another transition. Notice that the last curve is a bit shifted in temperature, the reason for this is that these data have been obtained from experiments done at l'Université de Sherbrooke. Since these experiments were carried out using another probe, the temperature gradients that depend on the position of the thermometer are slightly different and thus the transitions are observed at different temperatures. For $V_{c^*}[a^*]$ and $V_{a^*}[c^*]$ it is hard to tell which is T_{N2} due to the fact that two small humps are observed. Therefore the transition is assumed to be in the mid point.

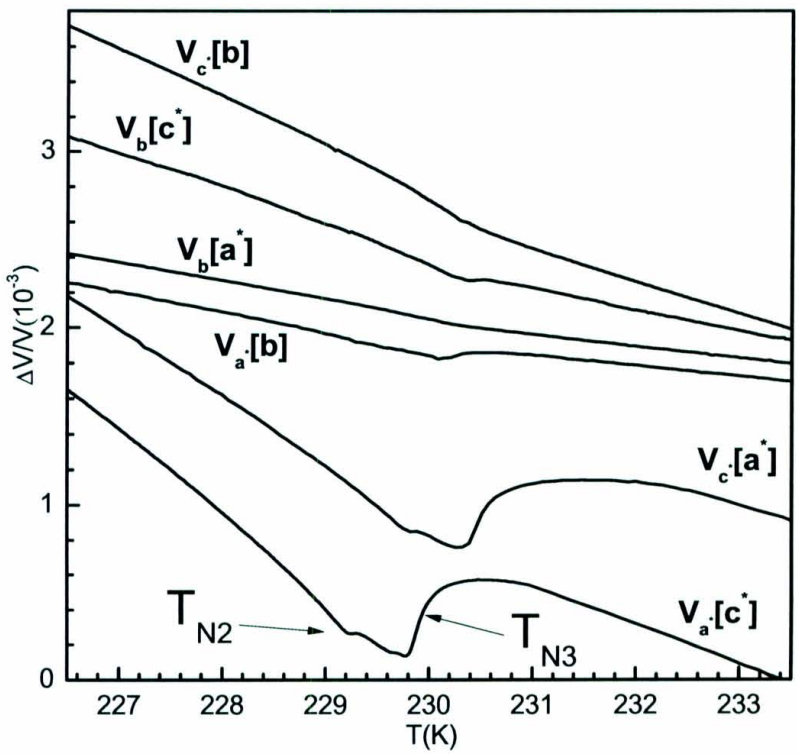

Figure 5.3: Transverse acoustic modes for the cooling process.

Despite several attempts, the longitudinal mode propagating along the **b** axis could

not be measured due to a poor signal in the reflection or transmission configuration. The longitudinal mode along the $\mathbf{c}^*$ axis was measured; however no useful data could be obtained. Anomalies associated with T_{N1} were observed for all transverse modes but they were not as significant as those already presented (data not shown).

5.2 Magnetic field and dielectric constants dependence

In Figure 5.4 we present the results for simultaneous ultrasonic velocity and dielectric constant measurements in black and green, respectively. Magnetic fields were applied along the **b** axis up to 7 T for the simultaneous measurements and up to 16 T for the ultrasonic velocity measurements only. The data corresponds to the transverse acoustic mode propagating along the $\mathbf{a}^*$ axis and polarized along the $\mathbf{c}^*$ axis ($V_{a^*}[c^*]$). In the inset we show the magnetic field dependence in the temperature range of $T_{N1} = 213$ K for the cooling process. The two step anomaly indicates a different magnetic ordering process from that previously reported. The paramagnetic transition was thought to occur at 230 K. In our measurements a new small anomaly, in close proximity to another much larger anomaly, is observed. Thus our high-resolution velocity measurements for $\mathbf{B} \parallel \mathbf{b}$ reveal two indisputable anomalies near the stabilization of the spiral order at $T \sim 230$ K. We ascribe these anomalies to two phase transitions, $T_{N2} = 229.3$ K and $T_{N3} = 230.0$ K. Previously, these phase transitions were thought to occur at a single transition and most probably overlooked due to the small temperature range in which this intermediate phase exists. As the field increases, the amplitude of the step-like variation observed at $T_{N2} = 229.3$ K, as well as the temperature difference between T_{N2} and T_{N3} increases. This confirms the existence of a new intermediate magnetic order AF3. The magnetic field was also

applied along the $\mathbf{a}^*$ and $\mathbf{c}^*$ axes and no field dependence was observed (results not shown).

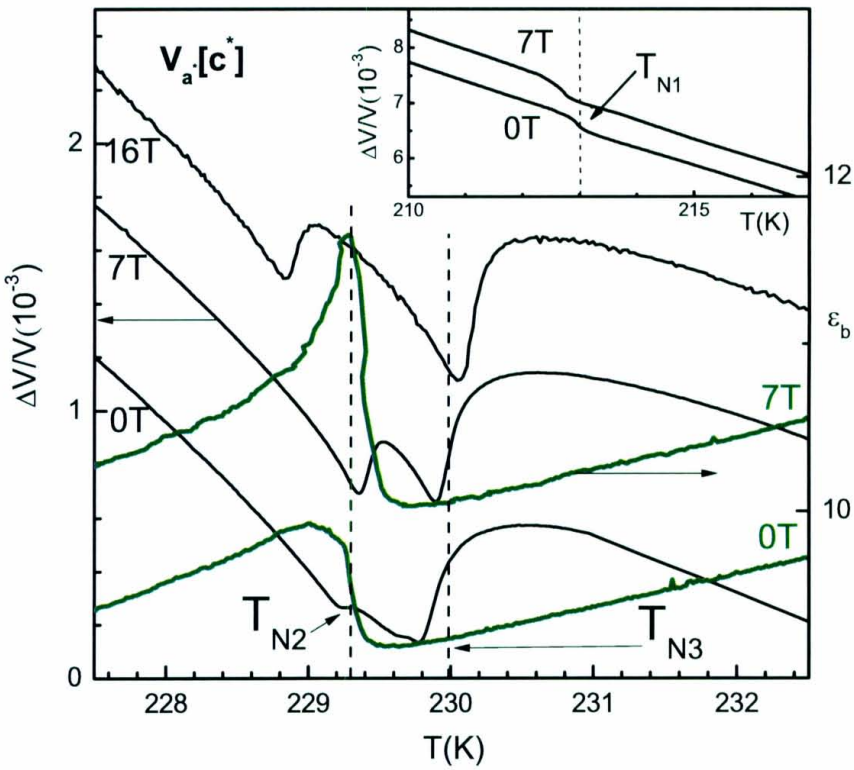

Figure 5.4: $V_{a^*}[c^*]$ acoustic mode temperature and magnetic field dependence ($\mathbf{B}\|\ \mathbf{b}$) for the cooling process. Dielectric constant measurements in green. T_{N1} in the inset.

Dielectric measurements: The above results are supported by supplementary dielectric measurements along the **b** axis, also shown in Fig. 5.4. Notice that, as the stability range of the intermediate phase is small ($\Delta T \sim 0.7$ K, which agrees with the prediction of Ref. [44]), velocity and dielectric data have been collected simultaneously to avoid any ambiguity regarding the actual critical temperatures. As shown in Fig. 5.4, for B = 0 and 7 T, the anomaly observed on the dielectric constant ϵ_b

coincides very well with T_{N2} determined using velocity data, while no variation is noticeable at T_{N3}. These results also indicate that the new phase AF3 is not ferroelectric, while magnetoelectric coupling exists for the AF2 phase. The comparison of our dielectric constant measurements and the recent measurements from another group (in Figure 2.7 [32]) made us distinguish a difference in magnitudes. This could be due to parasitic contributions as mentioned in Ref. [75]: the presence of other insulators in the sample's region may yield competitive effects. Magnetic fields were also applied for the acoustic modes V_{a^*} and $V_{a^*}[b]$ along the $\mathbf{a}^*$ and $\mathbf{b}$ axes up to 7 T but no significant field dependence was observed (therefore, these measurements are not presented). Simultaneous dielectric constant measurements along the $\mathbf{b}$ axis and ultrasonic velocity measurements for the acoustic modes V_a^*, $V_a^*[b]$ and $V_c^*[a^*]$ were carried out as well. These results revealed that their anomalies close to 230 K correspond to T_{N3} and not T_{N2}.

Spin-flop: In Figure 5.5 we present the magnetic field dependence, with $\mathbf{B} \parallel \mathbf{b}$, of the velocity of the acoustic mode $V_{a^*}[c^*]$ obtained at different temperatures. For these measurements, the temperature is kept constant while the magnetic field is increased from 0 to 16 T. A minimum is observed in the relative sound velocity variations for most of the temperatures with the exception of 10 K, 50 K, 202 K and 220 K, where a maximum is observed or the minimum is not very clear. This minimum has an obvious temperature dependence since its magnitude and position (in the field range) change with temperature. As the magnetic moments are known to be parallel to the field in the AF1 commensurate collinear state [32, 40], we attribute the observed anomaly to a spin-flop transition. As pointed out in Ref. [86] for the quasi-one-dimensional antiferromagnet $CsNiCl_3$, these features indicate a spin-flop transition. At 10 K, the spin-flop magnetic field is $B_{SF} = 11$ T and increases slowly up to 13.5 T at T_{N1}. This is in good agreement with magnetic susceptibility measurements performed on

powder samples [46]. This is the first time that the spin-flop transition is measured in a single crystal sample of CuO. Generally, a lower magnetic field is necessary to flip the magnetic moments when they are both parallel. Therefore, stronger magnetic fields are expected to be necessary for this transition to happen when the field and the magnetic moments are perpendicular (e.g. the case of **B** in the ac plane).

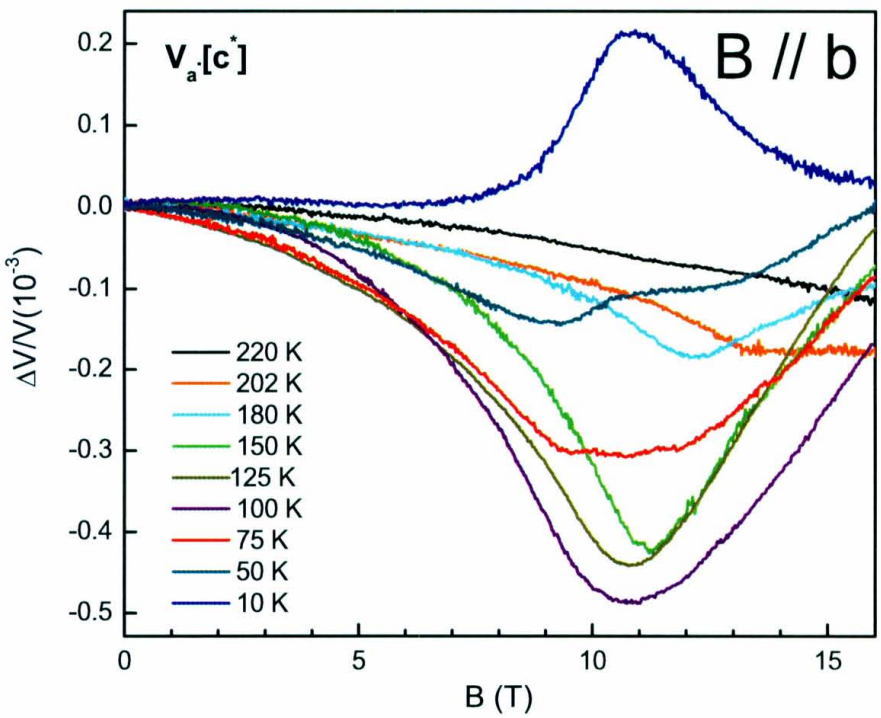

Figure 5.5: Spin-flop transition for $\mathbf{B} \parallel \mathbf{b}$ at different temperatures for the $V_{a^*}[c^*]$ mode.

5.3 Experimental phase diagram

In Fig. 5.6 we present the magnetic phase diagram of CuO determined up to 16 T for $\mathbf{B} \parallel \mathbf{b}$ using ultrasonic velocity measurements with the acoustic mode $V_{a^*}[c^*]$. At B = 0, as the temperature is lowered from the paramagnetic phase, three phase transitions are observed. The new AF3 intermediate phase exists along the magnetic field range attained and the temperature stability range increases from $\Delta T \sim 0.7$ K up to $\Delta T \sim 1.0$ K. The spiral state (AF2) extends up to 16 T, as well, with a small decrease of the temperature stability range at higher magnetic fields. In general, the critical temperatures T_{N1}, T_{N2}, and T_{N3} are weakly field dependent, while B_{SF} increases with temperature. At the tricritical point $B_{TCP} \sim 13.5$ T and $T_{TCP} \sim 212.5$ K, AF1, AF2 and HF1 meet and for higher magnetic fields a crossover from AF2 $\rightarrow$ HF1 is found. This is the first time the magnetic field-temperature phase diagram of CuO is determined.

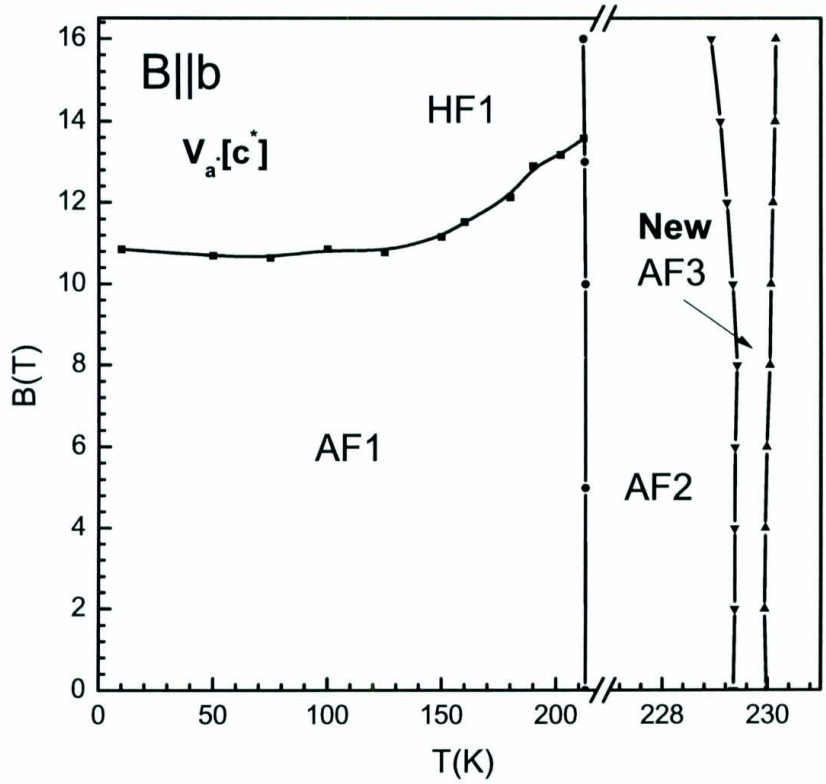

Figure 5.6: Magnetic phase diagram of CuO for the $V_{a^*}[c^*]$ mode with $\mathbf{B} \parallel \mathbf{b}$ (lines are used to guide the eye).

Chapter 6

Landau Theory of Phase Transitions: Application to CuO

The Landau theory of phase transitions is a general mean-field formulation in the context of classical statistical mechanics [88]. Landau theory generalizes the single mean magnetization, otherwise called order parameter, retaining the idea of Gibbs free energy optimization to obtain the equilibrium state. The order parameters characterize different types of long-range ordering that define states of matter such as a ferromagnetic state, a ferroelectric state, etc [89] that are associated with deviations from the disordered equilibrium state [90]. In this framework, the physical macroscopic properties are represented by a free energy functional that is minimized with respect to the order parameters. This yields a phenomenological macroscopic model that describes the phase transitions, that can be first order (discontinuous) or second order (continuous). In this chapter a Landau-type free energy (F_L) is adopted. Hence the thermodynamic potential would be $\Phi(T, S) = \Phi_0(T) + F_L(T, S)$.

6.1 Order parameters and the free energy

The Landau-type free energy is derived from a few principles. The order parameter is assumed to be small near the phase transition allowing for a Taylor series expansion. This is valid close to the paramagnetic state ($S = 0$). In principle, the order parameter depends on temperature, and other external parameters, and it is a known specific physical quantity that differs in the two phases [91]. Thus, it is used to define the degree of order below the transition temperature, or critical temperature (T_c). In continuous phase transitions (of second order), the order parameter continuously decreases to zero as the T_c is approached from below. In discontinuous phase transitions (of first order), the order parameter discontinuously decreases to zero as the T_c is approached from below (see Figure 6.1).

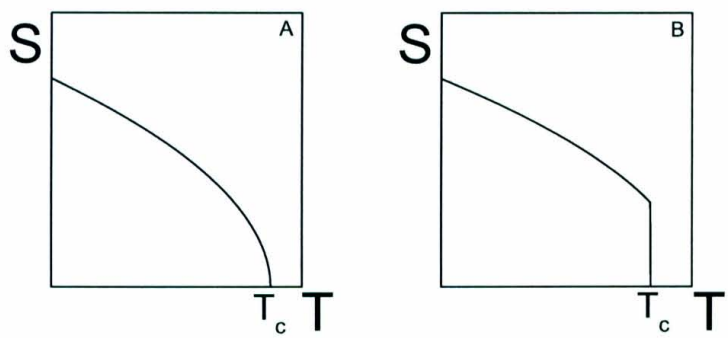

Figure 6.1: A. Second order phase transition. B. First order phase transition.

Thus, every magnetic system can be associated with a mean-field Landau free energy. This free energy must be invariant under the symmetry operations of the high-temperature phase leading to a reduction of the number of terms, as with the tensors e_{ij}, T_{ij}, and C_{ijkl} in Chapter 4. In our case, the spin polarization vector (**S**) is chosen as a magnetic order parameter and thus every term of the free energy must be invariant under inversion and time reversal (**S**→ -**S**, **H**→ -**H**) symmetries

since the high-temperature phase is paramagnetic. This way we can expect at least two states: a disordered state with $S = 0$ and an ordered state where $S \neq 0$. The first order term in the expansion should be zero as it is imposed by the extremum condition $\frac{\partial F_L}{\partial S} = 0$ and in our case all odd power terms are not allowed due to the time inversion symmetry. An expansion of the Landau free energy to the 4^{th}-order of the order parameter S would be of the form

$$F_L(S) = \frac{1}{2}AS^2 + \frac{1}{4}BS^4. \tag{6.1}$$

As a convention, A is used to represent a temperature dependent parameter given by a function such as $A(T) = a(T - T_0)$, with $a > 0$ for reasons that will be given in the next section. The coefficients a, T_0 and B are a priori unknown phenomenological parameters that can be estimated by fitting to experimental data.

6.2 Phase transitions

Second order phase transitions: An equation of state can be derived by minimizing Eq. 6.1 with respect to the order parameter S

$$\frac{\partial F_L}{\partial S}(S) = S(A + BS^2) = 0, \tag{6.2}$$

leading to two solutions: the trivial $S = 0$ and the non-trivial

$$S = \pm\sqrt{-\frac{A}{B}}. \tag{6.3}$$

The trivial solution represents a paramagnetic state since the order parameter is the spin polarization and $S = 0$ is attributed to no long-range magnetic order at all. The stability condition, associated with a minimum in the free energy, is given by

$$\frac{\partial^2 F_L}{\partial S^2} = A \geq 0. \tag{6.4}$$

This indicates that the paramagnetic region is $T \geq T_0$ and if we substitute A with our ansatz $A(T) = a(T - T_0) \rightarrow T_0 = T_c$, where $a > 0$. The non-trivial solution $S \neq 0$ would be stabilized by

$$\frac{\partial^2 F_L}{\partial S^2}(T, S) = A(T) + 3BS^2 \geq 0. \tag{6.5}$$

If we substitute Eq. 6.3,

$$\frac{\partial^2 F_L}{\partial S^2}(T) = -2A(T) = -2a(T - T_c) \geq 0, \tag{6.6}$$

establishing two conditions: $A(T) < 0$ and $B > 0$ in order to have a minimum of F_L that is a stable state, meaning that the $S \neq 0$ region is below $T_0 = T_c$. This also means that our ansatz was a good guess after all. Albeit with this ansatz we are assuming that the function $A(T)$ has no singularity at T_c and can be expanded near the transition.

Notice that in the paramagnetic state only one solution exists $S = 0$ whereas for the non-trivial case there are two minima ($\pm$) for the free energy due to the square-root in Eq. 6.3. This last remark represents the fact that if we had e.g. a ferromagnetic state for the non-trivial case, there would be two possible equivalent solutions: all spins up and all spins down.

First order phase transitions: One way to discuss first order phase transitions in a Landau basis is by adding higher degree terms in the order parameter expansion [91]. For the case of only one component order parameter, the free energy expansion is

$$F_L(S) = \frac{A}{2}S^2 + \frac{B}{4}S^4 + \frac{C}{6}S^6, \tag{6.7}$$

where a first order transition is described when $B < 0$ and $C > 0$ are assumed. By minimizing the free energy we get the following relation

$$\frac{\partial F_L}{\partial S}(S) = S(A + BS^2 + CS^4) = 0, \tag{6.8}$$

where there are three solutions: $S_1^2 = 0$ and

$$S_{2,3}^2 = \frac{-B \pm \sqrt{B^2 - 4AC}}{2C}. \tag{6.9}$$

The first solution represents the paramagnetic state whereas the two other are ordered states below the critical temperature. Since A is temperature dependent, we can consider four different cases.

For $B^2 - 4AC < 0$, A has to be $> \frac{B^2}{4C}$ and substituting the ansatz for A

$$T > T_0 + \frac{B^2}{4aC}. \tag{6.10}$$

If this equation is satisfied there is no solution and the free energy can only be minimized by $S = 0$.

For $B^2 - 4AC = 0$

$$T_2 = T_0 + \frac{B^2}{4aC}, \tag{6.11}$$

and

$$S(T_2) = -\frac{B}{2C}. \tag{6.12}$$

For $T = T_c$, the critical temperature is obtained using the equilibrium condition

$$\frac{\partial^2 F_L}{\partial S^2}|_{S=0} = a(T_c - T_0) = 0, \tag{6.13}$$

so $T_c = T_0$.

Finally, for $T = T_1$, we need to solve Eq. 6.8 and we need Eq. 6.7 to be equal to 0.

$$T_1 = T_c + \frac{3B^2}{16aC}. \tag{6.14}$$

This T_1 corresponds to the equal stability of the two phases ($S = 0$ and Eq. 6.9), or where the two free energies are equal ($F_1 = F_2$). This is the temperature at which the first order phase transition would most probably take place. However, first order phase transitions are characterized by a coexistence region, delimited by T_c and T_2, with two metastable phases. This is generally called a thermal hysteresis, where the transition temperature will not be the same on the heating and cooling processes.

6.3 Anisotropy

An important subject concerning magnetic phenomena is anisotropy. In a few words, magnetic anisotropy refers to the dependence of the magnetic properties relative to the direction [92]. In magnetocrystalline anisotropy the magnetization tends to align along a preferred crystallographic direction, the easy direction. The energy required to rotate the spin system away from the easy axis is proportional to the energy that is necessary to overcome the spin-orbit coupling. The orbitals are in general overlapping and coupled to the lattice. As a result, the magnetocrystalline anisotropy has always the same symmetry as the crystal structure. For example, in order to find the invariant terms of the free energy of a monoclinic compound that belongs to the C2/c space group, the symmetry generators which are the inversion and a C_2^y rotation can be used. Assuming a similar Hamiltonian with two interacting spins as in Eq. 4.36 but in the matrix form

$$H = \sum J_{ab}\mathbf{s}_a\mathbf{s}_b, \tag{6.15}$$

where J_{ab} are the exchange coefficients. Since these are the same symmetry operations as for the crystal structure, following the same procedure as for the elastic stiffness tensor in Eq. 4.21 ($J_{ab} = \alpha_a^m \alpha_b^n J_{mn}$) leads to

$$J = \begin{pmatrix} J_{xx} & 0 & J_{xz} \\ 0 & J_{yy} & 0 \\ J_{xz} & 0 & J_{zz} \end{pmatrix}. \tag{6.16}$$

Then the invariant Hamiltonian is represented by the terms

$$H = J_{xx}s_x^2 + J_{yy}s_y^2 + J_{zz}s_z^2 + 2J_{xz}s_x s_z, \tag{6.17}$$

this can be rearranged as

$$H = J_{xx}(s_x^2 + s_y^2 + s_z^2) + (J_{yy} - J_{xx})s_y^2 + (J_{zz} - J_{xx})s_z^2 + 2J_{xz}s_x s_z, \tag{6.18}$$

where the first term represents the isotropic exchange contribution and the other three anisotropic exchange terms. A brief demonstration on how to do this operation is shown in the Appendix A.

6.4 Landau Model for CuO (and Monoclinic Multiferroics)

A Landau model is here presented based on the principles of the previous sections and general characteristics of low symmetry monoclinic compounds. The special case of CuO is developed with the purpose of explaining the experimental results from Chapter 5 and with the intention of learning more about the two new magnetic phases (AF3 and HF1). However, semi-qualitative agreement with other compounds is expected due to the Landau-type formalism which is based on symmetry arguments and thus should be applicable to systems similar to CuO. First, the Landau free energy together with the order parameters is given. At last, the results of its analysis (minimization) are shown and discussed. This model is inspired by work on geometrically frustrated magnets defined by the Hamiltonian and the lattice structure [93].

6.4.1 Landau free energy and order parameters for CuO

The basics of the mathematical formulation and assumptions for the free energy are described in the following subsections. Starting from the Hamiltonian, continuing with the Landau free energy and ending with a brief explanation of how the order parameters are found using the analytical expressions for the temperature and magnetic field dependence. As first order phase transitions are anticipated, analytical and numerical calculations were necessary.

6.4.1.1 Invariant terms and Hamiltonian

The starting point is the Heisenberg model Hamiltonian (the most general type of symmetric quadratic interaction)

$$H = \sum_{ab} J_{ab} \mathbf{s}_a \mathbf{s}_b, \tag{6.19}$$

where $a, b = x, y, z$ and the Hamiltonian should be invariant with respect to the generators of the symmetry group. If we use the symmetry arguments for the monoclinic space group C2/c, mainly involving a 180° rotation along the **y** axis, as shown in the previous section the matrix (J_{ab}) is reduced and leads to

$$H = \frac{1}{2} \sum_{i \neq j} J_{ij} \mathbf{s}_i \cdot \mathbf{s}_j + D_y \sum_i (s_i^y)^2 + D_z \sum_i (s_i^z)^2 + D_{xz} \sum_i (s_i^x s_i^z) - \mathbf{H} \cdot \sum_i \mathbf{s}_i, \tag{6.20}$$

where J_{ij} represents the isotropic exchange interaction, **H** is an applied magnetic field, $\{D_y, D_z, D_{xz}\}$ are single-ion anisotropic terms allowed by symmetry which are responsible for the magnetoelectric effect, revise Section 1.2. For $\mathrm{J}_{ij} > 0$ the coupling is antiferromagnetic while for the anisotropic term, $D > 0$, the energy is minimized by a planar configuration and when $D < 0$ the energy is minimized by an axial configuration of the spins.

6.4.1.2 Landau free energy

Total free energy: Assuming that the physical properties of a phase can be described by a magnetic order, the integral form of the Landau-type expansion of the free energy functional up to fourth order in terms of the spin density $\mathbf{s}(\mathbf{r})$ is given by [94, 47, 83, 95]

$$
\begin{aligned}
F_L &= F_2 + F_4 - F_A - F_Z, && (6.21)\\
F_2 &= \frac{1}{2V^2}\int d\mathbf{r}_1 d\mathbf{r}_2\ A(\mathbf{r}_1,\mathbf{r}_2)\ \mathbf{s}(\mathbf{r}_1)\cdot\mathbf{s}(\mathbf{r}_2), && (6.22)\\
F_4 &= \frac{1}{4V^4}\int d\mathbf{r}_1 d\mathbf{r}_2 d\mathbf{r}_3 d\mathbf{r}_4\ B(\mathbf{r}_1,\mathbf{r}_2,\mathbf{r}_3,\mathbf{r}_4)\ \mathbf{s}(\mathbf{r}_1)\cdot\mathbf{s}(\mathbf{r}_2)\ \mathbf{s}(\mathbf{r}_3)\cdot\mathbf{s}(\mathbf{r}_4), && (6.23)\\
F_A &= \frac{1}{2V}\int \left[D_y(\mathbf{r})s_y(\mathbf{r})s_y(\mathbf{r}) + D_z(\mathbf{r})s_z(\mathbf{r})s_z(\mathbf{r}) + D_{xz}(\mathbf{r})s_x(\mathbf{r})s_z(\mathbf{r})\right] d\mathbf{r}, && (6.24)\\
F_Z &= \frac{1}{V}\int \mathbf{s}(\mathbf{r})\cdot\mathbf{H}\ d\mathbf{r}. && (6.25)
\end{aligned}
$$

The local spin density, $\mathbf{s}(\mathbf{r})$, is defined in terms of a non-local spin density $\rho(\mathbf{r})$ that describes the long-range magnetic order of the ions

$$
\begin{aligned}
\mathbf{s}(\mathbf{r}) &= \frac{V}{N}\sum_{\mathbf{R}} \rho(\mathbf{r})\delta(\mathbf{r}-\mathbf{R}), && (6.26)\\
\rho(\mathbf{r}) &= \mathbf{m} + \mathbf{S}e^{i\mathbf{Q}\cdot\mathbf{r}} + \mathbf{S}^* e^{-i\mathbf{Q}\cdot\mathbf{r}}, && (6.27)
\end{aligned}
$$

where the monoclinic structure of CuO is given by a unit cell of four Cu^{2+} magnetic ions (see Figure 6.2).

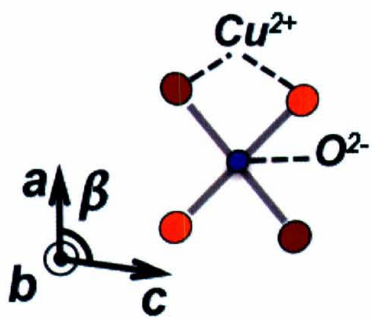

Figure 6.2: Unit cell. Orange means the ions have a different coordination on the **b** axis.

The positions of the ions are defined by four basis vectors $\mathbf{w}_1 = 0$, $\mathbf{w}_2 = \frac{1}{2}\mathbf{a} + \frac{1}{2}\mathbf{b}$, $\mathbf{w}_3 = \frac{1}{2}\mathbf{b}+\frac{1}{2}\mathbf{c}$, $\mathbf{w}_4 = \frac{1}{2}\mathbf{a}+\frac{1}{2}\mathbf{c}$ (where $\mathbf{R} = \mathbf{R}_l+\mathbf{w}_i$ and $\mathbf{R}_l = u\mathbf{a}+v\mathbf{b}+w\mathbf{c}$). V is the volume of the crystal, N represents the number of Cu^{2+} magnetic ions, $\mathbf{S}$ is the spin polarization vector. Moreover, the long-range magnetic order is described by a single wave vector $\mathbf{Q}$ while $\mathbf{m}$ is the induced uniform magnetization due to the magnetic field. The coefficient from Eq. 6.22 is given by $A(\mathbf{r}) = ak_BT\delta(\mathbf{r})+j^2J(\mathbf{r})$ providing the temperature dependence and $J(\mathbf{r})$ are the exchange interactions [83]. The coefficient from Eq. 6.23, $B(\mathbf{r})$, is assumed to be only spatially dependent and independent of temperature. Furthermore, to account for non-collinear spin configurations, we write the complex spin polarization in terms of real and imaginary parts as $\mathbf{S} = \mathbf{S}_1 + i\ \mathbf{S}_2$. These vectors are parametrized by the angles β, γ, and θ through (also see Ref. [94])

$$\mathbf{S}_1 = S\cos\beta[\cos\gamma\ \hat{\mathbf{y}} + \sin\gamma\ \hat{\rho}_\mathbf{2}], \tag{6.28}$$

$$\mathbf{S}_2 = S\sin\beta[\cos\theta\ \hat{\rho}_\mathbf{1} + \sin\theta(\cos\gamma\ \hat{\mathbf{y}} + \sin\gamma\ \hat{\rho}_\mathbf{2})], \tag{6.29}$$

where $\hat{\rho}_1$ and $\hat{\rho}_2$ are two orthogonal unit vectors normal to the easy axis, $\hat{\mathbf{y}} \parallel \mathbf{b}$. The direction of the moments in the ac plane is accounted for by defining the unit vectors $\hat{\rho}_1$ and $\hat{\rho}_2$ relative to Cartesian vectors, $\hat{\rho}_1 = \cos\alpha\ \hat{\mathbf{x}} + \sin\alpha\ \hat{\mathbf{z}}$ ($\hat{\mathbf{a}} \parallel \hat{\mathbf{x}}$) and $\hat{\rho}_2 = -\sin\alpha\ \hat{\mathbf{x}}+\cos\alpha\ \hat{\mathbf{z}}$, where α sets the direction of the magnetic moments on the ac plane. It is assumed that Eqs. 6.28 and 6.29 provide sufficient flexibility to describe the magnetic ordering in CuO. Note that β is an order parameter, not to be confused with the angle β of the monoclinic structure from Figure 6.2.

2nd-order contribution (F_2): Within the present model, the value of $\mathbf{Q}$ can be determined by simply considering the quadratic exchange contributions [47]

$$F_2 = \frac{1}{2V^2}\int d\mathbf{r}_1 d\mathbf{r}_2 \; A(\mathbf{r}_1 - \mathbf{r}_2)\; \mathbf{s}(\mathbf{r}_1)\cdot\mathbf{s}(\mathbf{r}_2), \tag{6.30}$$

which leads to $F_2 = \frac{1}{2}\tilde{A}_0 m^2 + A_Q S^2$ where $S^2 = \mathbf{S}\cdot\mathbf{S}^*$ and $A_Q = aT + J_Q$, with J_Q being the Fourier transform of the exchange integral $J(\mathbf{R})$,

$$J_Q = \sum_R J(\mathbf{R}) e^{i\mathbf{Q}\cdot\mathbf{R}}. \tag{6.31}$$

Considering the C-type monoclinic cell with four Cu^{2+} magnetic ions, we obtain

$$\begin{aligned}
J(\mathbf{Q}) &= 2\left[J_1 f_1(\mathbf{Q}) + J_2 f_2(\mathbf{Q}) + J_3 f_3(\mathbf{Q}) + J_4 f_4(\mathbf{Q})\right] \\
f_1(\mathbf{Q}) &= \cos(\pi q_a - \pi q_c) \\
f_2(\mathbf{Q}) &= \cos(\pi q_a + \pi q_c) \\
f_3(\mathbf{Q}) &= \cos(\pi q_a - \pi q_b) + \cos(\pi q_a + \pi q_b) \\
f_4(\mathbf{Q}) &= \cos(\pi q_b - \pi q_c) + \cos(\pi q_b + \pi q_c),
\end{aligned} \tag{6.32}$$

where J_1 and J_2 represent the nearest-neighbours exchange interactions along the AFM-chain and the coupling between chains on the same plane normal to **b**, respectively, while J_3 and J_4 represent the nearest-neighbours exchange interactions along **a** and **c** between Cu^{2+} ions on different planes (see Fig. 6.3).

The value of **Q** is then obtained by finding the extrema of J_Q (Eq. 6.32) as a function of the exchange interactions. Results of our numerical Fortran algorithm are summarized in the $J_2 - J_3$ phase diagram shown in Fig. 6.4 for AFM chains (with $J_1 \equiv 1$). This algorithm is based on a minimization technique called downhill simplex method and an example is given in the Appendix B. For different J_4 values, we

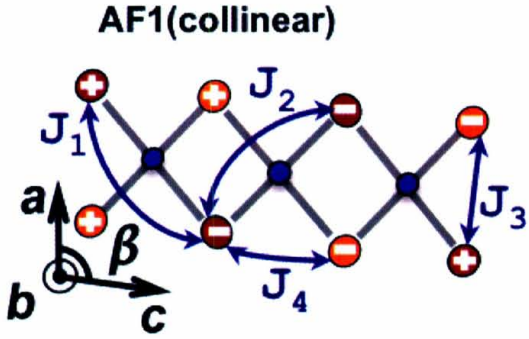

Figure 6.3: Exchange interactions.

obtain three phases: an incommensurate phase with $\mathbf{Q}_{ICM} = [q_a, 0, q_c]$ (left side) and two commensurate phases (top and bottom right side). Depending on the sign of J_3 relative to J_4, the commensurate wave vector is either $\mathbf{Q}_{CM} = [100]$ or $\mathbf{Q}_{CM} = [001]$. More interestingly, with $J_3 = J_4 = 0$ we obtain the expected commensurate wave vector $\mathbf{Q}_{CM} = [\frac{1}{2}\ 0\ -\frac{1}{2}]$ for $J_2 \leq 0$ (dash line in Fig. 6.4). Moreover, an ICM state with a modulation vector comparable to that of the experimental value $\mathbf{Q}_{ICM} = [0.506\ 0\ -0.483]$ is stabilized whenever J_3 and/or J_4 are non-zero but small relative to J_1 (for example, $J_2/J_1 = -0.3$, $J_3/J_1 = 0.017$, and $J_4/J_1 = 0$ leading to $J_Q/J_1 = -2.6$). These relative values are also in good agreement with estimates obtained by density functional theory [41, 57, 58] and are consistent with the quasi-1D magnetic character of CuO. Unfortunately, there is not enough inelastic neutron scattering data in order to specify the real values of these exchange interactions.

4th-order contribution (F_4): Adopting the same approach for the fourth-order term, we obtain

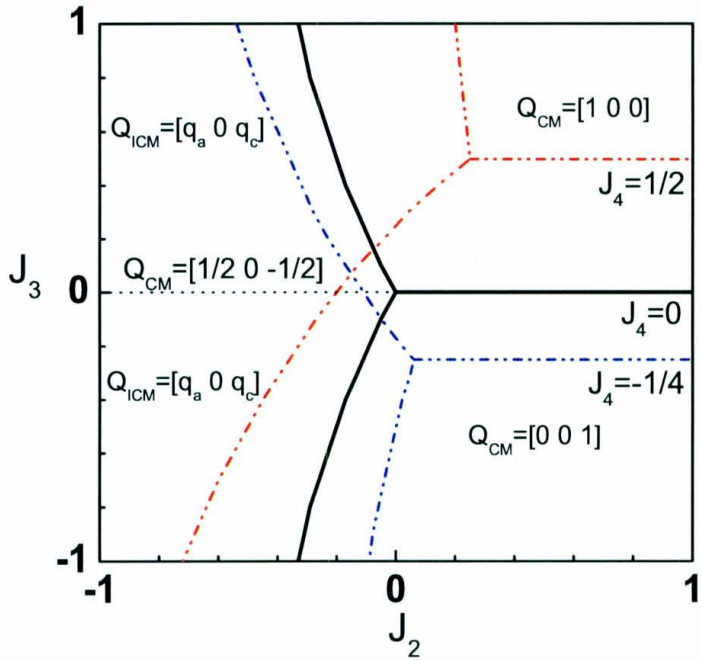

Figure 6.4: $J_3 - J_2$ phase diagram for different values of $J_4 = 0, \frac{1}{2}, -\frac{1}{4}$ with $J_1 = 1$. One incommensurate phase with $\mathbf{Q}_{ICM} = [q_a, 0, q_c]$ (left side) and two commensurate phases ($\mathbf{Q}_{CM} = [100]$ and $\mathbf{Q}_{CM} = [001]$) are obtained.

$$\begin{aligned} F_4 &= B_1 S^4 + \frac{1}{2} B_2 |\mathbf{S} \cdot \mathbf{S}|^2 + \frac{1}{4} B_3 m^4 + 2B_4 |\mathbf{m} \cdot \mathbf{S}|^2 \\ &\quad + B_5 m^2 S^2 + \frac{1}{4} B_U [(\mathbf{S} \cdot \mathbf{S})^2 + c.c.] \Delta_{4\mathbf{Q},\mathbf{G}} \ , \end{aligned} \tag{6.33}$$

where as in Ref. [95]

$$B_1 = B_{\mathbf{Q},-\mathbf{Q},\mathbf{Q},-\mathbf{Q}}, \tag{6.34}$$

$$B_2 = B_{\mathbf{Q},\mathbf{Q},-\mathbf{Q},-\mathbf{Q}}, \tag{6.35}$$

$$B_U = B_{\mathbf{Q},\mathbf{Q},\mathbf{Q},\mathbf{Q}}. \tag{6.36}$$

Note that the umklapp term $\Delta_{4\mathbf{Q},\mathbf{G}}$ arises directly from the lattice periodicity [47]

$$\frac{1}{N}\sum_{\mathbf{R}} e^{in\mathbf{Q}\cdot\mathbf{R}} = \Delta_{n\mathbf{Q},\mathbf{G}}, \tag{6.37}$$

where $\mathbf{G}$ is a monoclinic reciprocal lattice vector. This term is crucial in order to account for the first order phase transition observed at T_{N1} in CuO where a commensurate collinear state is stabilized. As noted in the Ref. [95], the $2\mathbf{Q}$ umklapp term is already included by a suitable renormalization of the spin density amplitude, and for this case terms different from $4\mathbf{Q}$ are omitted. Moreover, the sign of B_2 determines the type of spin polarization that minimizes the free energy. For example, in a collinear system the second term in Eq. 6.33, $\frac{1}{2}B_2|\mathbf{S}\cdot\mathbf{S}|^2 \neq 0$, whereas in a simple helical spin density with $\mathbf{S} = \frac{S}{\sqrt{2}}(\hat{\mathbf{x}} + i\hat{\mathbf{y}})$ the factor $(\mathbf{S}\cdot\mathbf{S}) = 0$. Therefore, non-collinear spin configurations are stabilized when $B_2 > 0$. Similarly, spin-flop transitions in antiferromagnets occur as a consequence of $B_4 > 0$ [95].

Anisotropic contribution (F_A): In addition to the usual second order exchange term, we also include single-ion anisotropic contributions. As demonstrated before, considering the symmetry of monoclinic crystals (C2/c), we identified three invariants which are given by

$$F_A = \frac{1}{2}D_{y0}m^2 + D_{yQ}|S_y|^2 + D_{zQ}|S_z|^2 + D_{xzQ}S_xS_z. \tag{6.38}$$

While D_y can be used to set the magnetic moments along **b**, the other terms are necessary in order to define the direction of the moments in the *ac* plane. The degree of anisotropy has not been experimentally determined yet; however, it is still possible to propose some estimates that give a qualitative agreement with some indirect experimental results.

The free energy with respect to the order parameters (S, β, θ, γ, α, and m) is given by the following expressions.

$$F_2 = \frac{1}{2}\tilde{A}_0 m^2 + A_Q S^2, \tag{6.39}$$

$$\begin{aligned} F_4 = {} & B_1 S^4 + \frac{1}{2} B_2 S^4 (4\sin^4\beta\cos^2\theta - 4\sin^2\beta\cos^2\theta + 1) \\ & + \frac{1}{4} B_3 m^4 - 2B_4 S^2 m^2 \cos^2\gamma(\sin^2\beta\cos^2\theta - 1) + B_5 S^2 m^2 \\ & \frac{1}{2} B_U S^4 (4\sin^4\beta(2 - \cos^2\theta) - 4\sin^2\beta(2 - \cos^2\theta) + 1), \end{aligned} \tag{6.40}$$

$$\begin{aligned} F_A = {} & \frac{1}{2} D_{y0} m^2 + D_{yQ} S^2 \cos^2\gamma(1 - \sin^2\beta\cos^2\theta) \\ & + \frac{1}{2} D_{zQ} S^2 \Big[\sin\gamma(\sin 2\alpha \sin^2\beta \sin 2\theta + 2\cos^2\alpha \sin\gamma) \\ & + \sin^2\beta\cos^2\theta(\sin^2\alpha(3 - \cos 2\gamma) - 2\sin^2\gamma)\Big] \\ & + 2D_{xzQ} S^2 \left[\sin\alpha\cos\alpha\left(\frac{1}{2}\sin^2\beta\cos^2\theta\,(3 - \cos 2\gamma) - \sin^2\gamma\right)\right. \\ & \left. + \frac{1}{2}\cos 2\alpha \sin^2\beta \sin\gamma \sin 2\theta\right]. \end{aligned} \tag{6.41}$$

6.4.2 Theoretical phase diagram

Minimization: The total free energy, $F_L = F_2 + F_4 - F_A - F_Z$, with $A_Q = a(T - T_Q)$ and $\tilde{A}_0 + D_{y0} = a(T + T_0)$, is then numerically minimized for the order parameters (S, β, θ, γ, α, and m) in order to find the theoretical phase diagram and the spin configurations of the respective states (see Appendices A and B). As in Ref. [94], most coefficients are set using analytical solutions associated with phase boundaries of

second order transitions. This is done by assuming an ansatz of order parameters that give the right spin configuration for the known magnetic states and then analytically calculating the solutions to the phase boundaries by finding the derivatives of the respective free energies. Since we are interested only in qualitative features of the phase diagram, arbitrary units are used for the parameters. For example, when the only anisotropic contribution taken into account is D_y, the phase boundaries for the phase transitions temperatures (T_{N2} and T_{N3}), the tricritical point where AF2 and AF3 meet (T_M and H_M), and the critical field for the crossover to the paramagnetic state (H_C) are

$$T_{N3} = T_Q - \frac{D_{yQ}}{a}, \tag{6.42}$$

$$T_{N2} = T_Q - \frac{D_{yQ}}{a} + \frac{B_1 D_{yQ}}{a B_2}, \tag{6.43}$$

$$T_M = T_Q + \frac{D_{yQ} B_5}{2 a B_4}, \tag{6.44}$$

$$H_M^2 = \frac{D_{yQ}(D_{yQ}(B_3 - B_5) + 2aB_4(T_Q - T_0))^2}{8B_4^3}, \tag{6.45}$$

$$H_C^2 = \frac{a^3(T_Q - T)(B_3(T_Q - T) - B_5(T_0 - T))^2}{B_5^3}. \tag{6.46}$$

Therefore, $a = 1$, $T_Q = 1.18$, $D_{yQ} = -0.02$, $B_1 = 0.103$, and $B_2 = 0.011$ result by assigning reasonable values for the critical temperatures at zero field ($T_{N3} = 1.2$ and $T_{N2} = 1.12$). From the minimization of the free energy with respect to α, we obtain

$$\frac{\partial F_L}{\partial \alpha} = D_{xzQ}(\cos\alpha^2 - \sin\alpha^2) - D_{zQ}\sin\alpha\cos\alpha = 0, \tag{6.47}$$

$$D_{xzQ} = \left(\frac{\sin^2\alpha\cos\alpha}{\cos^2\alpha - \sin^2\alpha}\right) D_{zQ}. \tag{6.48}$$

This result indicates that the direction of the magnetic moments in the ac plane is proportional to the anisotropy ratio D_{xzQ}/D_{zQ}. We must have $D_{zQ} < D_{yQ}$, since D_{yQ} corresponds to the easy magnetic axis, and we set $D_{zQ} = -0.01$ while the direction of the spins in the ac plane ($\alpha_{exp} \sim 70°$) [51] is used to determine the ratio $D_{xzQ}/D_{zQ} = 0.42$ (Eq. 6.48). The last coefficients are determined using the temperature of the multicritical point (where T_{N2} and T_{N3} boundaries meet - T_M and H_M) and the maximum field H_C(T = 0 K) (Eq. 6.46). From this exercise, we find $B_3 = 0.063$ and $B_4 = 0.013$, while $B_5 = 0.1$ was set arbitrarily. Finally, $B_{l'} = 0.035$ is used to obtain $T_{N1} = 0.77$, so that the transition occurs at about 20 % from T_{N2} as it has been observed experimentally. Fig. 6.5 shows the magnetic phase diagram resulting from the minimization of the free energy. For comparison, we also present results obtained without the anisotropic terms D_{zQ} and D_{xzQ} (dotted lines).

Depending on the scenario considered, we can get 5 or 6 magnetic phases illustrated in Fig. 6.6, described by the order parameters listed in Table 6.1. At zero-field, both models (with and without D_z and D_{xz}) predict the same phase sequence, consistent with our experimental observations shown in Fig. 5.6. At low temperatures, a collinear phase AF1 with the moments along **b** is predicted (see Fig. 6.6) while the AF2 phase corresponds to a spiral configuration in agreement with neutron scattering data [40]. According to our numerical calculations, the new intermediate phase AF3 is associated with a collinear phase where only half of the moments order with $\mathbf{S} \parallel \mathbf{b}$. As the field is applied, two spin-flop transitions (AF1$\rightarrow$ HF1 and AF2 $\rightarrow$ HF2) are found. The comparison of both phase diagrams indicates that the role of the anisotropic terms D_{zQ} and D_{xzQ} is to reduce the critical field of the AF1$\rightarrow$ HF1 transition, decrease the stability range of the intermediate phase AF3, and lead to a new magnetic order HF3 in which half the moments align into the ac plane. Depending on the values of D_{zQ} and D_{xzQ}, these findings could account for the fact that no spin-flop phase transition

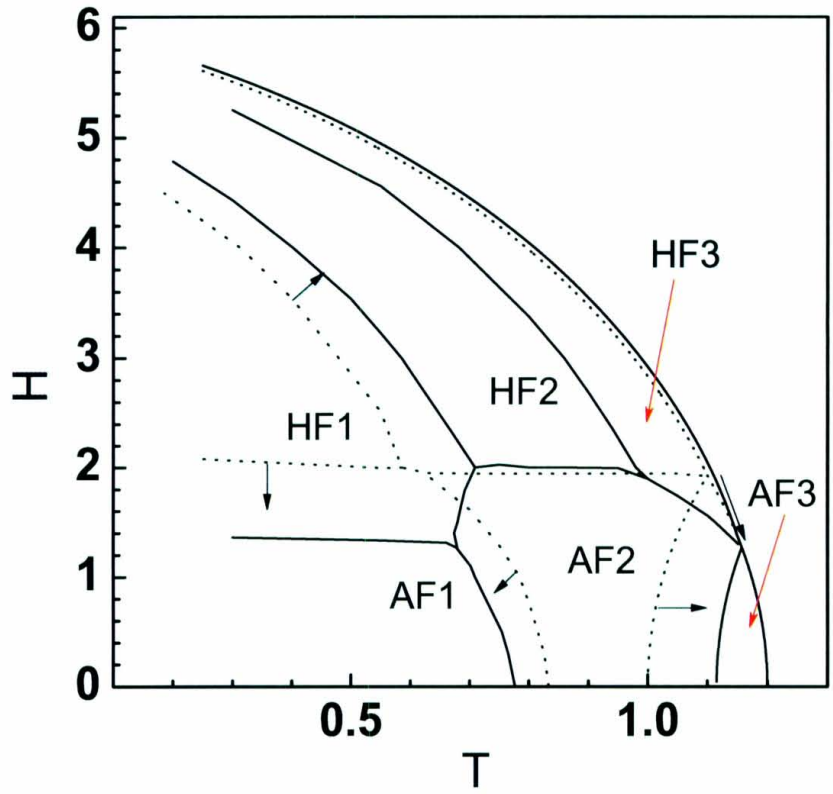

Figure 6.5: Magnetic field - temperature phase diagram of CuO for $\mathbf{H} \parallel \mathbf{b}$ derived from the Landau free energy. Dotted lines represent prediction with only one anisotropic term included, D_{yQ}. The solid line is for the case where all anisotropic terms are considered.

has been observed experimentally up to 16 T for the spiral phase AF2, while the spin-flop transition is observed at $\sim$ 13 T in the commensurate collinear phase AF1.

In a recent publication [96], the magnetic phase diagram of a doped version of $MnWO_4$ (Mn_{1-x}(Fe,Zn,Mg)$_x WO_4$) is well described using Landau theory. In this study, the free energy is based on a Heisenberg Hamiltonian with single-ion anisotropy and in a symmetry basis, just as we did for CuO, and as was done previously for $CuFeO_2$ [47].

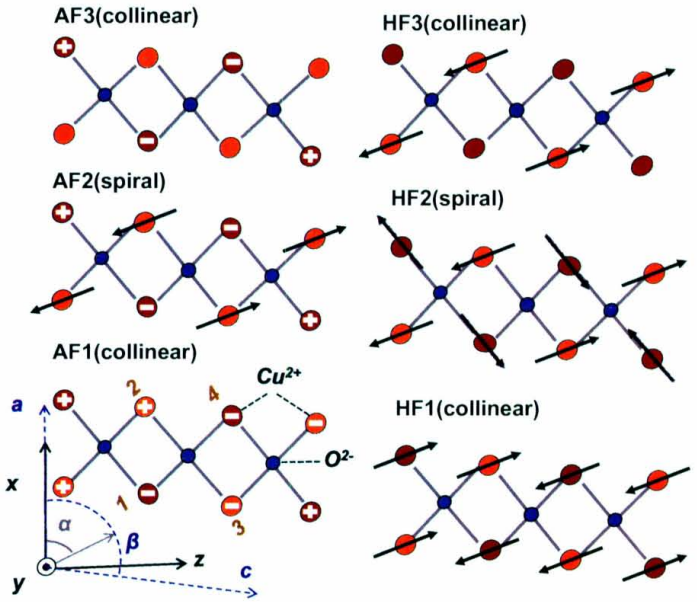

Figure 6.6: Spin configurations in a magnetic cell of 8 ions (red and orange circles). Red circles represent magnetic ions at b = 1/2. The +/- symbols represent spins in/out of the page. When no direction is specified (as in AF3 and HF3), spins on these sites are not ordered.

Antisymmetric DM-interaction: The present model is based on purely isotropic and anisotropic magnetic interactions allowed by symmetry. However, the spontaneous electric polarization can be calculated assuming that it is a result of the antisymmetric DM-interaction. Such approach indicates that the proposed transition to HF2 would involve a ferroelectric order, induced by the magnetoelectric coupling, along some direction in the *ac* plane. This electric polarization flop would reduce the symmetry by a possible structural transition to a triclinic phase when losing the 2-fold rotation. The general form for the induced polarization by antisymmetric DM-interaction is given by

$$\mathbf{P} = \sum_i \sum_j \alpha(\mathbf{r}_j - \mathbf{r}_i)\ \mathbf{r}_{ij} \times [\mathbf{S}(\mathbf{r}_i) \times \mathbf{S}(\mathbf{r}_j)]. \tag{6.49}$$

Table 6.1: Order parameters.

state	β	θ	γ	α
AF1	$\pi/4$	$\pi/2$	0	-
AF2	β	0	0	70°
AF3	-	-	0	-
HF1	$\pi/4$	$\pi/2$	$\pi/2$	160°
HF2	β	0	$\pi/2$	70°
HF3	$\pi/2$	0	-	70°

Using our local spin density Eq. 6.26, the induced polarization can be expressed as

$$\mathbf{P} = \frac{1}{2N}\sum_{\tau}\alpha(\tau)\ (e^{-i\mathbf{Q}\cdot\tau} - e^{i\mathbf{Q}\cdot\tau})\tau \times (\mathbf{S}\times\mathbf{S}^*), \tag{6.50}$$

where $\tau = \mathbf{R}_2 - \mathbf{R}_1$, the distance between NN. This is then simplified to

$$\mathbf{P} = \frac{1}{N}\sum_{\tau} -2\alpha\ \tau \times (\mathbf{S}_1 \times \mathbf{S}_2)\sin(\mathbf{Q}\cdot\tau). \tag{6.51}$$

This sum can be solved for the 6 theoretically predicted states to show that no induced polarization is expected for states other than AF2 and HF2, which give the following relations in cartesian coordinates

$$P_{AF2} = 2S^2\cos\beta\sin\beta(\sin\alpha - \cos\alpha) \ \parallel\ [010], \tag{6.52}$$

$$P_{HF2} = -2S^2\cos\beta\sin\beta \ \parallel\ [101]. \tag{6.53}$$

Thus, an induced polarization flop is expected in the crossover AF2 $\rightarrow$ HF2 from the **b** axis to some direction in the ac plane. Note that this order parameter (α) depends on the ratio between the anisotropic terms as given in Eq. 6.48. This might imply that the magnetoelectric coupling, if it is mediated by the antisymmetric DM-interaction, is due to the magnetic anisotropy. The above argument can be tested with

$\alpha = 45°$, which results in a screw structure with no spontaneous electric polarization as expected for the DM-interaction basis.

Chapter 7

Conclusions

Our principal and most important conclusion is that a new collinear phase (AF3), which occurs between the paramagnetic and the previously identified spiral phase (in agreement with recent predictions [44]), has been detected by high-resolution ultrasonic velocity measurements, then confirmed and explained by a Landau-type free energy model based on a Heisenberg-type Hamiltonian and rigorous symmetry arguments. In contrast with previous MC simulations of Refs. [41, 43], which omit anisotropic contributions, we find that the spin-lattice coupling is not required to account for the observed magnetic ordering.

Moreover, the magnetic-field vs temperature phase diagram for $\mathbf{B} \parallel \mathbf{b}$ has also been determined, revealing the existence of a spin-flop phase (HF1). Complementary dielectric measurements also confirm that magnetoelectric effects only exist in the non-collinear phase.

Evidently, the single-ion anisotropy plays an important role in the stabilization of the intermediate phase (AF3), where the three contributions provided arise from symmetry arguments. The low symmetry allows for such a behaviour and further experiments of the magnetic susceptibility and neutron scattering could clarify the

magnitudes of these coefficients.

The newly identified HF2 phase shows a spiral behaviour as AF2 and according to the Dzyaloshinskii-Moriya interaction an electric polarization flop from the **b** axis to the *ac* plane would be expected as in $TbMnO_3$ [15]. However, in this case the electric polarization would be in the *ac* plane, leading to a reduction in the crystal symmetry.

The new phase (AF3) is what has been predicted in Ref. [44, 40, 45], implying that the mechanism behind the multiferroicity does not require a strong coupling but a weak pseudoproper coupling between the order parameters as it was argued in Ref. [42, 97]. This supports the idea of ferroelectricity in magnetoelectric multiferroics from purely symmetrical interactions [98].

Our findings imply that the multiferroic mechanism in CuO is similar to a traditional cycloidal spin-driven type, such as in $MnWO_4$. The three zero-field magnetically ordered states are stabilized by spin-only contributions which include frustrated exchange interactions [98], spin-orbit induced anisotropy, and an Umklapp-type mechanism giving rise to the lower temperature commensurate phase. Furthermore, the occurrence of such a collinear state, just above a non-collinear state, is confirmed in well studied frustrated orthorhombic systems $RMnO_3$ [99, 100], the kagomé compound $Ni_3V_2O_8$ [36] and $LiCuVO_4$ [34]. Finally, the proposed model accounts for the experimental phase diagram of CuO determined in this work and is potentially useful for the description of other monoclinic multiferroic systems, in particular $MnWO_4$ [101] and $AMSi_2O_6$ [37]. In Table 7.1, details on some of the important characteristics of similar spin-driven multiferroics are presented. These compounds have different magnetic easy axis which is an intrinsic property of the materials. They all have an AF2 cycloidal spiral magnetoelectric state with the exception of $AMSi_2O_6$ that to our knowledge its magnetic order has not been resolved. As well, electric polarization flops have been experimentally demonstrated for all of them with the exception of

CuO and $Ni_3V_2O_8$. Moreover, $MnWO_4$ and CuO share the same sequence of zero-field states with characteristics such as the types of transitions, magnetic ordering, ICM AF2 and AF3 states and 1D-chain behaviour.

Therefore, CuO is a type-II multiferroic via the standard cycloid scenario as the rest of the type-II multiferroics. The good news is that the high-T_N type-II multiferroics key ingredient is the strong exchange interaction. Hence, the strength of the magnetic coupling is not just responsible for high-T_C in the superconducting layered cuprates [55] but also for high-T_N multiferroicity in spin-driven cycloidal multiferroics. The next question is how do we make high-T_N type-II multiferroics with high electric polarization. Future work:

- Resolve the new intermediate state AF3 to confirm its magnetic ordering.
- Experimentally verify the electric polarization flop, phase transitions and magnetic structures theoretically predicted at high magnetic fields.
- Do similar studies to the rest of the compounds in Table 7.1 in order to develop a generalized Landau model for the type-II multiferroics with cycloidal spiral spin-driven ferroelectric order.

Table 7.1: Similar spin-driven multiferroics.

Compound	structure	easy axis	AF2	$\mathbf{P}$	$\mathbf{P}$ flop	AF3	T_{N2}	T_{N1}	AF1	$\mathbf{Q}_{AF2,AF3}$	1D-chain
CuO [51, 55]	monoclinic	**b** axis	*abc* cycloidal	$\mathbf{P}_b$	$\mathbf{H}_b \rightarrow \mathbf{P}_{ac}$?	coll.?	2nd	1st	coll.	ICM	$[10\bar{1}]$
$MnWO_4$ [33]	monoclinic	*ac* plane	*abc* cycloidal	$\mathbf{P}_b$	$\mathbf{H}_b \rightarrow \mathbf{P}_a$	coll.	2nd	1st	coll.	ICM	**c** axis
$AMSi_2O_6$ [37]	monoclinic	*ac* plane	?	$\mathbf{P}_b$	$\mathbf{H}_{ac} \rightarrow \mathbf{P}_c$	coll.	2nd	-	-	?	**c** axis?
$RMnO_3$ [100, 19]	orthorhombic	**b** axis	*bc* cycloidal	$\mathbf{P}_c$	$\mathbf{H}_b \rightarrow \mathbf{P}_a$	coll.	2nd	-	-	ICM	-
$LiCuVO_4$ [34]	orthorhombic	?	*ab* cycloidal	$\mathbf{P}_a$	$\mathbf{H}_a \rightarrow \mathbf{P}_c$	coll.?	?	-	-	ICM	**b** axis
$Ni_3V_2O_8$ [36]	kagomé	**a** axis	*ab* cycloidal	$\mathbf{P}_b$	?	coll.	2nd	1st	2CAF	ICM	-

Bibliography

[1] R. W. Millar, Journal of the American Chemical Society **51**, 215 (1929), http://pubs.acs.org/doi/pdf/10.1021/ja01376a026.

[2] J. G. Bednorz and A. Müller, Zeitscrift für Physik B Condensed Matter **64**, 189 (1986).

[3] Curie, P., J. Phys. Theor. Appl. **3**, 393 (1894), URL http://dx.doi.org/10.1051/jphystap:018940030039300.

[4] M. Fiebig, Journal of Physics D: Applied Physics **38**, R123 (2005).

[5] L. Landau and E. Lifshitz, *Electrodynamics of Continuous Media*, Teoreticheskai fizika (Pergamon Press, 1960).

[6] I. Dzyaloshinskii, Sov. Phys. JETP **37**, 881 (1960).

[7] A. D.N., Sov. Phys. JETP **38**, 984 (1960).

[8] D. Astrov, Sov. Phys. JETP **13**, 729 (1961).

[9] V. Folen, G. Rado, and E. Stalder, Phys. Rev. Lett. **6**, 607 (1961).

[10] G. Rado and V. Folen, Phys. Rev. Lett. **7**, 310 (1961).

[11] G. A. Smolenskiĭ and I. E. Chupis, Soviet Physics Uspekhi **25**, 475 (1982).

[12] H. Schmid, Ferroelectrics **162**, 317 (1994).

[13] Weiss, Pierre, J. Phys. Theor. Appl. **6**, 661 (1907).

[14] H. Schmid, Journal of Physics: Condensed Matter **20**, 434201 (2008).

[15] T. Kimura, T. Goto, H. Shintani, K. Ishizaka, T. Arima, and Y. Tokura, Nature **426**, 55 (2003).

[16] K. Wang, J.-M. Liu, and Z. Ren, Advances in Physics **58**, 321 (2009).

[17] D. Khomskii, Physics **2**, 20 (2009).

[18] T. Kimura, Annual Review of Materials Research (2007).

[19] M. Kenzelmann, A. B. Harris, S. Jonas, C. Broholm, J. Schefer, S. B. Kim, C. L. Zhang, S.-W. Cheong, O. P. Vajk, and J. W. Lynn, Phys. Rev. Lett. **95**, 087206 (2005).

[20] S.-W. Cheong and M. Mostovoy, Nat Mater **6**, 1476 (2007).

[21] H. Katsura, N. Nagaosa, and A. V. Balatsky, Phys. Rev. Lett. **95**, 057205 (2005).

[22] J. Villain, Journal of Physics and Chemistry of Solids **11**, 303 (1959).

[23] T. A. Kaplan, Phys. Rev. **116**, 888 (1959).

[24] A. Yoshimori, Journal of the Physical Society of Japan **14**, 807 (1959).

[25] I. A. Sergienko and E. Dagotto, Phys. Rev. B **73**, 094434 (2006).

[26] M. Mostovoy, Nat. Mater. **7**, 269 (2008).

[27] P. Anderson, Materials Research Bulletin **8**, 153 (1973).

[28] C. LaCroix, P. Mendels, and F. Mila, *Introduction to Frustrated Magnetism: Materials, Experiments, Theory*, Springer Series in Solid-State Sciences (Springer, 2011).

[29] A. P. Ramirez, Annual Review of Materials Science **24**, 453 (1994).

[30] J. M. D. Coey, *Magnetism and Magnetic Materials* (2010).

[31] R. F. Bishop, P. H. Y. Li, D. J. J. Farnell, J. Richter, and C. E. Campbell, Phys. Rev. B **85**, 205122 (2012).

[32] T. Kimura, Y. Sekio, H. Nakamura, T. Siegrist, and A. P. Ramirez, Nat. Mater. **7**, 291 (2008).

[33] K. Taniguchi, N. Abe, T. Takenobu, Y. Iwasa, and T. Arima, Phys. Rev. Lett. **97**, 097203 (2006).

[34] F. Schrettle, S. Krohns, P. Lunkenheimer, J. Hemberger, N. Büttgen, H.-A. Krug von Nidda, A. V. Prokofiev, and A. Loidl, Phys. Rev. B **77**, 144101 (2008).

[35] S. Park, Y. Choi, C. Zhang, and S. Cheong, Physical review letters **98**, 57601 (2007).

[36] G. Lawes, A. B. Harris, T. Kimura, N. Rogado, R. J. Cava, A. Aharony, O. Entin-Wohlman, T. Yildrim, M. Kenzelmann, C. Broholm, et al., Phys. Rev. Lett. **95**, 087205 (2005).

[37] S. Jodlauk, P. Becker, J. A. Mydosh, D. I. Khomskii, T. Lorenz, S. V. Streltsov, D. C. Hezel, and L. Bohatý, Journal of Physics: Condensed Matter **19**, 432201 (2007).

[38] T. Kimura, J. C. Lashley, and A. P. Ramirez, Phys. Rev. B **73**, 220401 (2006).

[39] S. Seki, Y. Onose, and Y. Tokura, Phys. Rev. Lett. **101**, 067204 (2008).

[40] J. B. Forsyth, P. J. Brown, and B. M. Wanklyn, Journal of Physics C: Solid State Physics **21**, 2917 (1988).

[41] G. Giovannetti, S. Kumar, A. Stroppa, J. van den Brink, S. Picozzi, and J. Lorenzana, Phys. Rev. Lett. **106**, 026401 (2011).

[42] P. Tolédano, N. Leo, D. D. Khalyavin, L. C. Chapon, T. Hoffmann, D. Meier, and M. Fiebig, Phys. Rev. Lett. **106**, 257601 (2011).

[43] G. Jin, K. Cao, G.-C. Guo, and L. He, Phys. Rev. Lett. **108**, 187205 (2012).

[44] V. P. Sakhnenko and N. V. Ter-Oganessian, Physics of the Solid State **54**, 311 (2012).

[45] V. P. Sakhnenko and N. V. Ter-Oganessian, Crystallography Reports **57**, 112 (2012).

[46] O. Kondo, M. Ono, E. Sugiura, K. Sugiyama, and M. Date, Journal of the Physical Society of Japan **57**, 3293 (1988).

[47] M. L. Plumer, Phys. Rev. B **78**, 094402 (2008).

[48] S. G. Condran and M. L. Plumer, Journal of Physics: Condensed Matter **22**, 162201 (2010).

[49] G. Quirion, X. Han, and M. L. Plumer, Phys. Rev. B **84**, 014408 (2011).

[50] A. B. Kuz'menko, D. van der Marel, P. J. M. van Bentum, E. A. Tishchenko, C. Presura, and A. A. Bush, Phys. Rev. B **63**, 094303 (2001).

[51] M. Ain, A. Menelle, B. M. Wanklyn, and E. F. Bertaut, Journal of Physics: Condensed Matter **4**, 5327 (1992).

[52] B. X. Yang, J. M. Tranquada, and G. Shirane, Phys. Rev. B **38**, 174 (1988).

[53] S. Åsbrink and L.-J. Norrby, Acta Crystallographica Section B **26**, 8 (1970).

[54] J. C. Bonner and M. E. Fisher, Phys. Rev. **135**, A640 (1964).

[55] B. X. Yang, T. R. Thurston, J. M. Tranquada, and G. Shirane, Phys. Rev. B **39**, 4343 (1989).

[56] M. O'keeffe and F. Stone, Journal of Physics and Chemistry of Solids **23**, 261 (1962).

[57] X. Rocquefelte, M.-H. Whangbo, A. Villesuzanne, S. Jobic, F. Tran, K. Schwarz, and P. Blaha, Journal of Physics: Condensed Matter **22**, 045502 (2010).

[58] A.-M. Pradipto, R. Maurice, N. Guihéry, C. de Graaf, and R. Broer, Phys. Rev. B **85**, 014409 (2012).

[59] J. B. Goodenough and A. L. Loeb, Phys. Rev. **98**, 391 (1955).

[60] H. Yamada, X.-G. Zheng, Y. Soejima, and M. Kawaminami, Phys. Rev. B **69**, 104104 (2004).

[61] G. Kliche and Z. V. Popovic, Phys. Rev. B **42**, 10060 (1990).

[62] J. C. Irwin and T. Wei, Journal of Physics: Condensed Matter **3**, 299 (1991).

[63] D. Dai, H.-J. Koo, and M.-H. Whangbo, Inorganic Chemistry **43**, 4026 (2004).

[64] S. Jung, J. Kim, E. J. Choi, Y. Sekio, T. Kimura, and J. Lorenzana, Phys. Rev. B **80**, 140516 (2009).

[65] W. B. Wu, D. J. Huang, J. Okamoto, S. W. Huang, Y. Sekio, T. Kimura, and C. T. Chen, Phys. Rev. B **81**, 172409 (2010).

[66] M. Ain, W. Reichardt, B. Hennion, G. Pepy, and B. Wanklyn, Physica C: Superconductivity p. 1279 (1989).

[67] A. Boothroyd, A. Mukherjee, S. Fulton, T. Perring, R. Eccleston, H. Mook, and B. Wanklyn, Physica B: Condensed Matter pp. 731 – 733 (1997).

[68] U. Köbler and T. Chattopadhyay, Zeitschrift für Physik B Condensed Matter **82**, 383 (1991).

[69] T. Arbuzova, I. Smolyak, A. Samokhvalov, and S. Naumov, Journal of Experimental and Theoretical Physics **86**, 559 (1998).

[70] T. Shimizu, T. Matsumoto, A. Goto, T. V. Chandrasekhar Rao, K. Yoshimura, and K. Kosuge, Phys. Rev. B **68**, 224433 (2003).

[71] M. Seehra, Z. Feng, and R. Gopalakrishnan, Journal of Physics C: Solid State Physics **21**, L1051 (1988).

[72] T. Chattopadhyay, G. McIntyre, P. Brown, and J. Forsyth, Physica C: Superconductivity **170**, 371 (1990).

[73] W. Reichardt, F. Gompf, M. Aïn, and B. M. Wanklyn, Zeitschrift für Physik B Condensed Matter **81**, 19 (1990).

[74] J. van den Brink and D. I. Khomskii, Journal of Physics: Condensed Matter **20**, 434217 (2008).

[75] C. Bucci and R. Fieschi, Phys. Rev. Lett. **12**, 16 (1964).

[76] T. Moriya, Phys. Rev. **120**, 91 (1960).

[77] I. Dzyaloshinsky, Journal of Physics and Chemistry of Solids **4**, 241 (1958).

[78] P. Babkevich, A. Poole, R. D. Johnson, B. Roessli, D. Prabhakaran, and A. T. Boothroyd, Phys. Rev. B **85**, 134428 (2012).

[79] R. Truell, C. Elbaum, and B. Chick, *Ultrasonic methods in solid state physics* (Academic Press, 1969).

[80] E. Dieulesaint and D. Royer, *Elastic Waves in Solids: Applications to Signal Processing* (J. Wiley, 1980).

[81] A. Harker, *Elastic Waves in Solids with Applications to Nondestructive Testing of Pipelines*, British Gas technical monographs (A. Hilger in association with British Gas, 1988).

[82] N. Ashcroft and N. Mermin, *Solid State Physics*, Science: Physics (Saunders College, 1976).

[83] M. L. Plumer, Phys. Rev. B **44**, 12376 (1991).

[84] C. R. Bradley and A. P. Cracknell, *The Mathematical Theory of Symmetry in Solids* (1972).

[85] G. Quirion, M. L. Plumer, O. A. Petrenko, G. Balakrishnan, and C. Proust, Phys. Rev. B **80**, 064420 (2009).

[86] G. Quirion, X. Han, M. L. Plumer, and M. Poirier, Phys. Rev. Lett. **97**, 077202 (2006).

[87] C. Kittel, *Introduction to Solid State Physics* (Wiley, 1971).

[88] S. Sachdev, *Quantum Phase Transitions* (Cambridge University Press, 2011).

[89] D. Khomskii, *Basic Aspects of the Quantum Theory of Solids: Order and Elementary Excitations* (Cambridge University Press, 2010).

[90] L. D. Landau and E. M. Lifshitz, *Statistical Physics* (Pergamon Press, 1978).

[91] J. Tolédano and P. Tolédano, *The Landau Theory of Phase Transitions: Application to Structural, Incommensurate, Magnetic, and Liquid Crystal Systems*, World Scientific Lecture Notes in Physics (World Scientific, 1987).

[92] N. Spaldin, *Magnetic Materials: Fundamentals and Applications* (Cambridge University Press, 2010).

[93] H. T. Diep, *Magnetic Systems with Competing Interactions: Frustrated Spin Systems* (World Scientific, 1994).

[94] M. L. Plumer, K. Hood, and A. Caillé, Phys. Rev. Lett. **60**, 45 (1988).

[95] M. L. Plumer and A. Caillé, Phys. Rev. B **37**, 7712 (1988).

[96] S. Matityahu, A. Aharony, and O. Entin-Wohlman, Phys. Rev. B **85**, 174408 (2012).

[97] P. Tolédano, Phys. Rev. B **79**, 094416 (2009).

[98] P. Tolédano, B. Mettout, W. Schranz, and G. Krexner, Journal of Physics: Condensed Matter **22**, 065901 (2010).

[99] D. O'Flynn, C. V. Tomy, M. R. Lees, A. Daoud-Aladine, and G. Balakrishnan, Phys. Rev. B **83**, 174426 (2011).

[100] T. Kimura, G. Lawes, T. Goto, Y. Tokura, and A. P. Ramirez, Phys. Rev. B **71**, 224425 (2005).

[101] V. Felea, P. Lemmens, S. Yasin, S. Zherlitsyn, K. Y. Choi, C. T. Lin, and C. Payen, Journal of Physics: Condensed Matter **23**, 216001 (2011).

Appendix A

Mathematica notebook

The Mathematica code related to some of the calculations necessary for this project is attached here. In Section A.1, I show how to calculate the sound velocities. In Section A.2, a similar demonstration is done for the anisotropic exchange coefficients. In Section A.3, all the terms in the Landau-type free energy are calculated using the spin density. The expressions for the phase boundaries, in the case of only one anisotropic contribution - magnetic easy axis (D_y), are deduced. Lastly, a simple example of the numerical minimization for a given temperature and magnetic field values is presented.

A.1 Sound velocity

The solutions for the velocities can be calculated by using the Christoffel equation for different directions of propagation.

	$v^2\rho$	eigenvectors		
[100]	$\frac{1}{2}\left(C_{11}+C_{55}-\sqrt{C_{11}^2-2C_{55}C_{11}+4C_{15}^2+C_{55}^2}\right)$	$-\frac{-C_{11}+C_{55}+\sqrt{C_{11}^2-2C_{55}C_{11}+4C_{15}^2+C_{55}^2}}{2C_{15}}$	0	1
	$\frac{1}{2}\left(C_{11}+C_{55}+\sqrt{C_{11}^2-2C_{55}C_{11}+4C_{15}^2+C_{55}^2}\right)$	$\frac{C_{11}-C_{55}+\sqrt{C_{11}^2-2C_{55}C_{11}+4C_{15}^2+C_{55}^2}}{2C_{15}}$	0	1
	C_{66}	0	1	0
[010]	C_{22}	0	1	0
	$\frac{1}{2}\left(C_{44}+C_{66}-\sqrt{C_{44}^2-2C_{66}C_{44}+4C_{46}^2+C_{66}^2}\right)$	$-\frac{C_{44}-C_{66}+\sqrt{C_{44}^2-2C_{66}C_{44}+4C_{46}^2+C_{66}^2}}{2C_{46}}$	0	1
	$\frac{1}{2}\left(C_{44}+C_{66}+\sqrt{C_{44}^2-2C_{66}C_{44}+4C_{46}^2+C_{66}^2}\right)$	$\frac{-C_{44}+C_{66}+\sqrt{C_{44}^2-2C_{66}C_{44}+4C_{46}^2+C_{66}^2}}{2C_{46}}$	0	1
[001]	C_{44}	0	1	0
	$\frac{1}{2}\left(C_{33}+C_{55}-\sqrt{C_{33}^2-2C_{55}C_{33}+4C_{35}^2+C_{55}^2}\right)$	$-\frac{C_{33}-C_{55}+\sqrt{C_{33}^2-2C_{55}C_{33}+4C_{35}^2+C_{55}^2}}{2C_{35}}$	0	1
	$\frac{1}{2}\left(C_{33}+C_{55}+\sqrt{C_{33}^2-2C_{55}C_{33}+4C_{35}^2+C_{55}^2}\right)$	$\frac{-C_{33}+C_{55}+\sqrt{C_{33}^2-2C_{55}C_{33}+4C_{35}^2+C_{55}^2}}{2C_{35}}$	0	1

(A.1)

A.2 Anisotropy

Same procedure is followed to calculate the invariant exchange coefficients that must be considered in the Hamiltonian.

JT2 = Table $[J_{i,j}, \{i, 3\}, \{j, 3\}]$;

For $[i = 1, i \leq 3,$ For $[j = 1, j \leq 3, J_{j,i} = J_{i,j}; j{+}{+}]; i{+}{+}]$;

Print["Exchange coefficients"]

Print[" J = ", JT = MatrixForm[JT2]]

sf[α_, i_, j_, CC_]:= $\sum_{p=1}^{3} \sum_{q=1}^{3} \alpha[[i, p]]\alpha[[j, q]]CC[[p, q]]$;

Print["Generator"]

α2y = RotationMatrix[Pi, {0, 1, 0}];

Print $\left["C_2^b = ", \alpha 2y\right]$

Print["Symmetry operation"]

Print $\left[\text{"J' = ", "} \sum_{p=1}^{3} \sum_{q=1}^{3} \text{"MatrixForm}[\alpha 2y], \text{MatrixForm}[\alpha 2y]\text{MatrixForm[JT]}\right]$

Exchange coefficients

$$J = \begin{pmatrix} J_{11} & J_{12} & J_{13} \\ J_{12} & J_{22} & J_{23} \\ J_{13} & J_{23} & J_{33} \end{pmatrix} \tag{A.2}$$

Generator

$$C_2^y = \begin{pmatrix} -1 & 0 & 0 \\ 0 & 1 & 0 \\ 0 & 0 & -1 \end{pmatrix} \tag{A.3}$$

Symmetry operation

$$J' = \sum_{p=1}^{3}\sum_{q=1}^{3} \begin{pmatrix} -1 & 0 & 0 \\ 0 & 1 & 0 \\ 0 & 0 & -1 \end{pmatrix} \begin{pmatrix} -1 & 0 & 0 \\ 0 & 1 & 0 \\ 0 & 0 & -1 \end{pmatrix} \begin{pmatrix} J_{11} & J_{12} & J_{13} \\ J_{12} & J_{22} & J_{23} \\ J_{13} & J_{23} & J_{33} \end{pmatrix} \tag{A.4}$$

JTP2 = Table[0, {i, 3}, {j, 3}];

For[i = 1, i ≤ 3, For[j = 1, j ≤ 3, JTP2[[i, j]] = sf[α2y, i, j, JT2]; j++]; i++]

DIF = Simplify[JTP2 − JT2];

For [i = 1, i ≤ 3, For [j = 1, j ≤ 3, If [DIF[[i, j]]===0, , $J_{i,j}$ = 0] ; j++] ; i++]

Print["Invariant exchange coefficients"]

Print[" J' = ", MatrixForm[JTP2]]

s = {s1, s2, s3};

H = Table[0, {i, 1, 3}, {j, 1, 3}];

$H = \sum_{\mu=1}^{3} \sum_{\nu=1}^{3} \mathrm{JTP2}[[\mu, \nu]] s[[\mu]] s[[\nu]];$

$\mathrm{Print}[\text{“Invariant Hamiltonian”}]$

$\mathrm{Print}[\text{“H = ”}, \mathrm{Simplify}[H]]$

Invariant exchange coefficients

$$J' = \begin{pmatrix} J_{11} & 0 & J_{13} \\ 0 & J_{22} & 0 \\ J_{13} & 0 & J_{33} \end{pmatrix} \tag{A.5}$$

Invariant Hamiltonian

$$H = J_{11} s_1^2 + J_{22} s_2^2 + J_{33} s_3^2 + 2 J_{13} s_1 s_3 \tag{A.6}$$

A.3 Landau model

$\mathrm{s1v} = \{-S\mathrm{Cos}[\beta]\mathrm{Sin}[\gamma]\mathrm{Sin}[\alpha], S\mathrm{Cos}[\beta]\mathrm{Cos}[\gamma], S\mathrm{Cos}[\beta]\mathrm{Sin}[\gamma]\mathrm{Cos}[\alpha]\};$

$\mathrm{s2v} = \{S\mathrm{Sin}[\beta](\mathrm{Cos}[\theta]\mathrm{Cos}[\alpha] - \mathrm{Sin}[\theta]\mathrm{Sin}[\gamma]\mathrm{Sin}[\alpha]), S\mathrm{Sin}[\beta]\mathrm{Sin}[\theta]\mathrm{Cos}[\gamma], S\mathrm{Sin}[\beta](\mathrm{Sin}[\theta]\mathrm{Sin}[\gamma]\mathrm{Cos}[\alpha] + \mathrm{Cos}[\theta]\mathrm{Sin}[\alpha])\};$

$\mathrm{Sr} = (\mathrm{S1} + i\mathrm{S2})e^{i\phi};$

$\mathrm{Sc} = \mathrm{Sr}/.i \to -i;$

$\mathrm{SrSc} = \mathrm{Simplify}[\mathrm{ComplexExpand}[\mathrm{SrSc}]];$

$$\text{subS} = \left\{\text{S1}^2 \to \text{S1.S1}, \text{S2}^2 \to \text{S2.S2}, \text{S1S2} \to \text{S1.S2}\right\};$$

$$\text{Print}\left["\text{S.}S^* = ", \text{SrSc} = \text{SrSc}/.\text{subS}\right]$$

$$\text{Print}\left["\text{Sy Sy}^* = ", \text{SryScy} = \text{Expand}[\text{SrSc}]/.\left\{\text{S1}^2 \to \text{S1yS1y}, \text{S2}^2 \to \text{S2yS2y}, \text{S1S2} \to \text{S1yS2y}\right\}\right]$$

$$\text{Print}\left["\text{Sx Sz}^* + \text{Sx}^* \text{Sz} = ",\right.$$

$$\text{SxSz} = \text{Expand}[(\text{Sr}/.\{\text{S1} \to \text{s1v}[[1]], \text{S2} \to \text{s2v}[[1]]\})(\text{Sc}/.\{\text{S1} \to \text{s1v}[[3]], \text{S2} \to \text{s2v}[[3]]\})]+$$

$$\left.\text{Expand}[(\text{Sc}/.\{\text{S1} \to \text{s1v}[[1]], \text{S2} \to \text{s2v}[[1]]\})(\text{Sr}/.\{\text{S1} \to \text{s1v}[[3]], \text{S2} \to \text{s2v}[[3]]\})]\right]$$

$$\text{Print}\left["\text{Sz Sz}^* = ", \text{SrzScz} = \text{Expand}[\text{SrSc}]/.\left\{\text{S1}^2 \to \text{S1zS1z}, \text{S2}^2 \to \text{S2zS2z}, \text{S1S2} \to \text{S1zS2z}\right\}\right]$$

$$\text{Print}[\text{“(S.S) = ”}, \text{SrSr} = \text{Expand}[\text{SrSr}]/.\text{subS}]$$

$$\text{Print}\left["\text{(S.S)}^* = ", \text{SrSrc} = \text{SrSr}/.\{2i \to -2i\}\right]$$

$$\text{Print}\left["(\text{S.}S^*)^2 = ", \text{SrSc2} = \text{Expand}\left[\text{SrSc}^2\right]\right]$$

$$\text{Print}\left["|\text{S.S}|^2 = ", \text{SS2} = \text{Expand}[\text{SrSrSrSrc}]\right]$$

$$\text{S4U} = \text{Expand}\left[\text{SrSr}^2 + \text{SrSrc}^2\right];$$

$$\text{xx} = \text{ComplexExpand}\left[\text{Expand}\left[\text{S4U}/.e^{i4\phi} \to 1/.e^{-i4\phi} \to 0\right]e^{i4\phi} + \text{Expand}\left[\text{S4U}/.e^{-i4\phi} \to 1/.e^{i4\phi} \to 0\right]e^{-i4\phi}\right];$$

$$S.S^* = \text{S1.S1} + \text{S2.S2} \tag{A.7}$$

$$S_y \text{Sy}^* = \text{S1y}^2 + \text{S2y}^2 \tag{A.8}$$

$$\begin{aligned}\mathrm{Sx\ Sz^*} + \mathrm{Sx^*\ Sz} &= -2S^2\cos(\alpha)\sin(\alpha)\sin^2(\gamma)\sin^2(\theta)\sin^2(\beta) + 2S^2\cos(\alpha)\cos^2(\theta)\sin(\alpha)\sin^2(\beta) \\ &- 2S^2\cos(\theta)\sin^2(\alpha)\sin(\gamma)\sin(\theta)\sin^2(\beta) + 2S^2\cos^2(\alpha)\cos(\theta)\sin(\gamma)\sin(\theta)\sin^2(\beta) \\ &- 2S^2\cos(\alpha)\cos^2(\beta)\sin(\alpha)\sin^2(\gamma) \end{aligned} \tag{A.9}$$

$$\mathrm{Sz\ Sz^*} = \mathrm{S1z^2} + \mathrm{S2z^2} \tag{A.10}$$

$$\mathrm{(S.S)} = e^{2i\phi}\mathrm{S1.S1} + 2ie^{2i\phi}\mathrm{S1.S2} - e^{2i\phi}\mathrm{S2.S2} \tag{A.11}$$

$$\mathrm{(S.S)^*} = e^{-2i\phi}\mathrm{S1.S1} - 2ie^{-2i\phi}\mathrm{S1.S2} - e^{-2i\phi}\mathrm{S2.S2} \tag{A.12}$$

$$\mathrm{(S.S^*)^2} = \mathrm{(S1.S1)^2} + \mathrm{2S2.S2S1.S1} + \mathrm{(S2.S2)^2} \tag{A.13}$$

$$\mathrm{|S.S|^2} = \mathrm{(S1.S1)^2} - \mathrm{2S2.S2S1.S1} + 4\mathrm{(S1.S2)^2} + \mathrm{(S2.S2)^2} \tag{A.14}$$

A.3.1 Only one anisotropic contribution - (D_y)

subm = $\left\{S^2 \to S.S, (S^*)^2 \to S^*.S^*, SS^* \to S.S^*, mS \to m.S, mS^* \to m.S^*\right\}$;

ρ[R_] = $m + Se^{iQR} + S^*e^{-iQR}$;

xx = Expand[$\rho[R]\rho[R]$]/.subm;

yy = Expand[$\rho[R]\rho[R]$]/.subm;

zz = Expand[xxyy]zz0 = zz/. $\{\Delta_{Q,G} \to 0, \Delta_{2Q,G} \to 0, \Delta_{3Q,G} \to 0, \Delta_{4Q,G} \to 0\}$;

Simplify [zz − zz0/. $\{\Delta_{2Q,G} \to 0, \Delta_{3Q,G} \to 0, \Delta_{4Q,G} \to 0\}$];

Simplify [zz − zz0/. $\{\Delta_{Q,G} \to 0, \Delta_{3Q,G} \to 0, \Delta_{4Q,G} \to 0\}$];

Simplify [zz − zz0/. $\{\Delta_{2Q,G} \to 0, \Delta_{Q,G} \to 0, \Delta_{4Q,G} \to 0\}$];

zzu = Simplify [zz − zz0/. $\{\Delta_{2Q,G} \to 0, \Delta_{3Q,G} \to 0, \Delta_{Q,G} \to 0\}$];

subm = $\{m$S1 $\to m.$S1, mS2 $\to m.$S2$\}$;

subm = $\{m$S1 $\to m.$S1, mS2 $\to m.$S2$\}$;

mSrmSc = Expand[(Expand[(mSr)]/.subm)(Expand[(mSc)]/.subm)];

Print[

"F_L = AQ S.S^* + D_y $|S_y|^2$ + B_1 (S.S^*)^2 + $\frac{1}{2}B_2$|S.S|^2 + $\frac{B_4}{4}$((S.S)^2+($S^*.S^*$)^2) $\Delta_{4Q,G}$ + $\frac{1}{2}A_o m^2$ + $\frac{1}{4}B_3 m^4$+ 2 B_4|m.S|^2

+ $B_5 m^2$ S.S^*- m.H"]

Print ["F_2 = ", F2 = AQSrSc + DySryScy]

Print ["F_4 = ", F4 = B1SrSc2 + $\frac{B2}{2}$SS2]

Print ["F_U = ", FU = $\frac{BU}{4}$S4U]

Print ["F_H = ", FH = $\frac{1}{2}$A0($m.m$) + $\frac{1}{4}$B3$(m.m)^2$ + 2B4mSrmSc + B5$m.m$SrSc − $m.H$]

$$\begin{aligned} F_L &= AQS.S^* + D_y\ |S_y|^2 + B_1\ (\mathrm{S}.S^*)^2 + \frac{1}{2}B_2|\mathrm{S}.\mathrm{S}|^2 + \frac{B_u}{4}((\mathrm{S}.\mathrm{S})^2+(S^*.S^*)^2)\Delta_{4Q,G} + \frac{1}{2}A_o m^2 + \frac{1}{4}B_3 m^4 \\ &+ 2B_4|\mathrm{m}.\mathrm{S}|^2 + B_5 m^2\ \mathrm{S}.S^*\text{- m.H} \end{aligned} \tag{A.15}$$

$$F_2 = \mathrm{Dy}\left(\mathrm{S1y}^2 + \mathrm{S2y}^2\right) + \mathrm{AQ}(\mathrm{S1}.\mathrm{S1} + \mathrm{S2}.\mathrm{S2}) \tag{A.16}$$

$$F_4 = \frac{1}{2}\mathrm{B2}\left((\mathrm{S1}.\mathrm{S1})^2 - 2\mathrm{S2}.\mathrm{S2S1}.\mathrm{S1} + 4(\mathrm{S1}.\mathrm{S2})^2 + (\mathrm{S2}.\mathrm{S2})^2\right) + \mathrm{B1}\left((\mathrm{S1}.\mathrm{S1})^2 + 2\mathrm{S2}.\mathrm{S2S1}.\mathrm{S1} + (\mathrm{S2}.\mathrm{S2})^2\right) \tag{A.17}$$

$$
\begin{aligned}
F_U &= \frac{1}{4}\mathrm{BU}(e^{-4i\phi}(\mathrm{S1.S1})^2 + e^{4i\phi}(\mathrm{S1.S1})^2 - 4ie^{-4i\phi}\mathrm{S1.S2S1.S1} + 4ie^{4i\phi}\mathrm{S1.S2S1.S1} - 2e^{-4i\phi}\mathrm{S2.S2S1.S1} \\
&- 2e^{4i\phi}\mathrm{S2.S2S1.S1} - 4e^{-4i\phi}(\mathrm{S1.S2})^2 - 4e^{4i\phi}(\mathrm{S1.S2})^2 + e^{-4i\phi}(\mathrm{S2.S2})^2 + e^{4i\phi}(\mathrm{S2.S2})^2 + 4ie^{-4i\phi}\mathrm{S1.S2S2.S2} \\
&- 4ie^{4i\phi}\mathrm{S1.S2S2.S2}) \qquad \text{(A.18)}
\end{aligned}
$$

$$
F_H = \frac{1}{4}\mathrm{B3}(m.m)^2 + \frac{\mathrm{A0}m.m}{2} + \mathrm{B5}(\mathrm{S1.S1} + \mathrm{S2.S2})m.m + 2\mathrm{B4}\left((m.\mathrm{S1})^2 + (m.\mathrm{S2})^2\right) - m. \qquad \text{(A.19)}
$$

A.3.1.1 Only one anisotropic contribution - Reduced

$\mathbf{mv} = \{0, \mathbf{mb}, 0\};$

$\mathbf{Hv} = \{0, \mathbf{hb}, 0\};$

$\mathbf{subv} = \{\mathbf{S1} \to \mathbf{s1v}, \mathbf{S2} \to \mathbf{s2v}, \mathbf{S1y} \to \mathbf{s1v[[2]]}, \mathbf{S2y} \to \mathbf{s2v[[2]]}, m \to \mathbf{mv}, H \to \mathbf{Hv}\};$

$\mathbf{subt} = \{\mathbf{Cos}[\beta]^2 \to 1 - \mathbf{Sin}[\beta]^2, \mathbf{Sin}[\theta]^2 \to 1 - \mathbf{Cos}[\theta]^2, \mathbf{Sin}[\gamma]^2 \to 1 - \mathbf{Cos}[\gamma]^2, \alpha \to 0\};$

$\mathbf{F2} = \mathbf{Expand}[\mathbf{Expand}[\mathbf{F2}/.\mathbf{subv}/.\mathbf{subt}]/.\mathbf{subt}];$

$\mathbf{F4} = \mathbf{Expand}[\mathbf{Expand}[\mathbf{F4}/.\mathbf{subv}/.\mathbf{subt}]/.\mathbf{subt}];$

$\mathbf{FU} = \mathbf{Expand}[\mathbf{Expand}[\mathbf{FU}/.\mathbf{subv}/.\mathbf{subt}]/.\mathbf{subt}];$

$\mathbf{FH} = \mathbf{Expand}[\mathbf{Expand}[\mathbf{FH}/.\mathbf{subv}/.\mathbf{subt}]/.\mathbf{subt}];$

```
Print["Sβ = S Sin(β)"]
Print["ζ = Cos(θ)"]
Print["κ = Cos(γ)"]
Print ["F2 = ", F2t = Expand [F2/. {Cos[γ]^2 → κ^2, Cos[θ]^2 → ζ^2, Sin[β]^2 → Sβ^2/S^2}]]
Print ["F4 = ",
F4t =
Expand [F4/. {Cos[θ]^2 → ζ^2, Sin[β]^4 → Sβ^4/S^4, Sin[β]^2 → Sβ^2/S^2, Sin[γ]^4 → (1 - κ^2)^2, Cos[γ]^2 → κ^2, Cos[θ]^4 → ζ^4, Sin[θ]^4 → (1 - ζ^2)^2,
 Cos[γ]^4 → κ^4}]]
Print ["FU = ",
FUT =
Expand [FU/. {ϕ → 0, Cos[θ]^2 → ζ^2, Sin[β]^4 → Sβ^4/S^4, Sin[β]^2 → Sβ^2/S^2, Sin[γ]^4 → (1 - κ^2)^2, Cos[γ]^2 → κ^2, Cos[θ]^4 → ζ^4,
 Sin[θ]^4 → (1 - ζ^2)^2, Cos[γ]^4 → κ^4}]]
Print ["FH = ", FHt = Expand [FH/. {Cos[γ]^2 → κ^2, Cos[θ]^2 → ζ^2, Sin[β]^2 → Sβ^2/S^2}]]
```

$$S\beta = S\ \mathrm{Sin}(\beta) \tag{A.20}$$

$$\zeta = \mathrm{Cos}(\theta) \tag{A.21}$$

$$\kappa = \mathrm{Cos}(\gamma) \tag{A.22}$$

$$F_2 = \mathrm{Dy}\kappa^2 S^2 + \mathrm{AQ}S^2 - \mathrm{DyS}\beta^2\zeta^2\kappa^2 \tag{A.23}$$

$$F_4 = \mathrm{B1}S^4 + \frac{\mathrm{B2}S^4}{2} - 2\mathrm{B2S}\beta^2\zeta^2 S^2 + 2\mathrm{B2S}\beta^4\zeta^2 \tag{A.24}$$

$$F_U = \frac{\mathrm{BU}S^4}{2} - 4\mathrm{BUS}\beta^2 S^2 + 2\mathrm{BUS}\beta^2\zeta^2 S^2 + 4\mathrm{BUS}\beta^4 - 2\mathrm{BUS}\beta^4\zeta^2 \tag{A.25}$$

$$F_H = \frac{\mathrm{B3mb}^4}{4} + \mathrm{B5}S^2\mathrm{mb}^2 + 2\mathrm{B4}S^2\kappa^2\mathrm{mb}^2 - 2\mathrm{B4S}\beta^2\zeta^2\kappa^2\mathrm{mb}^2 + \frac{\mathrm{A0mb}^2}{2} - \mathrm{hbmb} \tag{A.26}$$

A.3.1.2 Only one anisotropic contribution - Phase boundaries

$\mathbf{FSF = FT/.\left\{S\beta \to S\,Sin\left[\frac{\pi}{4}\right], \zeta \to 1, \kappa \to \kappa\right\};}$

$\mathbf{DS = Expand\left[\frac{D[FSF,S]}{S}\right];}$

$\mathbf{DS\beta = Expand\left[\frac{D[FSF,S\beta]}{S\beta}\right];}$

$\mathbf{Dm = D[FSF, mb];}$

$$\text{Solve}\left[(\text{FSF}/.\kappa \to 0) - (\text{FSF}/.\kappa \to 1) == 0/.\text{mb} \to \sqrt{\text{mm}}, \text{mm}\right];$$

$$\text{mSF} = \sqrt{\text{mm}}/.\%[[1]];$$

$$\text{Solve}\left[\text{DS} == 0/.\text{mb} \to \text{mSF}/.S \to \sqrt{\text{SS}}, \text{SS}\right];$$

$$\text{SSF} = \sqrt{\text{SS}}/.\%[[1]];$$

$$\text{Solve}[\text{Expand}[\text{Dm}/.\text{mb} \to \text{mSF}/.S \to \text{SSF}] == 0, \text{hb}];$$

$$\text{HSF} = \text{hb}/.\%[[1]];$$

$$\text{FSF3} = (\text{FT} + \text{FUT})/.\left\{\text{S}\beta \to S\text{Sin}\left[\frac{\pi}{4}\right], \zeta \to 0\right\};$$

$$\text{DS3} = \text{Expand}\left[\frac{D[\text{FSF3}, S]}{S}\right];$$

$$\text{DS}\beta\text{3} = \text{Expand}\left[\frac{D[\text{FSF3}, \text{S}\beta]}{\text{S}\beta}\right];$$

$$\text{Dm3} = D[\text{FSF3}, \text{mb}];$$

$$\text{Solve}\left[(\text{FSF3}/.\kappa \to 1) - (\text{FSF3}/.\kappa \to 0) == 0/.\text{mb} \to \sqrt{\text{mm}}, \text{mm}\right];$$

$$\text{mSF3} = \sqrt{\text{mm}}/.\%[[1]];$$

$$\text{Solve}\left[\text{DS3} == 0/.\text{mb} \to \text{mSF3}/.S \to \sqrt{\text{SS}}, \text{SS}\right];$$

$$\text{SSF3} = \sqrt{\text{SS}}/.\%[[1]];$$

$$\text{Solve}[\text{Expand}[\text{Dm3}/.\text{mb} \to \text{mSF3}/.S \to \text{SSF3}/.\zeta \to 0] == 0, \text{hb}];$$

$$\text{HSF3} = \text{hb}/.\%[[1]];$$

$$\text{HSF31} = \text{Simplify}[\text{HSF3}/.\kappa \to 1];$$

$$\text{HSF30} = \text{Simplify}[\text{HSF3}/.\kappa \to 0];$$

$T=.$

Simplify[Solve[htn3 == 0/.{A0 → a(T − To), AQ → a(T − TQ)}/.{κ → 1}, T]];

Print ["T_{N1} = ", TN1s = T/.%[[1]]]

Expand[Solve[h2 == 0/.{A0 → a(T − To), AQ → a(T − TQ)}/.{κ → 1}, T]];

Print ["T_{N2} = ", TN2s = T/.%[[1]]]

Simplify [Expand [mtn3^2 − mtn2^2] /.κ → 1/.{A0 → a(T − To), AQ → a(T − TQ)}] ;

Simplify[Solve[% == 0, T]];

Print ["T_M = ", TM = T/.%[[1]]]

Hc2T = Simplify $\left[\text{htn3}^2/.\{\text{A0} \to a(T - \text{To}), \text{AQ} \to a(T - \text{TQ})\}/.\kappa \to 0\right]$;

Print ["$H^2{}_C$ = ", H2CT0 = %/.T → 0]

$$T_{\mathrm{N1}} = \mathrm{TQ} - \frac{\mathrm{Dy}}{a} \tag{A.27}$$

$$T_{\mathrm{N2}} = -\frac{\mathrm{Dy}}{2a} + \frac{\mathrm{B1Dy}}{a\mathrm{B2}} + \mathrm{TQ} \tag{A.28}$$

$$T_M = \frac{\mathrm{B5Dy}}{2a\mathrm{B4}} + \mathrm{TQ} \tag{A.29}$$

$$H^2{}_C = \frac{a^3 \mathrm{TQ}(\mathrm{B3TQ} - \mathrm{B5To})^2}{\mathrm{B5}^3} \tag{A.30}$$

A.3.2 All anisotropic contributions

Print[

"F = AQ S.S^* + D_y $|S_y|^2$ + $D_{xz} S_x S_z$ + D_z $|S_z|^2$ + B_1 (S.S^*)^2 + $\frac{1}{2} B_2$|S.S|^2 + $\frac{B_4}{4}$((S.S)^2+(S^*.S^*)^2) $\Delta_{4Q,G}$ + $\frac{1}{2} A_o m^2$

+ $\frac{1}{4} B_3 m^4$+ 2 B_4|m.S|^2 + $B_5 m^2$ S.S^*- m.H"]

F2 = AQSrSc;

F4 = B1SrSc2 + $\frac{\mathrm{B2}}{2}$SS2;

FA = DySryScy + DzSrzScz + DxzSxSz;

FU = $\frac{\mathrm{BU}}{4}$S4U;

FH = $\frac{1}{2}$A0($m.m$) + $\frac{1}{4}$B3($m.m$)^2 + 2B4mSrmSc + B5$m.m$SrSc − $m.H$;

mv = {0, mb, 0};

Hv = {0, hb, 0};

subv = {S1 → s1v, S2 → s2v, S1y → s1v[[2]], S2y → s2v[[2]], m → mv, H → Hv, S1z → s1v[[3]], S2z → s2v[[3]]};

subt = {Cos[β]^2 → 1 − Sin[β]^2, Sin[θ]^2 → 1 − Cos[θ]^2, Sin[γ]^2 → 1 − Cos[γ]^2, Sin[γ]^4 → 1 − 2Cos[γ]^2 + Cos[γ]^4,

Sin[θ]^4 → 1 − 2Cos[θ]^2 + Cos[θ]^4} ;

F2 = Expand[(F2 + FA)/.subv/.subt];

$$\text{F4} = \text{Expand}[\text{Expand}[\text{F4}/.\text{subv}/.\text{subt}]/.\text{subt}];$$

$$\text{FU} = \text{Expand}[\text{Expand}[\text{FU}/.\text{subv}/.\text{subt}]/.\text{subt}];$$

$$\text{FH} = \text{Expand}[\text{Expand}[\text{FH}/.\text{subv}/.\text{subt}]/.\text{subt}];$$

$$\text{subs} = \left\{\text{Cos}[\gamma]^2 \to \kappa^2, \text{Cos}[\theta]^2 \to \zeta^2, \text{Cos}[\theta]^4 \to \zeta^4, \text{Sin}[\beta]^4 \to \frac{\text{S}\beta^4}{S^4}, \text{Sin}[\beta]^2 \to \frac{\text{S}\beta^2}{S^2}, \text{Cos}[\gamma]^4 \to \kappa^4, \text{Sin}[\gamma]^2 \to 1 - \kappa^2\right\};$$

$$\text{F2t} = \text{Simplify}[\text{F2}/.\text{subs}];$$

$$\text{F4t} = \text{Simplify}[\text{F4}/.\text{subs}];$$

$$\text{FUT} = \text{Simplify}[\text{FU}/.\text{subs}];$$

$$\text{FHt} = \text{Simplify}[\text{FH}/.\text{subs}];$$

$$\text{Expand}\left[\partial_\alpha \text{F2}/.\theta \to 0/.\gamma \to 0\right];$$

$$\alpha\text{n} = N\left[\frac{2\pi}{360}(70)\right];$$

$$N[\text{Cos}[\alpha\text{n}]];$$

$$\text{Solve}\left[\partial_\alpha \text{F2} == 0/.\theta \to 0/.\gamma \to 0/.\alpha \to N[\alpha\text{n}], \text{Dxz}\right];$$

$$\text{Axzs} = -\text{Dxz}/.\%[[1]];$$

$$\text{Azzn} = 0.01;$$

$$\text{Axzn} = \text{Axzs}/.\text{Dz} \to \text{Azzn}/.\alpha\text{->}\alpha\text{n};$$

$$\text{coef} = \{\text{TQ} \to 1.18, \text{T0} \to -1.0, \text{Tu} \to 1.15, a \to 1.0, \text{Dy} \to -0.02, \text{Dz} \to -\text{Azzn}, \text{B1} \to 0.1025, \text{B2} \to 0.0108, \text{B3} \to 0.0633,$$

$$\text{B4} \to 0.0125, \text{BU} \to 0.0352, \text{B5} \to 0.1, \text{Dxz} \to \text{Axzn}\};$$

$$\text{FTn}=.$$

$\mathbf{FT = F2t + F4t + FHt;}$

$\mathbf{FTn[T\_, hb\_] = FT/.AQ \to a(T - TQ)/.A0 \to a(T - T0)/.S\beta \to S Sin[\beta]/.\kappa \to Cos[\gamma]/.\zeta \to Cos[\theta]/.coef;}$

$$\begin{aligned} F &= AQS.S^* + D_y\ |S_y|^2 + D_{xz} S_x S_z + D_z\ |S_z|^2 + B_1\ (\mathrm{S}.S^*)^2 + \frac{1}{2} B_2 |\mathrm{S}.\mathrm{S}|^2 + \frac{B_u}{4}((\mathrm{S}.\mathrm{S})^2 + (S^*.S^*)^2 \Delta_{4Q,G} \\ &+ \frac{1}{2} A_o m^2 + \frac{1}{4} B_3 m^4 + 2\ B_4 |\mathrm{m}.\mathrm{S}|^2 + B_5 m^2\ \mathrm{S}.S^* - \mathrm{m}.\mathrm{H} \end{aligned} \tag{A.31}$$

A.3.2.1 Minimization

$\mathbf{Tx = 0.9;}$

$\mathbf{Hx = 1.5;}$

$\mathbf{Minimize[FTn[Tx, Hx]/.\alpha \to 1.22173, \{S, \beta, \theta, \gamma, mb\}]}$

$$\left\{-0.722369, \left\{S \to 1.08901, \beta \to -0.848537, \theta \to 4.58709 \times 10^{-22}, \gamma \to -8.26924 \times 10^{-18}, \mathrm{mb} \to 0.684081\right\}\right\} \tag{A.32}$$

Appendix B

Fortran code

This Appendix contains a copy of the Fortran code that was used for the numerical minimization process in order to calculate all of the data points from the theoretical magnetic field-temperature phase diagram. Different code files were necessary for doing temperature and magnetic field sweeps, this one in particular is for the field sweep. As well, the isotropic exchange interactions for the 2nd-order contribution to the free energy were minimized with the same logic. A document can be provided by Professor Guy Quirion explaining the method with more details and with the instructions regarding the application of the code.

```
PROGRAM fieldsweepch2

! Amoebasub is the minimization subroutine. Nrtype and Nrutil define parameters
and subroutines used by Amoebasub.

USE amoebasub
USE nrtype
```

```
USE nrutil
IMPLICIT REAL(DP) (A-H,O-Z)

! Define all variables and parameters.
! - x(6) is used for the variables S,beta,theta,gamma,m,alpha.
! - epsr is the tolerance of the free energy output. The smaller it is the more accurate
the results are (to a degree).
! - FREE is the function in the program that takes in x(6) and returns the free energy
at that point.
!  - a,Ab,Tq,T0,Tu,B1,B2,B3,BU,B4,B5,H,T,BUs,Tn,Azz are the parameters of the
function FREE
! - y(7) is the array that holds the calculated free energies at the 7 inital points.
! - p(7,6) is the array holding the 7 inital starting points.
! - iter outputs the number of iterations needed to converge to the given output.
! - SEED is used for the random number generator.

REAL(DP) x(6),xn(6),xu(6),x2(6),ftry(1000000),xtry(6,1000000),epsr
REAL(DP) :: FREE
COMMON /PARAM/ a,Ab,Tq,T0,Tu,B1,B2,B3,BU,B4,B5,H,T,BUs,Tn,Azz
REAL(DP), DIMENSION(7) :: y
REAL(DP), DIMENSION(7,6) :: p
INTEGER iter, i, SEED

INTERFACE
FUNCTION FREE(x)
use nrutil
```

```
use nrtype
REAL(DP), DIMENSION(:), INTENT(IN) :: x
REAL(DP) :: FREE
END FUNCTION FREE
END INTERFACE

! Read in the parameters and create the data file to save the output.

OPEN (UNIT=2,FILE='spmu')
OPEN (UNIT=4,FILE='newhsweepm.dat')

READ(2,*) Tq
READ(2,*) T0
READ(2,*) Tu
READ(2,*) a
READ(2,*) Ab
READ(2,*) Azz
READ(2,*) B1
READ(2,*) B2
READ(2,*) B3
READ(2,*) BU
READ(2,*) B4
READ(2,*) B5
READ(2,*) T
READ(2,*) H1
READ(2,*) H2
```

```
READ(2,*) NUMT
READ(2,*) num
READ(2,*) epsr
pii=DACOS(-1.d0)
tpii=pii*2.d0

! Format the parameter output.

WRITE(4,*) 'Program tempsweep.f90'
WRITE(4,*) ' '

WRITE(*,*) ' a Ab B1 B2 B3 BU B4 B5 '
WRITE(*,503) a,Ab,B1,B2,B3,BU,B4,B5
WRITE(*,*) ' H E S2 Sb2/S2 Z2 kappa c(a)2 m'

WRITE(4,*) ' T B1 B2 B3 BU B4 B5 Tu '
WRITE(4,503) T,B1,B2,B3,BU,B4,B5,Tu
WRITE(4,*) ' H E S2 Sb2/S2 Z2 kappa c(a)2 m'

WRITE(4,*) ' '

503 FORMAT(8f8.4)

! Open SEED which will be used to generate random numbers.

OPEN (UNIT=3,FILE='SEED')
```

```
READ(3,*) SEED

! Define initial starting value's range (Ex. 0 < S < smax).

smax = 1000.d0
xmmax=5.d0
emin=10000.d0

dNUMT=DBLE(NUMT)

dH=(H1-H2)/dNUMT
DO 666 It=1, NUMT+1
H=H2+dH*(It-1)

!!!
```

```
x(1)=smax*ran(SEED)
x(2)=2*pii*ran(SEED)
x(3)=(pii/2.0)*ran(SEED)
x(4)=(pii/2.0)*ran(SEED)
x(5)=xmmax*ran(SEED)
x(6)=(pii/2.0)*ran(SEED)

! Change SEED so we get new random numbers in the next iteration.

SEED = 1000000*ran(SEED) + 1

! Define the array of the starting points.

p = reshape( (/x(1), x(1)+10.0, x(1), x(1), x(1), x(1), &
x(2), x(2), x(2)+1.0, x(2), x(2), x(2), x(2), &
x(3), x(3), x(3), x(3)+1.0 ,x(3), x(3), x(3), &
x(4), x(4), x(4), x(4) ,x(4)+1.0, x(4), x(4), &
x(5), x(5), x(5), x(5) ,x(5), x(5)+1.0,x(5),&
x(6), x(6), x(6), x(6), x(6), x(6), x(6)+1.0/), shape(p))

! Calculate the free energy at each point.

do i=1,7
y(i) = FREE(p(i,:))
enddo
```

```
! Call the minimization subroutine.

CALL amoeba(p,y,epsr,FREE,iter)

! Save the minimum to test. If it gives a free energy less than the one before it is
saved and the next minimum is
! compared to it until the free energy no longer decreases.

xtry(1,itry)=p(1,1)
xtry(2,itry)=p(1,2)
xtry(3,itry)=p(1,3)
xtry(4,itry)=p(1,4)
xtry(5,itry)=p(1,5)
xtry(6,itry)=p(1,6)

x2(1)=xtry(1,itry)
x2(2)=xtry(2,itry)
x2(3)=xtry(3,itry)
x2(4)=xtry(4,itry)
x2(5)=xtry(5,itry)
x2(6)=xtry(6,itry)

ftry(itry)=FREE(x2)
IF(itry.EQ.1) GO TO 15
IF(FREE(x2).GT.emin) GO TO 15
emin = FREE(x2)
```

```
imin =itry

15 continue

eminu=emin
xu(1)=xtry(1,imin)
xu(2)=xtry(2,imin)
xu(3)=xtry(3,imin)
xu(4)=xtry(4,imin)
xu(5)=xtry(5,imin)
xu(6)=xtry(6,imin)

!!!!!!!!!!!!!!!!!!!!!!!!!!!!!!!!!!!!!!!!!!!!!!!!!!!!!!!!

! minimization with no umklapp

emin=10000.d0
BUs = 0
Tn = Tq

DO 555 itry=1,num

! Define initial points using random number generator.

x(1)=smax*ran(SEED)
x(2)=2*pii*ran(SEED)
```

```
x(3)=(pii/2.0)*ran(SEED)
x(4)=(pii/2.0)*ran(SEED)
x(5)=xmmax*ran(SEED)
x(6)=(pii/2.0)*ran(SEED)

! Change SEED so we get new random numbers in the next iteration.

SEED = 1000000*ran(SEED) + 1

! Define the array of the starting points.

p = reshape( (/x(1), x(1)+10.0, x(1), x(1), x(1), x(1), x(1), &
x(2), x(2), x(2)+1.0, x(2), x(2), x(2), x(2), &
x(3), x(3), x(3), x(3)+1.0 ,x(3), x(3), x(3), &
x(4), x(4), x(4), x(4) ,x(4)+1.0, x(4), x(4), &
x(5), x(5), x(5), x(5) ,x(5), x(5)+1.0,x(5),&
x(6), x(6), x(6), x(6), x(6), x(6), x(6)+1.0/), shape(p))

! Calculate the free energy at each point.

do i=1,7
y(i) = FREE(p(i,:))
enddo

! Call the minimization subroutine.
```

```
CALL amoeba(p,y,epsr,FREE,iter)

! Save the minimum to test. If it gives a free energy less than the one before it is
saved and the next minimum is
! compared to it until the free energy no longer decreases.

xtry(1,itry)=p(1,1)
xtry(2,itry)=p(1,2)
xtry(3,itry)=p(1,3)
xtry(4,itry)=p(1,4)
xtry(5,itry)=p(1,5)
xtry(6,itry)=p(1,6)

x2(1)=xtry(1,itry)
x2(2)=xtry(2,itry)
x2(3)=xtry(3,itry)
x2(4)=xtry(4,itry)
x2(5)=xtry(5,itry)
x2(6)=xtry(6,itry)

ftry(itry)=FREE(x2)
IF(itry.EQ.1) GO TO 555
IF(FREE(x2).GT.emin) GO TO 555
emin = FREE(x2)
imin =itry
```

```
555 continue

eminn=emin
xn(1)=xtry(1,imin)
xn(2)=xtry(2,imin)
xn(3)=xtry(3,imin)
xn(4)=xtry(4,imin)
xn(5)=xtry(5,imin)
xn(6)=xtry(6,imin)

!!!!!!!!!!!!!!!!!!!!!!!!!!!!!!!!!!!!!!!!!!!!!!!!!!!

x(1)=xn(1)
x(2)=xn(2)
x(3)=xn(3)
x(4)=xn(4)
x(5)=xn(5)
x(6)=xn(6)
emin=eminn

! Compare the energies - umklapp and no umklapp

IF(eminu.LT.eminn) x(1)=xu(1)
IF(eminu.LT.eminn) x(2)=xu(2)
IF(eminu.LT.eminn) x(3)=xu(3)
IF(eminu.LT.eminn) x(4)=xu(4)
```

```
IF(eminu.LT.eminn) x(5)=xu(5)
IF(eminu.LT.eminn) x(6)=xu(6)
IF(eminu.LT.eminn) emin=eminu

! Convert the angles from radians to degrees.

ss = x(1)*x(1)
sbs2 = dsin(x(2))*dsin(x(2))
zeta2 = dcos(x(3))*dcos(x(3))
cg2 = dcos(x(4))*dcos(x(4))
ca2 = dcos(x(6))*dcos(x(6))

! Formatted output.

WRITE(*,333) H,emin,ss,sbs2,zeta2,cg2,ca2,x(5)
WRITE(4,333) H,emin,ss,sbs2,zeta2,cg2,ca2,x(5)

333 FORMAT(f7.3,1x,e11.5,1x,e11.5,1x,f7.3,1x,f7.3,1x,f7.3,2x,f7.3,1x,e11.3)

666 continue

REWIND 3
WRITE(3,*) SEED

STOP
END PROGRAM fieldsweepch2
```

```
!-----------------------------------------------------------

! Free energy that is being minimized.
! x(1) = S
! x(2) = beta
! x(3) = theta
! x(4) = gamma
! x(5) = m
! x(6) = alpha

FUNCTION FREE(x)
USE amoebasub
USE nrtype
USE nrutil
IMPLICIT REAL(DP) (A-H,O-Z)

REAL(DP) x(:), xm2, xm4, S2, S4, xm
COMMON /PARAM/ a,Ab,Tq,T0,Tu,B1,B2,B3,BU,B4,B5,H,T,BUs,Tn,Azz

S=x(1)
beta=x(2)
theta=x(3)
gamma=x(4)
xm = x(5)
alpha = x(6)
```

```
S2=S*S
S4=S2*S2
xm2 = xm*xm
xm4 = xm2*xm2
G2 = dcos(gamma)*dcos(gamma)
G4 = G2*G2
Sb2 = S2*dsin(beta)*dsin(beta)
Sb4 = Sb2*Sb2
Z2 = dcos(theta)*dcos(theta)
Z4 = Z2*Z2
ca2 = dcos(alpha)*dcos(alpha)
sa2 = dsin(alpha)*dsin(alpha)
Axz = 0.5*Azz
ca = dcos(alpha)
s2a = dsin(2*alpha)
c2a = dcos(2*alpha)
Gs = dsin(gamma)
Zs2 = dsin(2*theta)
saca = dsin(alpha)*dcos(alpha)
stct = dsin(theta)*dcos(theta)

AQ=a*(T-Tn)
A0=a*(T-T0)

F2 = AQ*S2 - Ab*G2*S2 + Ab*Sb2*Z2*G2
```

```
A1 = Axz*(s2a*((G2-1)*S2-Z2*(G2-2)*Sb2)+Sb2*c2a*Gs*Zs2)
A2 = Azz*(ca2*(Z2*(G2-2)*Sb2-(G2-1)*S2)+2*Sb2*saca*Gs*stct+Z2*Sb2)
F4 = B1*S4 + 0.5*B2*S4 - 2*B2*Sb2*Z2*S2 + 2*B2*Sb4*Z2
FU = BUs*(0.5*S4 - 4*Sb2*S2 + 2*Sb2*Z2*S2 + 4*Sb4 - 2*Sb4*Z2)
FH = 0.25*B3*xm4 + B5*S2*xm2 + 2*B4*S2*G2*xm2 - 2*B4*Sb2*Z2*G2*xm2 +
0.5*A0*xm2 - xm*H

FREE = F2 + F4 + FU + FH + A1 + A2

RETURN
END
```